THESIS FOR THE DEGREE OF DOCTOR OF PHILOSOPHY
WITH INTERNATIONAL MENTION FOR THE UNIVERSITY
OF SEVILLE

# Study of static and dynamic damage identification in multifield materials with artificial intelligence, BEM and X-FEM

GABRIEL HATTORI DA SILVA

Department of Continuum Mechanics and Structural Analysis
School of Engineering
UNIVERSITY OF SEVILLE
Seville, Spain 2013

Study of static and dynamic damage identification in multifield materials with artificial intelligence, BEM and X-FEM
Phd's Thesis in the Advanced Design in Mechanical Engineering program
GABRIEL HATTORI DA SILVA
Advisor: Prof. Dr. Andrés Sáez Pérez
Co-advisor: Prof. Dr. Felipe García Sánchez
Department of Continuum Mechanics and Structural Analysis
School of Engineering
University of Seville

## Abstract

The research proposed in this Thesis approaches the multifield materials by two main branches: the study of the fracture mechanics problem (direct problem), and the development of a damage identification methodology (inverse problem). Numerical methods have been studied for the direct problem and techniques have been proposed so new problems can be treated, notably a new formulation for enrichment function in extended finite element method, and a far field fundamental solution to be used conjointly with the boundary element method. With respect to the inverse problem, artificial intelligence techniques have been combined in a hybrid damage identification scheme, using supervised (neural networks) and unsupervised (self-organizing algorithms) learning techniques, providing excellent identification results despite the presence of high levels of external interference in the measured response. Experimental damage assessment was also investigated in this Thesis, and a methodology using data fusion and a Gaussian mapping has proved to provide good identification results.

**Keywords:** Damage identification, multifield materials, neural networks, self-organizing algorithms, boundary element method, extended finite element method, far field Green's function, experimental damage assessment

## PREFACE

I would like to express some lines of gratitude for those who have, in a way or another, contributed to the development of the research carried out by the author of this Thesis.

To my advisors, Prof. Andrés Sáez Pérez, for trusting me in the first place, for encouraging and supporting my pursue of the damage identification in multifield materials, and Prof. Felipe García Sánchez, always up to do some mathematical brainstorming. I am grateful for all the opportunities they granted me which greatly contributed to my growth as a researcher.

To Ramón Rojas Díaz, who encouraged me to deviate a little from the boundary elements and go towards the extended finite elements.

To Prof. Lin Ye, who provided a nice workplace during my research stay at the *Centre for Advanced Materials and Technology, the University of Sydney*, allowing me to perform my first experiments with smart materials, and to Samir Mustapha, for his infinite patience helping me with the experimental set-ups.

To Prof. Anders Boström, for receiving me into his group at the *Division of Dynamics, Chalmers University of Technology* during my second research stay, making sure I had everything I needed to continue with my research. Also to Jonathan Westlund and his family for the conviviality during my time in Göteborg.

To my colleagues (past and present) of the Department of Continuum Mechanics.

And last but not least to my friends for everything.

Sevilla, September 2013
Gabriel Hattori da Silva

## ACKNOWLEDGEMENTS

This Thesis has been supported by the Spanish Government through the research projects DPI2007-66792-C02-02 and DPI2010-21590-C02-02, and by the Excelence Research Project reference P09-TEP-5054, and it is gratefully acknowledged.

## THESIS

This Thesis consists of an extended summary and the following appended papers:

| | |
|---|---|
| **Paper A** | G. Hattori and A. Sáez<br>Damage identification in multifield materials using neural networks<br>*Inverse Problems in Science and Engineering*, 2013. |
| **Paper B** | G. Hattori and A. Sáez<br>Crack identification in magnetoelectroelastic materials using neural networks, self-organizing algorithms and boundary element method<br>*Computers & Structures*, 125:187-199, 2013. |
| **Paper C** | G. Hattori, R. Rojas-Díaz, A. Sáez, N. Sukumar and F. García-Sánchez<br>New anisotropic crack-tip enrichment function for the extended finite element method<br>*Computational Mechanics*, 50:591-601, 2012. |
| **Paper D** | G. Hattori, A. Sáez and A. Boström<br>Far field Green's fundamental solution for dynamic loading in magnetoelectroelastic materials<br>*XIV Advances in Boundary Element Techniques*, 1:475-480, 2013. |
| **Paper E** | G. Hattori, S. Mustapha, L. Ye and A. Sáez<br>An experimental approach for crack identification/assessment in piezoelectric materials<br>*10th World Congress on Computational Mechanics*, 2012. |

The appended papers were prepared in collaboration with co-authors. The author of this Thesis is responsible for the major progress of work in these papers, including the development/deduction of solution and numerical methods, performing the numerical simulations and experiments and writing the main parts of the papers.

# Contents

# 1 Introduction

In the last few years it has become more critical to supervise correctly the behavior of complex systems. Civil, aerospace, automobile industries are particularly concerned about the safety requirements, making crucial the correct prediction of faillure for a given structure/system. Intense research has been seen to analyze the durability, integrity and security of structural components. Nondestructive evaluation techniques (NDE) have been effectively used to detect and quantify structural damage at early stages, assuring that corrective measures can be taken in time. The procedure of damage assessment is often called damage identification or damage diagnosis.

Modern NDE techniques include radioscopy, ultrasonic scanning, dye penetrant testing, magnetic resonance imagery, laser interferometry, infrared thermography, among many others [122]. Most NDE approaches depend on the acquisition of structural response signals by means of a series of sensors under a known excitation, then compare the actual response to some benchmark solution. Materials presenting coupling behavior, such as the piezoelectric material, which presents coupling in the elastic and electric fields, are commonly used in the damage evaluation framework. The coupling behavior permits the material to act as sensor or as an actuator, which is desirable in damage evaluation schemes. Nevertheless, NDE techniques have been scarcely used in damage identification of multifield materials.

A new material has been created from the combination of a piezoelectric and a piezomagnetic phase [130]. This new material was called magnetoelectroelastic (MEE), presenting coupling in the elastic, the electric and the magnetic fields. Multifield materials have been widely studied [34, 35, 74, 94, 110] to cite some of the most recent works. The main problem of this class of material is due to their crystal arrangement, which implies in materials with brittle behavior. The crystal arrangement contained in this class of materials provide an undesirable effect: brittle behavior, which almost ensures the presence of defects due to operation and even in fabrication process [46, 47]. Hence, it is expected that the presence of damage changes the response of these materials. However, if the damage can be properly depicted, it is possible to interpret the response of the damaged multifield material. In other words, it would be as the material had no damage, since the measures obtained from it will be perfectly decoded. If the multifield material is used as a sensor, for instance, it would be possible to obtain some useful structural data via the faulty sensor. Thus, it is clear the importance of having a damage identification scheme for multifield materials.

Very few works can be found about damage identification in multifield materials. Furthermore, they are devoted to piezoelectric materials only: a genetic algorithm and the finite element method were applied to identify hole-type damage in piezoelectric ceramics for static [100] and time-harmonic [101] loadings. A probabilistic theory was applied for damage identification in piezoelectrics in [81]. Analytical inverse problem formulation concerning piezoelectric materials is given in [116].

## 1.1 Objectives

The main objective of this Thesis is to develop the damage identification tools for multifield materials, in particular when MEE materials are considered. The detection and quantification of damage may be crucial depending on the current application, specially if the material can not be replaced (for example, in off-shore structural health monitoring sensors). Instead of developing an analytical formulation which could be only used with this class of materials, and may not properly describe the material behavior under real operation circumstances, an artificial intelligence hybrid approach is proposed to solve this inverse problem.

Artificial intelligence tools such as the neural networks (NN) have been widely employed with high performance in all kinds of inverse problems. The NN architecture allows the interpolation of any system that can be described by an input-output relation. The existence of a model that characterizes the direct problem makes easier the approach using artificial intelligence tools. Analytical [15, 25, 42, 43, 55, 135] and numerical [22, 47, 95, 115, 146] models were developed in the last 30 years, analyzing how different types of damage affect the response in multifield materials. The effect of cracks in piezoelectric materials was also verified experimentally in [54, 62, 64, 86, 113, 114, 127].

Classical numerical methods such as the finite element method (FEM) and the boundary element method (BEM) have been used to model defects in multifield materials. New numerical methods have also been introduced, such as the meshless methods and the extended finite element method (X-FEM). In this Thesis two numerical methods are employed, the BEM and the X-FEM.

The BEM is vastly known due to its accuracy and stability in linear fracture mechanics problems. Most of the issues of modeling cracks in MEE materials and BEM have been studied and solved by previous researchers [46–48, 92, 93], including the deduction of Green's fundamental solution (FS) for anisotropic [132, 133], piezoelectric [28] and MEE materials [20, 94]. The fundamental solution is the kernel of the BEM, allowing the proper discretization of the domain. In this work, the BEM was used to solve the direct problem, i.e., the influence of a damage in the response of a MEE material.

The X-FEM has been shown to be a breakthrough in fracture mechanics due to the modeling of a crack in terms of enrichment functions instead of considering it as a phys-

ical geometrical boundary [14,71,123] in a FE context. Enrichment functions have been deduced for isotropic [71], orthotropic [8], piezoelectric [13] and MEE [95] materials, but no general anisotropic enrichment function was available. A new enrichment function based on Stroh's formalism is proposed in this Thesis, defined in a compact form and depending only on the material properties.

Experimental methods are also of great interest in damage identification, since it is possible to study the methods in real applications. A number of authors have studied damage identification experimentally [6,63,73,109,129]. Once again, little attention has been given to the damage identification in smart materials [59, 83]. Part of the work developed in this Thesis consists in an experimental dynamic damage identification scheme using commercial piezoelectric sensors. Real operation conditions can be emulated, and the performance of damaged sensors are compared to a reference solution from pristine sensors.

It was verified that the actual Green's functions for piezoelectric and MEE materials are not effective when the distance between the position where the load is applied and the position where the response is measured, or if the frequency increases. The main reason of this problem is the oscillation of the integrand, making necessary to discretize the integration domain in smaller parts, which can be computationally time consuming. This issue severely penalizes damage identification in high frequencies, where lies most of sensor applications. To avoid this problem, a new Green's function for piezoelectric and MEE materials valid for the far field was deduced.

# 2 Inverse problems

## 2.1 Definition

Initially, we have to define what is the difference between direct and inverse problem. Let $f$ be a general function that describes some physical model, and $\mathbf{x}$ the parameters that characterize the model. The solution of the direct problem $\mathbf{y}$ is defined as

$$\mathbf{y} = f(\mathbf{x}) + \xi \tag{2.1}$$

where $\xi$ is a noise present in the solution. Two types of inverse problems can be defined in this case:

1. Considering that a series of values $\mathbf{y}$ and the originating parameters $\mathbf{x}$ are known, find the model $f$.

2. Considering that a series of values $\mathbf{y}$ and the model $f$ is known, find the parameters $\mathbf{x}$.

In this Thesis, the focus is directed to the second inverse problem option. Consider a simple example, a mass-spring-damper system. The parameters of the problem are the mass $m$, the damping $c$ and the stiffness $k$. The problem model is given by the known equation $m\ddot{u} + c\dot{u} + ku = F(t)$ for dynamic loading, where solution is the displacement $u(t)$ for a given excitation $F(t)$. In the inverse problem, the displacement $u(t)$ and the excitation $F(t)$ are known, and the parameters $m$, $c$ and $k$ are the unknowns.

In summary, structural analysis for responses under a given load represent a direct problem. The identification of structural parameters that cause the measured response is the definition of an inverse problem. Figure 2.1 illustrates the direct and inverse problem schemes. Most inverse problems numerical approaches consist of the use of a black-box model, where some measured (or test) data with known parameters is used to update the model until an acceptable error is attained.

Inverse problems are difficult to treat because they are very likely to violate at least one of the Hadamard conditions [49]:

- Existence. Sometimes there is no model that can fit properly the measured data with the parameters. The presence of noise in the data is the most common reason to the absence of a reliable inverse model.

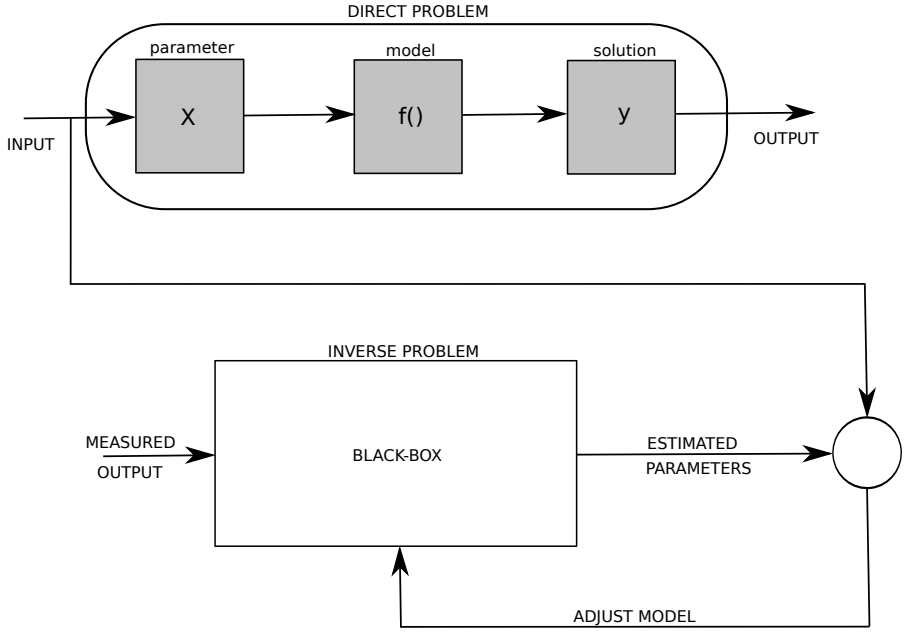


Figure 2.1: Scheme of direct and inverse problems.

- Uniqueness. There could be more than a set of parameters that describe exactly the same solution, being impossible to distinguish which parameter has caused the current response.
- Continuity. Small errors in the initial conditions or in the source terms should lead to small deviations in the solution. However, this condition is often not satisfied, since small changes in the solution may cause large changes in the originating parameters. The effect of this latter can be reduced by regularizing the problem, so the inversion process is stabilized with the use of some additional constraints. Some classical regularization methods can be cited as the truncated Singular Value Decomposition (SVD) [50], the Tikhonov regularization [126], and nonlinear total variation [99].

In practice, analytical formulations are hardly used in inverse problems, since there is often some interference (e.g. noise) in the measured data. The possible uncertainities have to be considered in the inverse model. Artificial intelligence and evolutionary algorithms as the neural networks and genetic algorithms, respectively, have been used widely and successfully in the inverse problem context. These methods require the direct problem formulation to model the inverse problem. Moreover, their nondeterministic feature allow to easily model the uncertainities present in the inverse problem. Nevertheless, other issues may appear, being the most typical convergence

problems and local optimum solutions.

Several types of inverse problems can be defined as

1. Boundary value inverse problems: direct measurements at the boundary are infeasible.

2. Cauchy inverse problem: the response is unknown at some part of the system/-body, and it is known everywhere else.

3. Material properties inverse problems: the response of the system is known, with unknown material properties.

4. Identification inverse problem: part of the geometry is unknown, such as defects or inclusions. This is the main focus treated in this Thesis.

   etc.

## 2.2 Damage identification

Damage identification is a branch of inverse problems. It is assumed that a structure/-component presents some type of damage, with size and location unknowns, and it is desirable to know these parameters from some measured structural response. Damage is a structural state different from the pristine state [122], so a benchmark solution (undamaged state) is required to define the implications of the damage in the structure. A system of damage classification has been introduced by [102]

1. Determine if damage is present in the structure;

2. Determine/estimate the damage location;

3. Determine/estimate the extension of the damage;

4. Estimate the structure remaining life;

The key aspect of this Thesis is to completely and accurately characterize the damage, without taking in consideration how the damage affects the service life. Damage detection can be very straightforward to determine, since a simple shift in the solution (assuming a benchmark solution is available) characterizes the damage. However, location and quantification of damage can be complicate, and some techniques are detailled as follows:

- Model updating techniques: These techniques [41, 72] have the objective of approximating the solution from the numerical model of the direct problem to the

real measurements through modification of the initial discretization model, by incorporating more features of the analyzed problem. The parameters of the numerical modeling providing the best fit with the real measurements are the wanted damage parameters.

- Mode shape analysis: Modal parameters such as frequencies and mode shapes depend directly of some properties of the physical model. The idea is to detect the change in the modal parameters to quantify the change of the physical properties. Mode shapes contain local information, which makes them more sensitive to local damages and enables them to be used directly in multiple damage detection [37]. Also, it is possible to use the mode shape information alone to calculate the structural state, without the need of a benchmark solution. These methods take mode shape change or mode shape data as a spatial-domain signal and use signal processing technique to locate the damage by detecting the local discontinuity of mode shape curve caused by the damage. Their basic assumption is that the mode shape data from a healthy structure contains only low-frequency signal in spatial domain compared to the damage-induced high-frequency signal change [37]. However, mode shape analysis rely on sensors for measuring, making them more susceptible to external disturbances, and distortions due to improper sensor functioning.

- Natural frequency analysis: These range of methods are attractive because the natural frequencies can be obtained from a few accessible points on the structure, also being less willing to noise influences. Nevertheless, in [104] it has been seen that natural frequencies alone may not represent a unique identification of the damage location, since cracks of similar lengths at different locations may cause the same amount of frequency change.

- Frequency Response Function (FRF) analysis: the FRF analysis uses directly the data obtained from a frequency measurement. It is simple and depending on the analyzed problem, it can have more significant results than methods based on natural frequencies or mode shapes. It is less sensitive to noise than mode shape analysis, due to the use of the measured frequency response directly, and it is possible to use reduced frequency ranges [66,105]. Frequency shifts can be useful to detect damage, but the need of an accurate measure to ensure that the shift is related to the damage than a measurement disturbance is a major drawback.

- Wavelets analysis: the wavelets allow to perform a direct time-frequency analysis, being useful for processing dynamic signals and images. The wavelets are waveforms with limited duration, designed to resonate with signals which contain information of similar frequency. This numerical tool has been introduced in the analysis of vibration signals by [23,75,76] and can recognize singularities in

the analyzed signal, characterizing them in space and time. These reasons makes very attractive the use of wavelets in damage identification schemes.

- Time reversal: the origin of this approach comes from the wave reciprocity, which states that if there is a solution of the Navier's equation, then the time reversal of that solution is also a solution of the Navier's equation [52]. In brief, the solution due to a given excitation at point A and measured at point B of a structure is equivalent to the reflected solution applied at point B and measured at point A, assuming both A and B arbitrary positions in the structure. This latter is called the reversed wave, and should generate the exact excitation which originated the first wave. Clearly, this paradox can be applied only where the wave reciprocity holds, being valid for ultrasonic waves in composites structures for example. Time reversal can infer the presence of damage in view that the time reversibility of the wave solution is affected by the presence of damage in the wave propagation path. This particular method has the advantage of not requiring a benchmark solution in order to properly determine the location and size of the damage, which is assessed through calibration of the deviation of the reconstructed wave solution with respect to the original wave [84, 106].

- Damage Index (DI) and data fusion: the definition of a DI can greatly simplify the damage identification process, by the statement of a benchmark solution and a known solution with damage. DI has the objective of extracting the damage features of the measured solution, as can be seen in [29, 67, 90, 140], to cite a few references. The combination of multiples features extracted from multiples distributed sensors to obtain the damage state is called data fusion. Data fusion are used to obtain a graphic solution of the region where it is more probable to present damages [56, 122]. DI and data fusion were used in this Thesis to evaluate the structural state of a piezoelectric plate experimentally.

- Artificial intelligence (AI) analysis: The primary objective of this Thesis is to develop an AI methodology to detect and quantify damage in multifield materials. The usual approach in damage identification problems with AI tools is to create a black-box model through the adjustment of a set of known parameters and the associated measured output. The AI techniques used in this Thesis are detailled in the following section.

## 2.3 Review of artificial intelligence techniques

Artificial neural networks (NN) have been conceived to mimic the human nervous system, by the inference that if the biological structure is intelligent, another similar artificial structure will also be intelligent [51]. The human nervous system is composed

by billions of small structures called neurons, which propagate the information in the neural net in the form of electrochemical waves through the axons. The junction where the information from a neuron is transmitted to another is called synapses. The information is modified and propagated by the neurons.

A computational model may be developed to simulate this particular processing information structure. The result is a much simpler model compared to the original one, but with strong capabilities of interpolation and parallelism, being able to learn the functionallity of complex systems described by a series of input/output pairs, and extrapolate the results, predicting the correct output from an input which has not been used to establish the model.

NN are composed by neurons, which are organized in a layered structure as illustrated in Figure 2.2 and can be defined as follows:

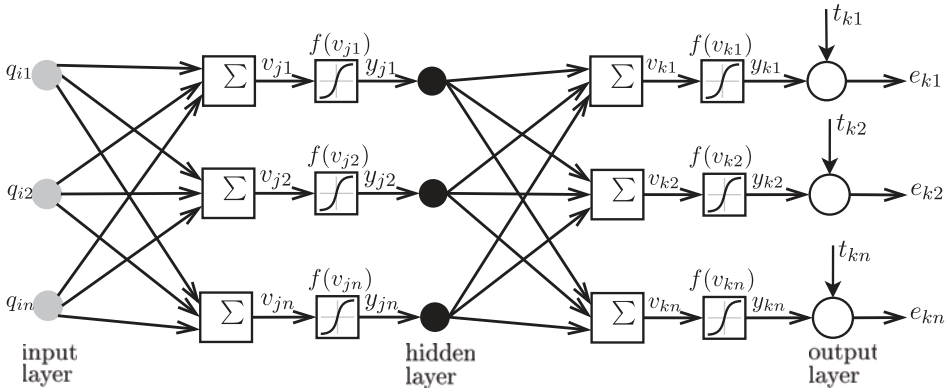


Figure 2.2: Scheme of a back-propagation NN. From **Paper A**.

- Input layer: receives the data to be interpolated/identified, for example, the measured response of a structure.
- Hidden layers: allows the information from the input layer to be transmitted through the network. The connectivity between the neurons are indispensable to the effectivity of the interpolation provided by the NN.
- Output layer: provides the parameter estimation given the measured response. The NN error can be quantified only at this point and it is used to update the weights.

Each connection between neurons from different layers represents a weight. A NN learns a pattern by the update of the weights, thus being the main responsible of modifying the information from the input layer to the output layer.

The information contained in a layer is gathered together, modified by an activation function and then propagated to the next layer. This process is repeated until the information reaches the output layer, where it becomes the NN response to the received data.

NN have become popular in inverse problems schemes due to its simplicity of use and possibility of modelling practically any type of inverse model. However, there are some issues which have to be carefully considered to take full advantage of the NN:

- The selection of an appropriate architecture: this is the most complicated parameter to be adjusted, where the user knowledge on the analyzed problem may be critical. The number of layers and the number of neurons per layer can determine whether the NN can create a meaningful model from the training set or not.

- Prevent overfitting: excessive training may cause the NN to recognize only its training set, being unable to identify other patterns which are inside the training space but have not been used in training, one of the main advantages of modelling inverse problems with NN. The control of the error of patterns not used in the NN training can provide insight of overfitting. The verification set is composed by inputs other than those in the training set. If the error of this verification set increases while the error of the training set decreases is a strong indicator of overfitting.

- Regularization: in problems where external interference is present, the NN training may be seriously compromised. Since inverse problems have the tendency to be ill-conditioned, a small change in the NN input may represent a high change in the NN output. Thus, it may be necessary to use regularization techniques to reduce the interference influence in the NN training. An example of regularization method in NN is the work of [39], where a combination of the Levenberg-Marquardt training algorithm with a Gaussian formulation is performed.

A large list of works that used NN in inverse problems could be cited. Lately, special focus is given to composite materials. In [121] a combined approach of wavelets and NN is used to detect delamination in quasi-isotropic composite, where the structural information is captured by means of Lamb waves. A hybrid strategy of NN and genetic algorithm for identifying the nonlinear model of a composite laminate shell is found in [12]. In [139], an adaptive NN technique is proposed for the detection of cracks in anisotropic laminated plates, by using the displacement response on the surface of the plate given a time-harmonic excitation. The strip element method and NN were applied for the identification of interfacial delaminations in carbon/epoxy laminated composite beams in [53]. Undamped eigenfrequencies were used in [7] to estimate the elastic and piezoelectric parameters in active plates with both gradient optimization and NN.

NN are an example of supervised learning models, since an error has to be controlled and reduced to a minimum. Other artificial intelligence techniques are said to be unsupervised, due to the absence of a reference error. Clustering techniques, such as the K-means and Gaussian mixtures (GM), have the purpose of reorganizing data such that components with similar features remain in the same cluster.

A review of the clustering methods can be found in [96]. Some clustering methods use distance measures (e.g. the Euclidean distance) to determine the similitude between two given components. Other clustering methods rely on the fact that the components belonging to a cluster are drawn from some probability distribution. In both cases, the number of clusters to be created has to be defined beforehand, which can be intricate since no information is available concerning the number of clusters in most cases. To overcome this issue, some indices have been created to find the optimum number of clusters depending on the used algorithm (see [24, 32], for example).

Clustering methods have also been used in inverse problems. In [65], the first twelve mode shapes of a bridge have been recognized by a hierarchical clustering algorithm. A combination of the acoustic emission and K-means has been used for identification of the failure mechanims by [82]. Damage types in composite materials were separated into two groups by [142] using clustering techniques.

The NN training set has been created through solving the direct problem successively. The boundary element has been used in this work due to their superior accuracy compared to standard finite elements. Nevertheless, the extended finite elements have shown to be a great advance in order to suppress the weakness of standard finite elements in fracture mechanics problems. Both numerical methods are described in the following section.

## 2.4 Review of numerical methods

### 2.4.1 Boundary element method (BEM)

The boundary element method (BEM) was first introduced in the work of Brebbia and Domínguez [17] and represented a series of advances in comparison to the existent domain discretization methods as the finite element method (FEM) and the finite differences method (FDM):

- More accurate mathematical definitions are employed, resulting in a more accurate and stable discretization method. The formulation can consider infinite and half spaces, specially advantegeous in the dynamic domain.
- The problem is defined only at the boundaries, which implies in a reduced mesh (linear for 2D problems and surface for 3D problems), therefore resulting in a reduced set of linear equations to be solved.

- Any internal point in the domain can be calculated once the boundary problem has been solved.

- Great advantage in acoustic, fracture mechanics, re-entry corners and stress intensity problems, where domain discretization methods have poor performance and accuracy.

However, there are some drawback which may have kept away FEM users to migrate to the BEM:

- The system of equations is not symmetric and it is fully populated, which may lead to longer computing times (compared to FEM for example), specially in 3D problems. In this case, techniques such as the fast multipole method [97] has been introduced to speed up the solution in large-scale problems.

- A Fundamental Solution (FS) or Green's function, describing the behavior of a point load in a infinite medium of the material properties is part of the kernel of the method. The calculation of FS is another field of research, which can make unfeasible the use of BEM in problems where a FS is not available beforehand.

- FS must be computationally efficient, which makes explicit FS formulations very desirable in this sense. Dynamic problems usually have implicit formulations, see [28,94,133] for instance, where the FS is expressed in a integral form by means of the Radon transform.

- The BEM formulation may present singularities/hypersingularities which must be analytically regularized before any numerical integration can be performed, as can be seen in [46,47].

- Non-linear problems (e.g., material nonlinearities) may be difficult to model.

A high number of researchers have embraced BEM and its possible uses were multiplied: elastic [18, 118], elastodynamics [30, 68], ultrasonic [16], thermic [134], fluids [10,89], acoustics [33,136], just to cite a few references.

The constitutive equations relating the mechanical stresses $\sigma_{ij}$, the electric displacements $D_i$ and the magnetic inductions $B_i$ with the elastic strains $\epsilon_{ij}$, the electric field $E_i$ and the magnetic field $H_i$ are given as [119]

$$\sigma_{ij} = C_{ijkl}\epsilon_{kl} - e_{lij}E_l - h_{lij}H_l \tag{2.2}$$

$$D_i = e_{ikl}\epsilon_{kl} + \kappa_{il}E_l + \beta_{il}H_l \tag{2.3}$$

$$B_i = h_{ikl}\epsilon_{kl} + \beta_{il}E_l + \gamma_{il}H_l \tag{2.4}$$

with $c_{ijkl}$, $\kappa_{il}$ and $\gamma_{il}$ denoting the elastic stiffness, the dielectric permittivities and the magnetic permeabilities tensors, and $e_{lij}$, $h_{lij}$ and $\beta_{il}$ being the piezoelectric, the piezomagnetic and the electromagnetic coupling coefficients, respectively, and

$$\epsilon_{ij} = \frac{1}{2}\left(u_{i,j} + u_{j,i}\right); \quad E_i = \varphi_{,i}; \quad H_i = -\phi_{,i} \tag{2.5}$$

The Einstein summation notation applies in Eqs. (2.2)-(2.4). The displacements response in multifield materials can be written in a compact form, where the elastic displacements $u_i$, the electric potential $\varphi$ and the magnetic potential $\phi$ are assembled together in a generalized displacement vector $u_I$ defined as [11]

$$u_I = \begin{cases} u_i, & \text{I=1,2} \\ \varphi, & \text{I=4} \\ \phi, & \text{I=5} \end{cases} \tag{2.6}$$

where the lowercase subscripts vary from 1 to 3 in 3D problems, whereas the index $i = 3$ is omitted in 2D problems. The uppercase subscripts define the type of material:

- if $I = \{1, 2\}$, an elastic material is considered.
- if $I = \{1, 2, 4\}$, a piezoelectric material is considered.
- if $I = \{1, 2, 4, 5\}$, a MEE material is considered.

Again, the index $I = 3$ is reserved only for 3D materials. Analogously, a generalized stress tensor $\sigma_{iJ}$ is defined as

$$\sigma_{iJ} = \begin{cases} \sigma_{ij}, & \text{J=1,2} \\ D_i, & \text{J=4} \\ B_i, & \text{J=5} \end{cases} \tag{2.7}$$

and the generalized traction vector $p_J$ is given by

$$p_I = \begin{cases} p_i = \sigma_{ij} n_j, & \text{I=1,2} \\ D_n = D_j n_j, & \text{I=4} \\ B_n = B_j n_j, & \text{I=5,} \end{cases} \tag{2.8}$$

with $\mathbf{n} = (n_1, n_2)$ being the outward unit normal to the boundary, $p_i$ the elastic tractions, and $D_n$ and $B_n$ the normal electric displacement and normal magnetic induction, respectively. A generalized elasticity tensor can also be specified as

$$C_{iJKl} = \begin{pmatrix} c_{ijkl} & e_{lij} & h_{lij} \\ e_{ikl} & -\epsilon_{il} & -\beta_{il} \\ h_{ikl} & -\beta_{il} & -\gamma_{il} \end{pmatrix} \tag{2.9}$$

so that the constitutive equations may be written in an elastic-like fashion as

$$\sigma_{iJ} = C_{iJKl} u_{K,l} \tag{2.10}$$

The time-harmonic equilibrium equations for a MEE material in the absence of body forces can be written as

$$\sigma_{ij,j}(\mathbf{x}, \omega) + \rho\omega^2 u_i(\mathbf{x}, \omega) = 0 \tag{2.11}$$

$$D_{i,i}(\mathbf{x}, \omega) = 0 \tag{2.12}$$

$$B_{i,i}(\mathbf{x}, \omega) = 0 \tag{2.13}$$

where $\omega$ is the frequency of excitation and $\rho$ is the mass density of the material. The Maxwell equations are written assuming the quasi-static approximation [87] on the electric and magnetic fields. Similarly, Eqs. (2.11)-(2.13) can also be written in the generalized form as

$$C_{iJKl} u_{K,il}(\mathbf{x}, \omega) + \rho\omega^2 \delta_{JK} u_K(\mathbf{x}, \omega) = 0 \tag{2.14}$$

where $\delta_{JK}$ stands for the generalized Kronecker delta, which acts as the standard Kronecker delta for $I, J = 1, 2$, being zero otherwise.

From Figure 2.3, let $\Omega$ be a 2D MEE cracked domain with boundary $\Gamma$, which can be decomposed in two boundaries, an external boundary $\Gamma_c$ and an internal crack $\Gamma_{crack} = \Gamma_+ \cup \Gamma_-$ represented by two geometrically coincident crack surfaces.

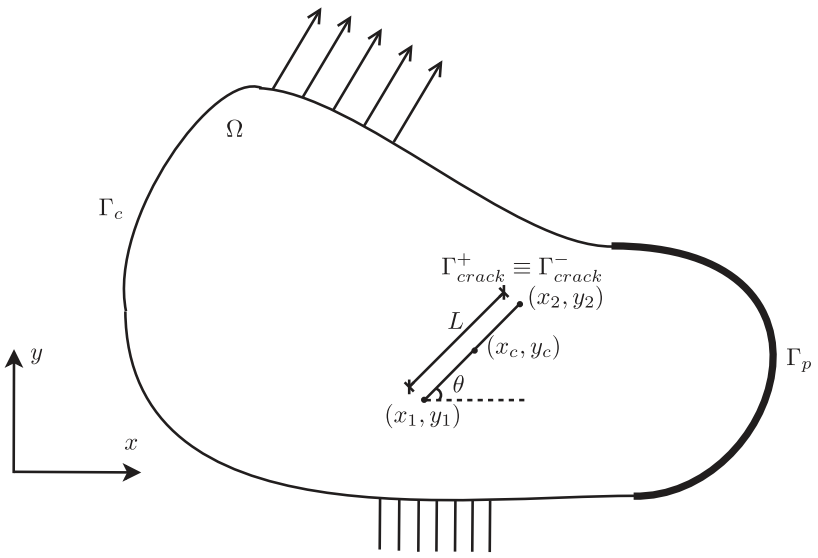


Figure 2.3: Scheme of the direct problem. From **Paper B**.

The Dual BEM formulation relies on two boundary integral equations (BIE), one with respect to the displacements at a point $\boldsymbol{\xi}$ of the domain $\Omega$ and frequency $\omega$ defined as

$$c_{IJ}(\boldsymbol{\xi})u_J(\boldsymbol{\xi},\omega) + \int_\Gamma p^*_{IJ}(\boldsymbol{x},\boldsymbol{\xi},\omega)u_J(\boldsymbol{x},\omega)d\Gamma(\boldsymbol{x}) = \int_\Gamma u^*_{IJ}(\boldsymbol{x},\boldsymbol{\xi},\omega)p_J(\boldsymbol{x},\omega)d\Gamma(\boldsymbol{x}) \tag{2.15}$$

and a BIE with respect to the generalized tractions, defined as

$$c_{IJ}(\boldsymbol{\xi})p_j(\boldsymbol{\xi},\omega) + N_r\int_\Gamma s^*_{rIJ}(\boldsymbol{x},\boldsymbol{\xi},\omega)u_J(\boldsymbol{x},\omega)d\Gamma(\boldsymbol{x}) = N_r\int_\Gamma d^*_{rIJ}(\boldsymbol{x},\boldsymbol{\xi},\omega)p_J(\boldsymbol{x},\omega)d\Gamma(\boldsymbol{x}) \tag{2.16}$$

which follows from the differentiation of the displacement BIE and further substitution into the constitutive laws equation (for details see [46]). $N_r$ stands for the outward unit normal to the boundary at the collocation point $\boldsymbol{\xi}$, $c_{ij}$ is the free term that comes from the Cauchy Principal Value integration of the strongly singular kernels $p^*_{IJ}$, $u^*_{IJ}$ and $p^*_{ij}$ are the displacement and traction FS and $d^*_{rIJ}$ and $s^*_{rIJ}$ follow from derivation and substitution into the Hooke's law of $u^*_{IJ}$ and $p^*_{IJ}$, respectively.

When modeling MEE materials in BEM, it is usual to adopt the impermeable boundary condition in the crack [25, 80], thus considering that the crack is shielded against the electric and magnetic fields. In addition, the cracks are considered to be free of mechanical tractions. These boundaries conditions can be summarized as

$$\Delta p_J = p_J^+ + p_J^- = 0 \tag{2.17}$$

where the '+' and '-' superscripts represents the upper and lower crack surfaces, respectively. The use of the impermeable boundary condition allows to redefine Eqs. (2.15) and (2.16) in terms of the crack-tip opening displacement ($\Delta u_J = u_J^+ - u_J^-$) in function of the crack-free boundary $\Gamma$ and one of the crack surfaces, say $\Gamma_+$

$$c_{IJ}(\boldsymbol{\xi})u_J(\boldsymbol{\xi},\omega) + \int_{\Gamma_c} p^*_{IJ}(\boldsymbol{x},\boldsymbol{\xi},\omega)u_J(\boldsymbol{x},\omega)d\Gamma(\boldsymbol{x}) + \int_{\Gamma_+} p^*_{IJ}(\boldsymbol{x},\boldsymbol{\xi},\omega)\Delta u_J(\boldsymbol{x},\omega)d\Gamma(\boldsymbol{x}) = \int_{\Gamma_c} u^*_{IJ}(\boldsymbol{x},\boldsymbol{\xi},\omega)p_J(\boldsymbol{x},\omega)d\Gamma \tag{2.18}$$

$$p_J(\boldsymbol{\xi},\omega) + N_r\int_{\Gamma_c} s^*_{rIJ}(\boldsymbol{x},\boldsymbol{\xi},\omega)u_J(\boldsymbol{x},\omega)d\Gamma(\boldsymbol{x}) + N_r\int_{\Gamma_+} s^*_{rIJ}(\boldsymbol{x},\boldsymbol{\xi},\omega)\Delta u_J(\boldsymbol{x},\omega)d\Gamma(\boldsymbol{x}) = N_r\int_{\Gamma_c} d^*_{rIJ}(\boldsymbol{x},\boldsymbol{\xi},\omega)p_J(\boldsymbol{x},\omega)d\Gamma(\boldsymbol{x}) \tag{2.19}$$

In this latter equation, the free term has been set to 1 due to the additional singularity arising from the coincidence of the two crack surfaces. The use of an hypersingular

formulation do not limit at all the crack shape, being valid for curved and branched cracks, for example. The inconvenient of this approach is that the BEM formulation will now present both strong singularities and hypersingularities, which have to be regularized before any numerical integration is possible. Successful hypersingular approaches have been developed by [47] for piezoelectric materials and [46] for MEE materials under static loadings. These works have been extended to the dynamic domain in [48] and [92, 93] for piezoelectric and MEE materials, respectively.

A remark is necessary when static loading is applied. In this case ($\omega = 0$), the terms from Eqs. (2.18) and (2.19) do not present frequency dependence. Moreover, the equilibrium equation given in Eq. (2.14) is simplified, since the inertial term is zero.

### 2.4.2 eXtended finite element method (X-FEM)

The motivation of X-FEM was to eliminate some of the deficiencies of standard FEM when concerning crack modelling. The excessive meshing aroung the crack-tips and the mandatory remeshing for crack growth problems are the most common problems. The partition of unity [9] allows to model discontinuities from the mesh through the enrichment of the classical finite elements. The enrichment consists in adding degrees of freedom (dofs) at the nodes representing the discontinuous surfaces position. In this framework, the mesh is independent from the discontinuities, remaining the same in crack growth problems.

Two types of enrichment functions are applied in the X-FEM: the Heaviside enrichment function, responsible for characterizing the discontinuity induced by the crack surfaces, which assumes the value $-1$ or $+1$ only; the crack-tip enrichment function (CTEF), responsible for spanning the displacements around the crack-tip. This latter presents complex behavior, varying for different constitutive laws (see [8, 38, 77], for some different CTEF). In this sense, it is similar to the FS, necessary in BEM formulations.

The displacement approximation $\mathbf{u}^h(\mathbf{x})$ with the partition of unity can be stated as [71]

$$\mathbf{u}^h(\mathbf{x}) = \sum_{i \in \mathcal{N}} N_i(\mathbf{x})\mathbf{u}_i + \sum_{j \in \mathcal{N}^{\mathcal{H}}} N_j(\mathbf{x})H(\mathbf{x})\mathbf{a}_j + \sum_{k \in \mathcal{N}^{\mathcal{CT}}} N_k(\mathbf{x}) \sum_{\alpha} F_\alpha(\mathbf{x})\mathbf{b}_k^\alpha \tag{2.20}$$

where $N_i$ is the standard finite element shape function associated with node $i$, $\mathbf{u}_i$ is the vector of nodal dofs for classical finite elements, and $\mathbf{a}_j$ and $\mathbf{b}_k^\alpha$ are the added set of degrees of freedom that are associated with enriched basis functions, associated with the Heaviside function $H(\mathbf{x})$ and the CTEF $F_\alpha(\mathbf{x})$, respectively.

Since the CTEF describe the displacements at the crack-tip zone through the addition of several dofs, the stress concentration around the crack-tip is more accurate with a significantly coarse mesh compared to the mesh used with standard FEM in a similar problem.

The presence of blending elements, which do not contain the crack but contain enriched nodes is also important to be considered . These elements were analyzed by [21], and some studies have improved the convergence of blending elements (see [40], for instance). The X-FEM convergence rate can also be increased through the use of geometrical enrichment [58], where a number of elements around the crack-tip receive the CTEF instead of a single element (this latter named topological enrichment).

# 3 Overall results of this Thesis

## 3.1 Damage identification in magnetoelectroelastic materials using artificial intelligence tools

In **Paper A**, the problem of damage identification in MEE materials is addressed for the first time to the author's best knowledge. Since a BEM formulation describing the behavior of a MEE material due to the presence of a crack-type defect was developed by [46], the use of a NN is suitable to model the inverse problem. In this case, the influence of a given crack damage in the displacements in part of the external boundary of a 2D MEE plate consists in the NN input, and the position of the crack-tips are taken as NN output. A sufficiently large input/output data set is created and is given to the NN to be able to recognize how different crack patterns affect the displacement response on the boundaries. The first approach with standard NN can be found in Figure 3.1 and it has shown that crack patterns over a certain size can be identified by the NN, while the remaining smaller cracks were not. Moreover, the NN calculated crack position were always in the center of the plate, showing the tendency of the NN to concentrate unidentifiable cracks in this region.

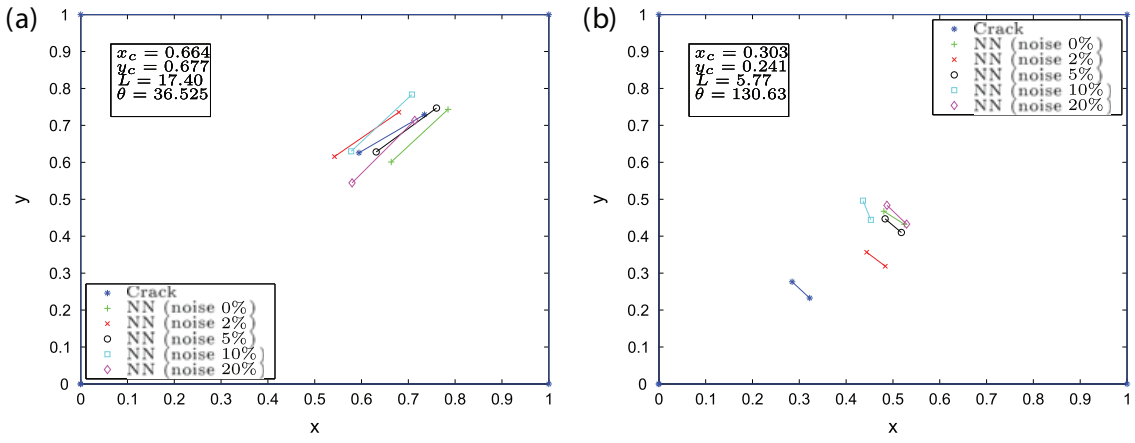


Figure 3.1: Damage identification with SNNs. From **Paper A**.

The proposed solution of the NN identification limitation is to perform a training set division (TSD) based on the center position of the crack patterns in the plate. The plate

is divided into five regions, a center one, which apparently is the most problematic region to identify, and four adjacent equally divided areas. The crack patterns contained in each of these regions are independent training sets, and have to be assigned to NN for training. The identification results seen in Figure 3.2 shows that the smaller crack patterns can be recognized by the new proposed NN identification framework.

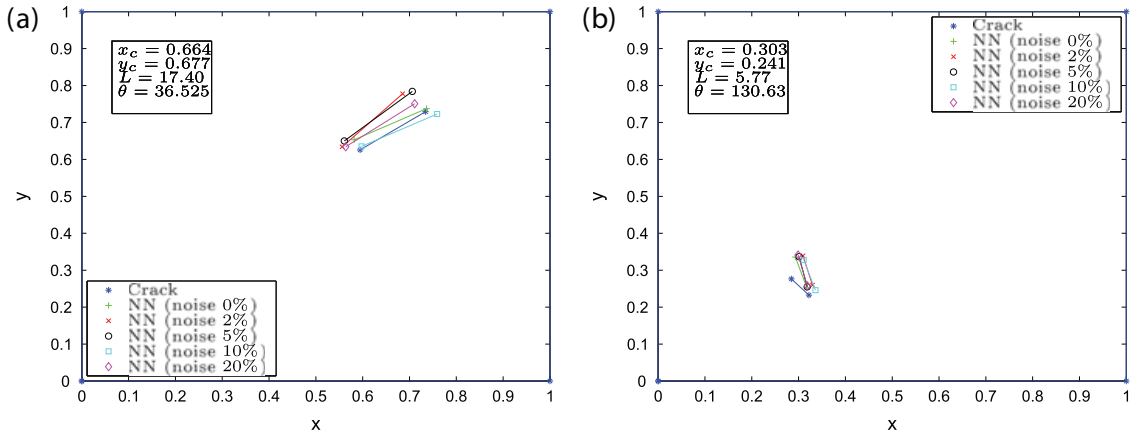


Figure 3.2: Damage identification for partitioned training set. From **Paper A**.

In order to analyze the sensitivity of the NN identification scheme, noise has been added to the training set. However, a different implementation of the noise was used. Given that the MEE damage identification framework is an ill-conditioned problem, small changes in the input (the displacement response) may cause a huge change in the output (crack parameters). Furthermore, the simple addition of the noise may put the input outside the training space, defined as the domain where the NN has been trained to recognize crack patterns. For these reasons, the noise was incorporated into the training set instead of being used the validation set to avoid this problem, expanding marginally the training domain to comport the noise. In this work, the validation set is used without noise in all cases to verify how NN trained with noisy inputs can recognize pristine inputs.

From **Paper A**, the approach used is effective but restricted to the analyzed case, since the TSD is realized using the fact that the NN had the tendency to classify the crack patterns in the center region. This kind of knowledge is not usually available when modeling the inverse problem. Hence, an automated classifier is desirable. In **Paper B**, the crack identification problem is approached by introducing another artificial intelligence tool, which will be responsible for dividing the training set. The self-organizing algorithms are designed to separate a number of elements considering only their intrinsic properties. In this Thesis, two of the most usual self-organizing algorithms were compared, the K-means algorithm [108] and the Gaussian mixtures (GM) [26] algorithm. To

make the separation easier, the Principal Component Analysis (PCA) [1] is employed to reduce the multidimensional NN input to a bidimensional vector, but conserving the information of the original input.

The K-means algorithm functionality is based on the minimization of the distance between a given element and the center of the formed groups (centroids). Since an element belongs to the closest centroid, an iterative method is calculated to find the optimum position of the centroids, therefore forming the desirable groups. The GM algorithm uses probabilistic theory to form the groups, by determining the probability of a given component to belong to a given group. The distribution probability is calculated by means of the Expectation Maximization (EM). In this work five training sets provide the optimum damage identification. The formation of more groups do not contribute to increase the accuracy of the damage identification, on the contrary, the identification performance is reduced due to the overfitting of the NN caused by the arise of groups with few elements. From Figure 3.3 it is easy to verify that the GM algorithm largely improves the identification results obtained with the NN.

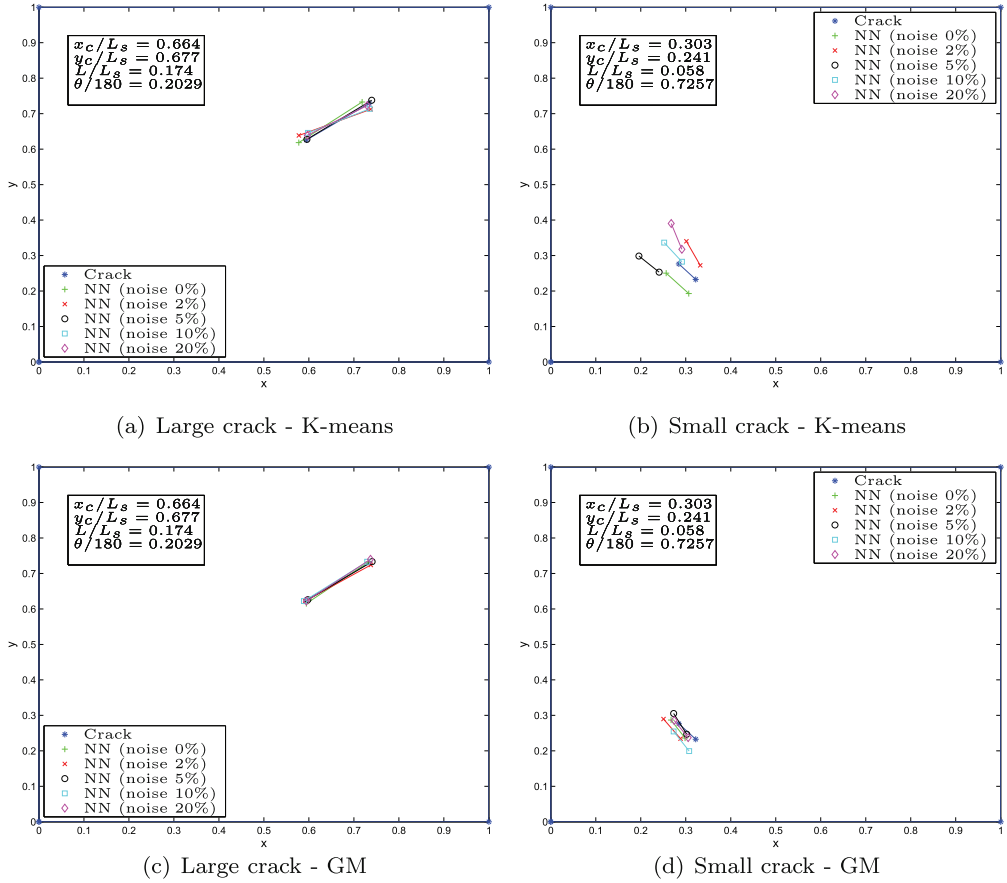


(a) Large crack - K-means

(b) Small crack - K-means

(c) Large crack - GM

(d) Small crack - GM

Figure 3.3: Crack identification. From **Paper B**.

## 3.2 A new enrichment function for 2D anisotropic materials for the X-FEM

The Stroh's formalism has been used previously to obtain Green's function for piezoelectric [13] and MEE materials [95]. The main advantage of this formulation is the possibility to calculate an explicit expression which depends on the material properties, regardless the orientation of the material and the geometry of the problem. The Stroh's formalism has been used to obtain the asymptotic displacements in the crack-tip by [124], and after some mathematical manipulation, the crack-tip enrichment function (CTEF) can be obtained.

Two types of enrichment strategy were used: the topological enrichment, where the CTEF is applied exclusively to the finite element which contains the crack-tip; and the geometrical enrichment, where all the nodes inside a given circumference centered at the crack-tip receive the CTEF. The isotropic CTEF was also used for comparison purposes. The convergence analysis has shown that the relative energy is the same with isotropic or anisotropic CTEF for topological enrichment. The anisotropic CTEF has a reduction of about 10 % in the relative energy compared to the isotropic CTEF with the geometrical enrichment.

In **Paper C** the interaction integral has been adopted to the calculation of the stress intensity factors (SIFs). This formulation is particularly suitable in FEM discretizations, because only the elements inside an arbitrary closed contour containing the crack-tip are used to obtain the SIFs.

For all presented numerical examples in **Paper C**, it was verified that the geometric enrichment is robust and accurate, presenting excelent agreement with numerical results obtained using the BEM, historically more accurate than FEM in fracture mechanics problems. The proposed anisotropic CTEF is general and can be used for any 2D anisotropic material.

## 3.3 Far field Green's functions for MEE materials under time-harmonic loading

The Green's functions valid in the far field were deduced using the works of Buchwald [19], Lighthill [61] and Sáez and Domínguez [103], where a combination of residue theory and the method of the stationary phase is used. In this method, the field variables are defined in terms of the Fourier transform, resulting in a triple integration formula. The residue theory can suppress one of this integrals, while the two remaining are approximated with the method of the stationary phase. From the method of stationary phase, the main contribution of a highly oscillatory integrand is due to the region where the oscillation is almost stationary. These regions are called critical points.

Using this methodology, the slowness surfaces of the MEE material have great relevance. The stationary points are defined where the normal on the slowness surface is parallel to the position vector, defined by the position where the load is applied and the position where the response is measured. The asymptotic displacements are then calculated solving Eq. (12) of **Paper D**, for all $N_H$ and $N_G$ critical points. From Payton [88], the number of stationary points is directly correlated to the material's crystal class. Duff [31] has shown that the quasi-longitudinal sheet is always convex, having only one stationary point, while Payton [88] has proved that the slowness sheet of the purely transversal motions is always convex. Therefore, it is necessary to find the number of stationary points of the quasi-shear motion slowness surface, which will contain at least one and up to three stationary points.

Due to the application of the quasi-static approximation, the electric and the magnetic coupling do not generate new slowness surface sheets. Instead, their presence affect the shape of some sheets, which depend also of the class of the material (cubic, hexagonal, tetragonal, etc).

This new FS can allow the study of damage identification in multifield materials with artificial intelligence tools in high frequencies, since the creation of the dataset of direct problems will not be penalized by the excessive computing time required to solve a single direct problem using the implicit FS. Moreover, most of the typical applications of multifield materials are performed in high frequencies, such as health monitoring, for instance.

## 3.4 An experimental approach for crack identification/assessment in piezoelectric materials

It was stated previously that damage identification in smart materials was given little attention. Experimental damage identification in such materials was even more neglected. One of the objectives of this Thesis is to provide insight of experimental damage identification in multifield materials. Piezoelectric (PZT) sensors were employed since they can be easily found commercially.

To quantify damage experimentally, a damage index (DI) is defined in **Paper E**, correlating the response of the pristine state of the piezoelectric material with the response measured after a defect is imposed. Several measures were taken on the surface of a damaged piezoelectric plate, placed on an aluminium plate. The excitation was provided by another PZT located in the middle of the opposite side of the aluminium plate. Then, a data fusion scheme is applied to obtain a graphic solution of the damage location and size.

Usually, data fusion schemes are based on sensing paths, defined as the path between a sensor from a given actuator. This scheme is very useful to quantify the damage influ-

ence over the structure. If the damage is close to a sensing path, the DI in this sensing path will have more importance than the measurement obtained from a sensing path that is far away from the damage. The response obtained from several sensing paths can be used to characterize the structural state. However, data fusion schemes efficiency is restricted in the actual experimental set-up since there is only one actuator. In addition, the difference of the measured responses from the undamaged and damaged state are very similar, further complicating the identification. Preliminary identification results led to no useful information about structural damage.

To overcome the limitation of a single sensing path available, a Gaussian mapping technique was applied to the DI. In this way the same information can be represented and the data fusion can be used to quantify the damage state of the PZT. This simple approach has been shown to enhance the structural damage information for several types of defects, including cracks and holes.

The degree of correlation in signals captured before and after the introduction of damage will clearly decrease if the sensing path is close to the damage due to the inclusion of damage-scattered wave components.

# 4 Conclusions and future work

In this thesis a new damage identification scheme was developed, using a combination of neural networks, self-organizing algorithms and the boundary element method. The considered damage was a crack-type defect. In the proposed approach, only part of the displacement solution calculated on the boundaries using the BEM was necessary to perform the damage identification. It was verified that standard NN were not able to properly recognize all possible crack patterns, then some modifications were necessary to overcome this limitation. In **Paper A**, a division of the training set was sufficient to greatly improve the crack identification results. However, the TSD was executed based on some *a priori* knowledge of the damage identification problem, which prevents the framework to be general. For this reason, the introduction of the self-organinzing algorithms in **Paper B** had the objective to obtain a TSD with an automated method, depending exclusively on the properties of the training set.

A new enrichment function for generally anisotropic bidimensional materials based on the Stroh's formalism was developed for the use with X-FEM in **Paper C**. The main advantage of the obtained enrichment function is that it is defined only by the materials properties, being independent of the adopted orientation. It was verified through examples in fracture mechanics that a regular X-FEM mesh can attain approximately the same accucacy obtained with BEM.

A new Green's function for MEE and piezoelectric materials was deduced for the far field in **Paper D**. An asymptotic approximation was obtained in a similar way as Buchwald [19] and Sáez and Domínguez [103] have calculated for transversely isotropic materials. The present symmetry of this kind of material allows a series of simplifications to be applied in the formulation, resulting in a more concise mathematical expression. Nevertheless, the methodology can be applied for generally anisotropic tridimensional piezoelectric and MEE materials.

Finally, an experimental scheme for damaged identification in piezoelectric material was studied in **Paper E**. Experimental measurements of the electric potential were taken on the surface of a commercial piezoelectric. A usual technique in experimental damage assessment is the data fusion, which consists in the calculation of a DI from data available of piezoelectric sensors which act as actuator or sensor. However, in this work only one sensor were available. The solution of this issue was to add a Gaussian mapping to the obtained DI, rescaling the data fusion so meaningful results can be obtained.

## 4.1 Future works

Several lines of work can be followed from the actual state of this Thesis. In terms of damage identification, the use of wavelets may be an important advance in the field, as it has been used by [4,36,70,79,98,120,141].

A unified theory of Stroh for an enrichment function may allow the calculation of a powerful general formulation, that can be applied from isotropic to generally anisotropic materials, including materials with coupling behavior as the piezoelectric and MEE materials. The challenge of the unified enrichment function is to obtain a reasonable number of enrichment functions to be calculated: for isotropic and anisotropic materials, 4 enrichment functions per node are required, while 6 and 8 are necessary for piezoelectric [13] and MEE [95] materials, respectively. However, the number of enrichment function for piezoelectric and MEE materials with the unifed theory would be 12 and 16, respectively, the double of the current enrichment functions for these materials. Further studies on enrichment functions and the Stroh's formalism are required.

Another theme of interest in fracture mechanics with BEM is to enhance the smart materials coupling by appending the thermal component into the MEE material. The thermal field has the particularity of affecting every other field (elastic, electric, magnetic), but in contrast no other field has influence over the thermal one, assuming a conservative system. The thermic coupling also adds a new issue to the formulation, due to a new domain integral arising. Reciprocity methods have been used to transform the domain integral into a boundary integral [57,69]. In the static domain, the thermal problem can be decoupled from the MEE problem, so the thermic variables can be calculated at first, then the remaining MEE problem can be solved. In the dynamic domain, the problem is fully coupled, then no simplifications can be applied beforehand. Furthermore, a new Green's function for time-harmonic loading has to be used. Several authors have dedicated to thermoanisotropy [2,5,111,112,131] and thermopiezoelectricity [44,45,78,125,143,144], to cite a few references.

It is known that the coupling properties of piezoelectric and MEE materials change when surpassing the Curie temperature. Some studies suggest that even for lower temperatures (for instance, half the material's Curie temperature), the coupling properties decline abruptely, due to a change of the crystal structure, from a piezoelectric to a non-piezoelectric form [107]. Some applications, as microelectronics, use widely smart materials under high temperatures. A nonlinear analysis would allow to quantify the change in the measured response due to the influence of high temperatures

Some issues concerning the boundary conditions (BC) on the crack faces in smart materials are still under discussion. Three types of boundary conditions have been assumed so far: the permeable BC, where the electric and magnetic field are unaffected by the presence of the crack, the impermeable BC, where the crack is totally isolated from the electric and magnetic field, and the semi-permeable BC, which is a more real-

istic BC. In this formulation, the electric and magnetic field are not completely isolated on the crack faces, allowing the passage of the electromagnetic field. Since the correct value of the electric and the magnetic potentials on the crack faces is not known previously, this nonlinear problem is solved by an iterative procedure. This issue has been addressed by [27,91] for the static domain and [60,117,137] for the time domain, but no works have been developed for the frequency domain, for example, the scattering of a P-wave due to the presence of a crack in MEE materials.

Other types of experimental damage identification are also of interest, among them one can cite the measurement of electrical changes for damage evaluation. The method consists in taking several measures of the electrical potential in a structure, and compare the response with a reference solution. If the measurements are different, it means that the material resistivity has changed, due to some damage or imperfection in the material. This method is purely experimental, so it would be a great breakthrough to obtain a numerical method for evaluating the resistivity of piezoelectric devices. This method has been successfully applied in composite structures, as can be seen in [3, 85, 128, 138, 145] to cite a few references.

# Bibliography


[1] H. Abdi and L. Williams. Principal component analysis. *Wiley Interdisciplinary Reviews: Computational Statistics*, 2:433–459, 2010.

[2] A. I. Abreu, A. Canelas, B. Sensale, and W. J. Mansur. CQM-based BEM formulation for uncoupled transient quasistatic thermoelasticity analysis. *Engineering Analysis with Boundary Elements*, 36(4):568–578, 2012.

[3] J. C. Abry, S. Bochard, A. Chateauminois, M. Salvia, and G. Giraud. In situ detection of damage in CFRP laminates by electrical resistance measurements. *Composites Science and Technology*, 59(6):925–935, 1999.

[4] K. F. Alvin, A. N. Robertson, G. W. Reich, and K. C. Park. Structural system identification: From reality to models. *Computers and Structures*, 81(12):1149–1176, 2003.

[5] W. T. Ang and D. L. Clements. Hypersingular integral equations for a thermoelastic problem of multiple planar cracks in an anisotropic medium. *Engineering Analysis with Boundary Elements*, 23(9):713–720, 1999.

[6] S. R. Anton and D. J. Inman. Reference-free damage detection using instantaneous baseline measurements. *AIAA JOURNAL*, 47(8):1952–1964, 2009.

[7] A. L. Araújo, C. M. M. Soares, J. Herskovits, and P. Pedersen. Parameter estimation in active plate structures using gradient optimisation and neural networks. *Inverse Problems in Science and Engineering*, 14(5):483–493, 2006.

[8] A. Asadpoure and S. Mohammadi. Developing new enrichment functions for crack simulation in orthotropic media by the extended finite element method. *International Journal for Numerical Methods in Engineering*, 69:2150–2172, 2007.

[9] I. Babuška and J. M. Melenk. The partition of unity method. *International Journal for Numerical Methods in Engineering*, 4:607–632, 1997.

[10] P. K. Banerjee and L. Morino. *Boundary Element Methods in Nonlinear Fluid Dynamics: Developments in boundary element methods*. Elsevier Science Publishers, 1990.

[11] D. M. Barnett and J. Lothe. Dislocations and line charges in anisotropic piezoelectric insulators. *Phys. stat. sol.*, 76:105–111, 1975.

[12] D. H. Bassir, S. Guessasma, and L. Boubakar. Hybrid computational strategy based on ann and gaps: Application for identification of a non-linear model of composite material. *Composite Structures*, 88(2):262–270, 2009.

[13] E. Béchet, M. Scherzer, and M. Kuna. Application of the X-FEM to the fracture of piezoelectric materials. *International Journal for Numerical Methods in Engineering*, 77:1535–1565, 2009.

[14] T. Belytschko and T. Black. Elastic crack growth in finite elements with minimal remeshing. *International Journal for Numerical Methods in Engineering*, 45:601–620, 1999.

[15] Y. Benveniste. Magnetoelectric effect in fibrous composites with piezoelectric and piezomagnetic phases. *Physical Review*, B 51:16424–16427, 1995.

[16] A. Boström. Review of hypersingular integral equation method for crack scattering and application to modeling of ultrasonic nondestructive evaluation. *Applied Mechanical Review*, 56(4):383–405, 2003.

[17] C. A. Brebbia and J. Domínguez. Boundary element methods for potential problems. *Applied Mathematical Modelling*, 1(7):372 – 378, 1977.

[18] C. A. Brebbia and J. Domínguez. *Boundary Elements: An Introductory Course (second edition)*. Computational Mechanics Publications, 1992.

[19] V. T. Buchwald. Elastic waves in anisotropic media. *Philosophical Transactions of the Royal Society of London. Series A, Mathematical and Physical Sciences*, 253(1275):563–580, 1959.

[20] F. C. Buroni and A. Sáez. Three-dimensional Green's function and its derivatives for materials with general anisotropic magneto-electro-elastic coupling. *Philosophical Transactions of the Royal Society of London. Series A, Mathematical and Physical Sciences*, 466:515–537, 2010.

[21] J. Chessa, H. Wang, and T. Belytschko. On the construction of blending elements for local partition of unity enriched finite elements. *International Journal for Numerical Methods in Engineering*, 57(7):1015–1038, 2003.

[22] C. H. Chue and T. J. C. Liu. Magnetoelectroelastic antiplane analysis of a bimaterial $BaTiO_3 - CoFe_2O_4$ composite wedge with an interface crack. *Theoretical and Applied Fracture Mechanics*, 44:275–296, 2005.

[23] I. Daubechies. The wavelet transform, time-frequency localization and signal analysis. *IEEE Transactions on Information Theory*, 36(5):961–1005, 1990.

[24] D. L. Davies and D. W. Bouldin. A cluster separation measure. *IEEE Transactions on Pattern Analysis and Machine Intelligence*, 1(2):224–227, 1979.

[25] W. F. Deeg. *The analysis of dislocation, crack and inclusion problems in piezoelectric solids*. PhD thesis, Stanford University, USA, 1980.

[26] A. P. Dempster, N. M. Laird, and D. B. Rubin. Maximum likelihood from incomplete data via the em algorithm. *Journal of the Royal Statistical Society. Series B (Methodological)*, 39(1):1–38, 1977.

[27] M. Denda. BEM analysis of semipermeable piezoelectric cracks. *Key Engineering Materials*, 383:67–84, 2008.

[28] M. Denda, Y. Araki, and Y. K. Yong. Time-harmonic BEM for 2-D piezoelectricity applied to eigenvalue problems. *International Journal of Solids and Structures*, 26:7241–7265, 2004.

[29] E. DiPasquale, J.-W. Ju, A. Askar, and A. S. Cakmak. Relation between global damage indices and local stiffness degradation. *Journal of structural engineering New York, N.Y.*, 116(5):1440–1456, 1990.

[30] J. Dominguez. *Boundary Elements in Dynamics*. Computational Mechanics Publications, 1993.

[31] G. F. D. Duff. The Cauchy problem for elastic waves in an anisotropic medium. *Philosophical Transactions of the Royal Society of London. Series A, Mathematical and Physical Sciences*, 252(1010):pp. 249–273, 1960.

[32] J. C. Dunn. Well-separated clusters and optimal fuzzy partitions. *Journal of Cybernetica*, 4(1):95–104, 1974.

[33] O. V. Estorff. *Boundary Elements in Acoustics: Advances & Applications*. WIT Press, 2000.

[34] C. Fan, M. Zhao, J. Wang, and E. Pan. Analysis of an arbitrarily oriented crack in a finite piezoelectric plane via the hybrid extended displacement discontinuity-fundamental solution method. *Computational Mechanics*, 51(4):567–580, 2013.

[35] C. Fan, Y. Zhao, M. Zhao, and E. Pan. Analytical solution of a semi-permeable crack in a 2D piezoelectric medium based on the ps model. *Mechanics Research Communications*, 40:34–40, 2013.

[36] W. Fan and P. Qiao. A 2-D continuous wavelet transform of mode shape data for damage detection of plate structures. *International Journal of Solids and Structures*, 46(25-26):4379–4395, 2009.

[37] W. Fan and P. Qiao. Vibration-based damage identification methods: A review and comparative study. *Structural Health Monitoring*, 10(1):83–111, 2011.

[38] M. Fleming, Y. A. Chu, B. Moran, and T. Belytschko. Enriched element-free Galerkin methods for crack tip fields. *International Journal for Numerical Methods in Engineering*, 40:1483–1504, 1997.

[39] F. D. Foresee and M. T. Hagan. Gauss-Newton approximation to Bayesian learning. In *International Conference in Neural Networks*, volume 3, pages 1930–1935, 1997.

[40] T. P. Fries. A corrected xfem aproximation without problems in blending elements. *International journal for numerical methods in engineering*, 75:503–532, 2008.

[41] M. I. Friswell. Damage identification using inverse methods. *Philosophical Transactions of the Royal Society A: Mathematical, Physical and Engineering Sciences*, 365(1851):393–410, 2007.

[42] C. F. Gao, H. Kessler, and H. Balke. Crack problems in magnetoelectroelastic solids. Part I: exact solution of a crack. *International Journal of Engineering Science*, 41:969–981, 2003.

[43] C. F. Gao, H. Kessler, and H. Balke. Crack problems in magnetoelectroelastic solids. Part II: General solution of collinear cracks. *International Journal of Engineering Science*, 41:983–994, 2003.

[44] C. F. Gao, P. Tong, and T. Y. Zhang. Fracture mechanics for a mode III crack in a magnetoelectroelastic solid. *International Journal of Solids and Structures*, 41:6613–6629, 2004.

[45] C.-F. Gao and M.-Z. Wang. Collinear permeable cracks in thermopiezoelectric materials. *Mechanics of Materials*, 33(1):1–9, 2001.

[46] F. García-Sánchez, R. Rojas-Díaz, A. Sáez, and C. Zhang. Fracture of magnetoelectroelastic composite materials using boundary element method (BEM). *Theoretical and Applied Fracture Mechanics*, 47(3):192–204, 2007.

[47] F. García-Sánchez, A. Sáez, and J. Domínguez. Anisotropic and piezoelectric materials fracture analysis by BEM. *Computer and Structures*, 83:804–820, 2005.

[48] F. García-Sánchez, C. Zhang, and A. Sáez. 2-D transient dynamic analysis of cracked piezoelectric solids by a time-domain BEM. *Computer Methods in Applied Mechanics and Engineering*, 197, 33-40:3108–3121, 2008.

[49] J. Hadamard. Sur les problmes aux dérivées partielles et leur signification physique. *Princeton University Bulletin*, 13:49–52, 1902.

[50] R. J. Hanson. Numerical method for solving fredholm integral equations of the first kind using singular values. *SIAM Journal on Numerical Analysis*, 8(3):616–622, 1971.

[51] S. Haykin. *Neural Networks: A Comprehensive Foundation*. Prentice Hall, Upper Saddle River, NJ, USA, 2nd edition, 1999.

[52] R. K. Ing and M. Fink. Time-reversed lamb waves. *IEEE Transactions on Ultrasonics, Ferroelectrics and Frequency Control*, 45(4):1032–1043, 1998.

[53] S. I. Ishak, G. R. Liu, H. M. Shang, and S. P. Lim. Locating and sizing of delamination in composite laminates using computational and experimental methods. *Composites: Part B*, 32(4):287–298, 2001.

[54] L. Z. Jiang and C. T. Sun. Analysis of indentation cracking in piezoceramics. *International Journal of Solids and Structures*, 38(10-13):1903–1918, 2001.

[55] X. Jiang and E. Pan. Exact solution for 2D polygonal inclusion problem in anisotropic magnetoelectroelastic full-, half-, and bimaterial-planes. *International Journal of Solids and Structures*, 41:4361–4382, 2004.

[56] L. A. Klein. *Sensor and Data Fusion Concepts and Applications*. SPIE Press, Bellingham, 1999.

[57] M. Kögl and L. Gaul. A boundary element method for anisotropic coupled thermoelasticity. *Archive of Applied Mechanics*, 73(5-6):377–398, 2003.

[58] P. Laborde, J. Pommier, Y. Renard, and M. Salaün. High-order extended finite element method for cracked domains. *International Journal for Numerical Methods in Engineering*, 64:354–381, 2005.

[59] S. J. Lee, H. Sohn, and J. W. Hong. Time reversal based piezoelectric transducer self-diagnosis under varying temperature. *Journal of Nondestructive Evaluation*, 29(2):75–91, 2010.

[60] J. Lei, Q. Yang, and C. Zhang. Transient response of a semi-permeable crack between dissimilar anisotropic piezoelectric layers by time-domain BEM. *Engineering Analysis with Boundary Elements*, 37(10):1205–1211, 2013.

[61] M. J. Lighthill. Studies on magneto-hydrodynamic waves and other anisotropic wave motions. *Philosophical Transactions of the Royal Society of London. Series A, Mathematical and Physical Sciences*, 252(1014):397–430, 1960.

[62] B. Liu, D. N. Fang, A. K. Soh, and K. C. Hwang. An approach for analysis of poled/depolarized piezoelectric materials with a crack. *International Journal of Fracture*, 111(4):395–407, 2001.

[63] Y. Lu, L. Ye, Z. Su, L. Zhou, and L. Cheng. Artificial neural network (ANN)-based crack identification in aluminium plates with Lamb wave signals. *Journal of Intelligent Material Systems and Structures*, 20:39–49, 2009.

[64] C. S. Lynch, W. Yang, L. Collier, Z. Suo, and R. M. McMeeking. Electric field induced cracking in ferroelectric ceramics. *Ferroelectrics*, 166(1-4):11–30, 1995.

[65] F. Magalhes, A. Cunha, and E. Caetano. Online automatic identification of the modal parameters of a long span arch bridge. *Mechanical Systems and Signal Processing*, 23(2):316–329, 2009.

[66] N. M. M. Maia, J. M. M. Silva, E. A. M. Almas, and R. P. C. Sampaio. Damage detection in structures: From mode shape to frequency response function methods. *Mechanical Systems and Signal Processing*, 17(3):489–498, 2003.

[67] A. Mal, F. Ricci, S. Banerjee, and F. Shih. A conceptual structural health monitoring system based on vibration and wave propagation. *Structural Health Monitoring*, 4(3):283–293, 2005.

[68] G. D. Manolis and D. E. Beskos. *Boundary element methods in elastodynamics*. Unwin Hyman, 1988.

[69] T. Matsumoto, A. Guzik, and M. Tanaka. A boundary element method for analysis of thermoelastic deformations in materials with temperature dependent properties. *International Journal for Numerical Methods in Engineering*, 64(11):1432–1458, 2005.

[70] M. Meo, G. Zumpano, M. Piggott, and G. Marengo. Impact identification on a sandwich plate from wave propagation responses. *Composite Structures*, 71(3-4):302–306, 2005.

[71] N. Möes, J. Dolbow, and T. Belytschko. A finite element method for crack growth without remeshing. *International Journal for Numerical Methods in Engineering*, 46:131–150, 1999.

[72] J. E. Mottershead and M. I. Friswell. Model updating in structural dynamics: A survey. *Journal of Sound and Vibration*, 167(2):347–375, 1993.

[73] S. Mustapha, L. Ye, D. Wang, and Y. Lu. Debonding detection in composite sandwich structures based on guided waves. *AIAA Journal*, 50(8):1697–1706, 2012.

[74] F. Narita, Y. Morikawa, Y. Shindo, and M. Sato. Dynamic fatigue behavior of cracked piezoelectric ceramics in three-point bending under ac electric fields. *Journal of the European Ceramic Society*, 32(14):pp. 3759–3766, 2012.

[75] D. E. Newland. Wavelet analysis of vibration, part I: Theory. *Journal of Vibration and Acoustics*, 116:409–416, 1994.

[76] D. E. Newland. Wavelet analysis of vibration, part II: Wavelet maps. *Journal of Vibration and Acoustics*, 116:417–425, 1994.

[77] C. C. Nobile, L. Fracture analysis for orthotropic cracked plates. *Composite Structures*, 68(3):285–293, 2005.

[78] Y. Ootao and Y. Tanigawa. Transient analysis of multilayered magneto-electro-thermoelastic strip due to nonuniform heat supply. *Composite Structures*, 68(4):471 – 480, 2005.

[79] A. Ovanesova and L. Suárez. Applications of wavelet transforms to damage detection in frame structures. *Engineering Structures*, 26(1):39–49, 2004.

[80] Y. E. Pak. Linear electro-elastic fracture mechanics of piezoelectric materials. *International Journal of Fracture*, 54:79–100, 1992.

[81] R. Palma, G. Rus, and R. Gallego. Probabilistic inverse problem and system uncertainties for damage detection in piezoelectrics. *Mechanics of Materials*, 41(9):1000–1016, 2009.

[82] Y. Z. Pappas, Y. P. Markopoulos, and V. Kostopoulos. Failure mechanisms analysis of 2D carbon/carbon using acoustic emission monitoring. *Applied Mechanics Reviews*, 64(3), 2011.

[83] G. Park, C. R. Farrar, F. L. Di Scalea, and S. Coccia. Self-diagnosis and validation of active sensors used for structural health monitoring. *Proceedings of SPIE - The International Society for Optical Engineering*, 6173, 2006.

[84] H. W. Park, H. Sohn, K. H. Law, and C. R. Farrar. Time reversal active sensing for health monitoring of a composite plate. *Journal of Sound and Vibration*, 302:50–66, 2007.

[85] J. B. Park, T. Okabe, N. Takeda, and W. A. Curtin. Electromechanical modeling of unidirectional CFRP composites under tensile loading condition. *Composites - Part A: Applied Science and Manufacturing*, 33(2):267–275, 2001.

[86] S. B. Park and C. T. Sun. Fracture criteria for piezoelectric ceramics. *Journal of American Ceramics Society*, 78:1475–1480, 1995.

[87] V. Z. Parton and B. A. Kudryatsev. *Electromagnetoelasticity*. Gordon and Breach science publisher, New York, 1988.

[88] R. G. Payton. *Elastic wave propagation in transversely isotropic media*. M. Nijhoff Publishers, 1983.

[89] H. Power, C. A. Brebbia, and D. B. Ingham. *Boundary Element Methods in Fluid Dynamics II*. WIT Press, 1994.

[90] P. Rizzo and F. L. di Scalea. Feature extraction for defect detection in strands by guided ultrasonic waves. *Structural Health Monitoring*, 5(3):297–308, 2006.

[91] R. Rojas-Díaz, M. Denda, F. García-Sánchez, and A. Sáez. Dual BEM analysis of different crack face boundary conditions in 2D magnetoelectroelastic solids. *European Journal of Mechanics, A/Solids*, 31(1):152–162, 2012.

[92] R. Rojas-Díaz, F. García-Sánchez, and A. Sáez. Analysis of cracked magnetoelectroelastic composites under time-harmonic loading. *International Journal of Solids and Structures*, 47:71–80, 2010.

[93] R. Rojas-Díaz, F. García-Sánchez, A. Sáez, and C. Zhang. Dynamic crack interactions in magnetoelectroelastic composite materials. *International Journal of Fracture*, 157:119–130, 2009.

[94] R. Rojas-Díaz, A. Sáez, F. García-Sánchez, and C. Zhang. Time-harmonic Green's functions for anisotropic magnetoelectroelasticity. *International Journal of Solids and Structures*, 45:144–158, 2008.

[95] R. Rojas-Díaz, N. Sukumar, A. Sáez, and F. García-Sánchez. Fracture in magnetoelectroelastic materials using the extended finite element method. *International Journal for Numerical Methods in Engineering*, 88:1238–1259, 2011.

[96] L. Rokach and O. Maimon. Clustering methods. In O. Maimon and L. Rokach, editors, *The data mining and knowlegde discovery handbook*, pages 321–352. Springer, 2010.

[97] V. Rokhlin. Rapid solution of integral equations of classical potential theory. *Journal of Computational Physics*, 60(2):187 – 207, 1985.

[98] M. Rucka and K. Wilde. Application of continuous wavelet transform in vibration based damage detection method for beams and plates. *Journal of Sound and Vibration*, 297(3-5):536–550, 2006.

[99] L. I. Rudin, S. Osher, and E. Fatemi. Nonlinear total variation based noise removal algorithms. *Physica D: Nonlinear Phenomena*, 60(1-4):259–268, 1992.

[100] G. Rus, R. Palma, and J. L. Pérez-Aparicio. Optimal measurement setup for damage detection in piezoelectric plates. *International Journal of Engineering Science*, 47:554–572, 2009.

[101] G. Rus, R. Palma, and J. L. Pérez-Aparicio. Experimental design of dynamic model-based damage identification in piezoelectric ceramics. *Mechanical Systems and Signal Processing*, 26(1):268–293, 2012.

[102] A. Rytter. *Vibration based inspection of civil engineering structures*. PhD thesis, Department of Building Technology, Aalborg University, Denmark, 1993.

[103] A. Sáez and J. Domínguez. Far field dynamic Green's functions for BEM in transversely isotropic solids. *Wave motion*, 32 (2):113–123, 2000.

[104] O. Salawu. Detection of structural damage through changes in frequency: a review. *Engineering Structures*, 19(9):718 – 723, 1997.

[105] R. P. C. Sampaio, N. M. M. Maia, and J. M. M. Silva. Damage detection using the frequency-response-function curvature method. *Journal of Sound and Vibration*, 226(5):1029–1042, 1999.

[106] G. B. Santoni, L. Yu, B. Xu, and V. Giurgiutiu. Lamb wave-mode tuning of piezoelectric wafer active sensors for structural health monitoring. *Journal of Vibration and Acoustics*, 129:752–762, 2007.

[107] M. J. Schulz, M. J. Sundaresan, J. McMichael, D. Clayton, R. Sadler, and B. Nagel. Piezoelectric materials at elevated temperature. *Journal of Intelligent Material Systems and Structures*, 14(11):693–705, 2003.

[108] S. Z. Selim and M. A. Ismail. K-means-type algorithms: A generalized convergence theorem and characterization of local optimality. *IEEE Transactions on Pattern Analysis and Machine Intelligence*, PAMI-6(1):81–87, 1984.

[109] S. S. M. Seth, S. K. and S. Constantinos. Damage detection in composite materials using Lamb wave methods. *Smart Materials and Structures*, 11(2):269–278, 2002.

[110] K. Sharma, T. Q. Bui, C. Zhang, and R. R. Bhargava. Analysis of a subinterface crack in piezoelectric bimaterials with the extended finite element method. *Engineering Fracture Mechanics*, 104:pp. 114–139, 2013.

[111] Y. C. Shiah and C. L. Tan. Exact boundary integral transformation of the thermoelastic domain integral in BEM for general 2D anisotropic elasticity. *Computational mechanics*, 23(1):87–96, 1999.

[112] Y. C. Shiah and C. L. Tan. Fracture mechanics analysis in 2-D anisotropic thermoelasticity using BEM. *CMES - Computer Modeling in Engineering and Sciences*, 1(3):91–99, 2000.

[113] Y. Shindo, H. Murakami, K. Horiguchi, and F. Narita. Evaluation of electric fracture properties of piezoelectric ceramics using the finite element and single-edge precracked-beam methods. *Journal of the American Ceramic Society*, 85(5):1243–1248, 2002.

[114] Y. Shindo, M. Oka, and K. Horiguchi. Analysis and testing of indentation fracture behavior of piezoelectric ceramics under an electric field. *Journal of Engineering Materials and Technology, Transactions of the ASME*, 123(3):293–300, 2001.

[115] J. Sladek, V. Sladek, P. Solek, and E. Pan. Fracture analysis of cracks in magneto-electro-elastic solids by the MLPG. *Computational Mechanics*, 42:697–714, 2008.

[116] J. Sladek, V. Sladek, P. H. Wen, and Y. C. Hon. Inverse fracture problems in piezoelectric solids by local integral equation method. *Engineering Analysis with Boundary Elements*, 33:1089–1099, 2009.

[117] J. Sladek, V. Sladek, C. Zhang, and M. Wünsche. Semi-permeable crack analysis in magnetoelectroelastic solids. *Smart Materials and Structures*, 21(2), 2012.

[118] M. D. Snyder and T. A. Cruse. Boundary-integral analysis of anisotropic cracked plates. *International Journal of Fracture mechanics*, 315-328, 1975.

[119] A. K. Soh and J. X. Liu. On the constitutive equations of magnetoelectroelastic solids. *Journal of Intelligent Material Systems and Structures*, 16:597–602, 2005.

[120] H. Sohn, G. Park, J. R. Wait, N. Limback, and C. R. Farrar. Wavelet-based active sensing for delamination detection in composite structures. *Smart Materials and Structures*, 13(1):153–160, 2004.

[121] Z. Su and L. Ye. Lamb wave-based quantitative identification of delamination in CF/EP composite structures using artificial neural algorithm. *Composite Structures*, 66(1-4):627–637, 2004.

[122] Z. Su and L. Ye. *Identification of Damage using Lamb waves*. Springer, London, UK, 2009.

[123] N. Sukumar, Z. Y. Huang, J. H. Prévost, and Z. Suo. Partition of unity enrichment for bimaterial interface cracks. *International Journal for Numerical Methods in Engineering*, 59:1075–1102, 2004.

[124] Z. Suo. Singularities, interfaces and cracks in dissimilar anisotropic media. *Proceedings of the Royal Society of London. Series A, Mathematical and Physical Sciences*, 427(1873):331–358, 1990.

[125] J.-Q. Tarn and H.-H. Chang. A refined state space formalism for piezothermoelasticity. *International Journal of Solids and Structures*, 45(10):3021 – 3032, 2008.

[126] A. Tikhonov and V. Arsénine. Méthodes de résolution de problmes mal posés. *MIR*, 1976.

[127] A. G. Tobin and E. Pak. Effect of electric fields on fracture behavior of PZT ceramics. In *Proceedings of the Smart Structures and Materials*, 1993.

[128] A. Todoroki and Y. Tanaka. Delamination identification of cross-ply graphite/epoxy composite beams using electric resistance change method. *Composites Science and Technology*, 62(5):629 – 639, 2002.

[129] C. Valle and J. W. Littles. Flaw localization using the reassigned spectrogram on laser-generated and detected Lamb modes. *Ultrasonics*, 39(8):535–542, 2002.

[130] J. van Suchtelen. Product properties: A new application of composite materials. *Philips Research Reports*, 27(1):28–37, 1972.

[131] B. L. Wang and J. C. Han. Multiple cracking of magnetoelectroelastic materials in coupling thermo-electro-magneto-mechanical loading environments. *Computational Materials Science*, 39(2):291–304, 2007.

[132] C. Y. Wang and J. D. Achenbach. Elastodynamic fundamental solutions for anisotropic solids. *Geophysical Journal International*, 18:384–392, 1994.

[133] C. Y. Wang and J. D. Achenbach. 3-D time-harmonic elastodynamic Green's functions for anisotropic solids. *Philosophical Transactions of the Royal Society of London. Series A, Mathematical and Physical Sciences*, 449:441–458, 1995.

[134] L. C. Wrobel and C. A. .Brebbia. *Boundary element methods in heat transfer*. Computational Mechanics Publications, 1992.

[135] T. L. Wu and J. H. Huang. Closed-form solutions for the magnetoelectric coupling coefficients in fibrous composites with piezoelectric and piezomagnetic phases. *International Journal of Solids and Structures*, 37(21):2981–3009, 2000.

[136] T. W. Wu. *Boundary Element Acoustics: Fundamentals and Computer Codes*. WIT Press, 2000.

[137] M. Wünsche, C. Zhang, F. García-Sánchez, A. Sáez, J. Sladek, and V. Sladek. Dynamic crack analysis in piezoelectric solids with non-linear electrical and mechanical boundary conditions by a time-domain BEM. *Computer Methods in Applied Mechanics and Engineering*, 200(41-44):2848–2858, 2011.

[138] Z. H. Xia and W. A. Curtin. Damage detection via electrical resistance in CFRP composites under cyclic loading. *Composites Science and Technology*, 68(12):2526–2534, 2008.

[139] Y. G. Xiu, G. R. Liu, Z. P. Wu, and X. M. Huang. Adaptive multilayer perceptron networks for detection of cracks in anisotropic laminated plates. *Internation Journal of Solids and Structures*, 38:5625–5645, 2001.

[140] L. H. Yam, Y. Y. Li, and W. O. Wong. Sensitivity studies of parameters for damage detection of plate-like structures using static and dynamic approaches. *Engineering Structures*, 24(11):1465–1475, 2002.

[141] L. H. Yam, Y. J. Yan, and J. S. Jiang. Vibration-based damage detection for composite structures using wavelet transform and neural network identification. *Composite Structures*, 60(4):403–412, 2003.

[142] B. L. Yang, X. M. Zhuang, T. H. Zhang, and X. Yan. Damage mode identification for the clustering analysis of AE signals in thermoplastic composites. *Journal of Nondestructive Evaluation*, 28(3-4):163–168, 2009.

[143] S. W. Yu and Q. H. Qin. Damage analysis of thermopiezoelectric properties: Part I - crack tip singularities. *Theoretical and Applied Fracture Mechanics*, 25(3):263–277, 1996.

[144] S. W. Yu and Q. H. Qin. Damage analysis of thermopiezoelectric properties: Part II. effective crack model. *Theoretical and Applied Fracture Mechanics*, 25(3):279 – 288, 1996.

[145] A. E. Zantout and O. I. Zhupanska. On the electrical resistance of carbon fiber polymer matrix composites. *Composites Part A: Applied Science and Manufacturing*, 41(11):1719–1727, 2010.

[146] X. C. Zhong and X. F. Li. Magnetoelectroelastic analysis for an opening crack in a piezoelectromagnetic solid. *European Journal of Mechanics*, 26:405–417, 2007.

# 5 Appended papers

## Paper A: Damage identification in multifield materials using neural networks

The original version of this paper can be found in **www.tandfonline.com**

- DOI:10.1080/17415977.2013.792079
- Journal Name: Inverse Problems in Science and Engineering
- ISSN:1741-5977 (print) ; 1741-5985 (online)
- ISI 2011 Classification: Q3 (51/90) Impact factor: 0.622
- SCIMAGO 2011 Classification: Q2 (112/359) SJR: 0.357

# Damage identification in multifield materials using neural networks

Authors: Gabriel Hattori and Andrés Sáez

ABSTRACT

Smart materials structures with multifield coupling properties have been widely used in the latter years. Some methodologies have been developed to study fracture problems in piezoelectric and magnetoelectroelastic (MEE) materials using the boundary element method (BEM). However, relatively limited attention has been paid to inverse problems. Identification problems are usually ill-conditioned, which implies that gradient search methods might not have a good performance, whilst Newton based search methods are computationally expensive. Additionally, the presence of noise in the measured data affects the convergence of these methods. In this paper we study the application of neural networks to damage identification of multifield materials, in particular to MEE materials. A particular training set division (TSD) has been applied to improve the identification results, even for high noise levels. A hypersingular BEM is used to obtain the solution of the direct problem (elastic displacements and magnetic and electric potentials) and create the training set.

**Keywords**: Inverse problems; Multifield materials; Fracture mechanics; Neural networks; Boundary element method

## A.1 Introduction

Smart or multifield materials have gained special attention in latter years due to their ample range of applications, from sensors in structural health monitoring to transducers in medical devices. Such applications take advantage of their coupling properties among different fields: mechanical and electric in piezoelectric materials; mechanical, electric and magnetic in magnetoelectroelastic (MEE) materials. Many of these materials exhibit brittle behavior, which means damage is susceptible to appear, due to operating conditions or even during the manufacture process. This issue has encouraged several authors to analyze the behavior of these materials analytically [7, 8, 13, 28] or numerically [5, 18, 21, 31], to cite a few works. However, little attention has been given to damage identification in smart materials.

Damage identification is a ramification of inverse problems [26]. Several numerical or analytical formulations have been proposed in the literature (see for example

[12, 14, 25]). Nowadays, ordinary methods are gradually being replaced by artificial intelligent techniques to model damage identification, since they do not require a speficic inverse formulation of the problem. Instead, these methods use the solution of the direct problem, i.e, the effect of the damage in the response, to model the inverse problem. With this objective, Comino et al. [6] introduced genetic algorithms and topologic derivatives to solve inverse problems in anisotropic plates. Lu et al. [16] applied neural networks to identify cracks in aluminium plates. A large list of authors could be cited for structural damage identification. Nevertheless, the references are limited when it comes to damage identification in smart materials: in reference [22] genetic algorithms and the finite element method were used to identify holes in piezoelectric ceramics, while in [17] probabilistic theory was applied for damage identification. To the authors' best knowledge, no work for damage identification in MEE materials has been presented so far.

The objective of the present study is to analyze the application of the neural networks in damage identification of MEE materials. For this purpose, the formulation by García-Sánchez et al. [9] for 2D static fracture analysis of MEE materials is employed to solve the direct problem for different sizes, position and crack orientations. These data are used as input to a back-propagation neural network [11]. A trained neural network will identify the crack location of the input data, and should be able to identify cracks of non-trained inputs. The noise sensitivity of the neural network was also verified.

This paper is organized as follows. The governing equations of MEE materials are stated in Section 2. The direct problem is described in Section 3 and the inverse problem is depicted in Section 4. The obtained numerical results are shown in Section 5. Concluding remarks are presented in Section 6.

## A.2 Magnetoelectroelastic governing equations

The linear MEE 2D problem can be represented in an elastic like way by generalizing Barnett and Lothe's approach [3] for piezoelectric materials. An extended displacement vector $u_I$ is defined that includes the elastic components $u_i$, the electric potential $\phi$ and the magnetic potential $\varphi$, as

$$u_I = \begin{cases} u_i, & \text{I=1,2} \\ \varphi, & \text{I=4} \\ \phi, & \text{I=5} \end{cases} \tag{A.1}$$

where the lowercase subscripts vary from 1 to 2, whereas the uppercase ones take the values 1,2 (elastic), 4 (electric) and 5 (magnetic). A generalized stress tensor $\sigma_{iJ}$ can also

be defined as

$$\sigma_{iJ} = \begin{cases} \sigma_{ij}, & \text{J=1,2} \\ D_i, & \text{J=4} \\ B_i, & \text{J=5} \end{cases} \tag{A.2}$$

with an associated generalized traction vector

$$p_I = \begin{cases} p_i = \sigma_{ij} n_j, & \text{I=1,2} \\ D = D_j n_j, & \text{I=4} \\ B = B_j n_j, & \text{I=5} \end{cases} \tag{A.3}$$

where $\sigma_{ij}$ represents the mechanical stress tensor, $D_i$ are the components of the electric displacement, $B_i$ stands for the components of the magnetic induction vector, and $\mathbf{n} = (n_1, n_2)$ are the components of the normal vector to the boundary.

The MEE constitutive equations may them be written as [24]

$$\sigma_{iJ} = C_{iJKl} u_{K,l} \tag{A.4}$$

where the material properties have been grouped together into a generalized elasticity tensor $C_{iJKl}$ defined as

$$C_{iJKl} = \begin{cases} c_{ijkl} & J,K = 1,2 & e_{lij} & J = 1,2;\ K = 4 & h_{lij} & J = 1,2;\ K = 5 \\ e_{ikl} & J = 4;\ K = 1,2 & -\epsilon_{il} & J,K = 4 & -\beta_{il} & J = 4;\ K = 5 \\ h_{ikl} & J = 5;\ K = 1,2 & -\beta_{il} & J = 5;\ K = 4 & -\gamma_{il} & J,K = 5 \end{cases} \tag{A.5}$$

with $c_{ijkl}$, $\epsilon_{il}$, $\gamma_{il}$, $e_{lij}$, $h_{lij}$ and $\beta_{il}$ being the elastic stiffness, the dielectric permittivities and the magnetic permeabilities tensors, and the piezoelectric, the piezomagnetic and the electromagnetic coupling coefficients, respectively.

## A.3 Direct BEM formulation for crack problems in MEE materials

Linear elastic fracture mechanics is one of the areas where the BEM has clearly demonstrated being a powerful and effective numerical method when compared to other computational techniques. Among its advantages one may cite that: (i) discretization of only the boundary is required; thus simplifying preprocessing and remeshing in crack growth analysis, (ii) it shows improved accuracy in stress concentration problems, since there are no approximations imposed on the stress solution at the interior domain points, or (iii) fracture parameters (stress intensity factors, energy release rates, etc.) may be accurately determined from the computed nodal data in a straightforward manner [1, 15].

The training data set for the neural network (NN) will be generated from numerical simulations performed using the dual BEM formulation proposed by García-Sánchez et al. [9] for 2D static fracture problems of MEE materials. This approach will be implemented to solve the corresponding direct problem for different cracks with varying sizes, locations and orientations.

Let $\Omega$ be a 2D MEE cracked domain with boundary $\Gamma$, so that $\Gamma = \Gamma_{crack} \cup \Gamma_c$, where $\Gamma_{crack} = \Gamma_+ \cup \Gamma_-$ are two geometrically coincident crack surfaces and $\Gamma_c$ denotes the rest of the (crack-free) boundary. The dual formulation of the BEM makes use of both the generalized displacement boundary integral equation (BIE)

$$c_{IJ}u_J + \int_\Gamma p^*_{IJ}u_J d\Gamma = \int_\Gamma u^*_{IJ}p_J d\Gamma \tag{A.6}$$

and the generalized traction BIE

$$c_{IJ}p_J + \int_\Gamma s^*_{IJ}u_J d\Gamma = \int_\Gamma d^*_{IJ}p_J d\Gamma \tag{A.7}$$

to overcome the difficulty imposed by having two coincident crack boundaries that would lead to a degeneracy in case of considering only the standard displacement BIE. In Eqs. (A.6) and (A.7), $u^*_{IJ}$ and $p^*_{IJ}$ stand for the fundamental solution displacements and tractions, respectively; $d^*_{IJ}$ and $s^*_{IJ}$ follow from differentiation of $u^*_{IJ}$ and $p^*_{IJ}$ and further substitution into the constitutive equations (A.4); $c_{IJ}$ are the free terms arising from the Cauchy principal value integration of the fundamental solution kernels. Eqs. (A.6) and (A.7) hold in the absence of generalized body forces, eletric charge density and electric current density.

Further details about the BEM formulation and its validation are given in [9], where aspects like meshing strategy, implemented fundamental solutions, evaluation of fracture parameters and integrations schemes are explained thoroughly. In particular, the BEM formulation in [9] is detailed for cracks that are self-equilibrated from a mechanical point of view and are electrically and magnetically impermeable, i.e.,

$$\Delta p_I = p^+_I + p^-_I = 0 \tag{A.8}$$

where the superscripts $+$ and $-$ stand for the upper and lower crack surfaces. In such cases, it suffices to apply the displacement BIE for collocation nodes on $\Gamma_c$ and the traction BIE for collocation nodes on either face of the crack, say $\Gamma_+$

$$c_{IJ}u_J + \int_{\Gamma_c} p^*_{IJ}u_J d\Gamma + \int_{\Gamma_+} p^*_{IJ}\Delta u_J d\Gamma = \int_{\Gamma_c} u^*_{IJ}p_J d\Gamma \tag{A.9}$$

$$p_J + \int_{\Gamma_c} s^*_{IJ}u_J d\Gamma + \int_{\Gamma_+} s^*_{IJ}\Delta u_J d\Gamma = \int_{\Gamma_c} d^*_{IJ}p_J d\Gamma \tag{A.10}$$

to yield a complete set of equations to compute the generalized displacements and tractions on $\Gamma_c$ and the generalized crack opening displacements $\Delta u_I = u_I^+ - u_I^-$ on $\Gamma_{crack}$. In Eq. (A.10) the free term is set to 1 because of the additional singularity arising from the coincidence ot the two crack surfaces.

## A.4 Inverse problem

Several techniques have been developed in order to solve different types of inverse problems [20]. Analytical techniques are very effective but can only be applied for simple configurations. Moreover, due to ill-conditioning, there is no guarantee of a (unique) solution to the problem.

When the behavior of the physical system is too complex or not entirely known, a black box model may be chosen to represent the inverse problem. For this purpose, the neural networks were widely used in structural inverse problems [27], damage identification [16, 29], or parameters estimation [2], among many applications.

An artificial NN is a system made by numerous simple structural units called neurons, that are arranged in layered structures. The particular properties of the NN include a parallel way to process information and the learning by experience feature, which allows the NN to reutilize the acquired experience. The NN can be trained to have a specific function through the adjustment between the neurons connections [11].

We consider a back-propagation NN scheme, as Figure A.1 sketches. The output of the NN is given by

$$y_{kn} = f(\sum w_{kj} y_{jn}) \tag{A.11}$$

where $w_{kj}$ represent the weights linkage between the $n$th neuron of the $k$th layer and the $j$th input, $f(\cdot)$ is the transfer function, defined as

$$f(v) = \begin{cases} \frac{exp(v)-exp(-v)}{exp(v)+exp(-v)} & \text{for hidden and input layers} \\ v & \text{for output layer} \end{cases} \tag{A.12}$$

with $exp$ as the exponential function. Let us remark that Eq. (A.12) can be repeated recursively for $y_{jn}$ until the input layer, where $y_{jn}$ is replaced by the network input $q_{in}$. The NN output error $e_{kn}$ is defined as $e_{kn} = y_{kn} - t_{kn}$, where $t_{kn}$ is the target parameter.

The mean square error (MSE) is defined as the sum of all quadratic errors for all $n$ neurons of the output layer, for every $M$ input of the training set, and it is expressed by

$$\overline{\epsilon} = \frac{1}{2M} \sum_{i=1}^{M} \sum_{j=1}^{n} (y_{kn} - t_{kn})^2 \tag{A.13}$$

The training rule is based on the minimization of the MSE, reducing the error until

some acceptable tolerance. In this work the Levenberg-Marquardt algorithm is applied as training rule (see [10] for details).

Next both a standard NN and an improved NN with training set division will be implemented and their performance analyzed on a practical crack identification example.

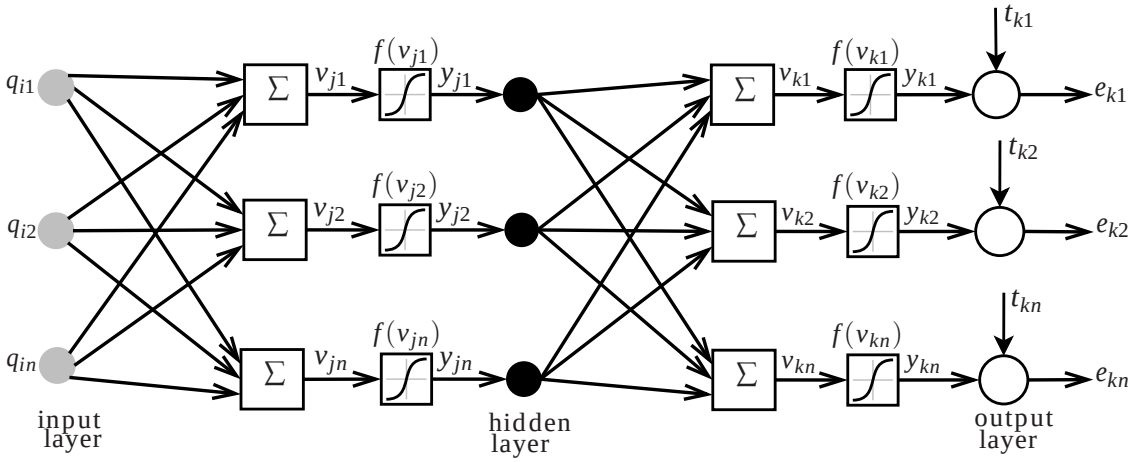


Figure A.1: Scheme of the a back-propagation neural network.

## A.5 Numerical results and discussion

### A.5.1 Analyzed problem

A square 2D plate with dimensions $L_x = L_y = 8$ cm of a MEE $BaTiO_3 - CoFe_2O_4$ composite with a volumetric fraction of $V_f = 0.5$ is considered in this work. The material properties are given in Table A.1. The crack parameters range is summarized in Table A.2, where $x_c$ and $y_c$ indicate the crack center, $L$ denotes the crack length and $\theta$ represents the crack orientation with respect to the $x$ direction, as shown in Figure A.2. In what follows the crack center coordinates $(x_c, y_c)$ are normalized dividing their respectives values by the plate length $L_x$, obtaining a 0 to 1 scale in function of the plate side dimension. The crack length is normalized in %, to the plate dimension $L_x$.

For the analyzed problems, it was assumed that only the extended displacement solution on the right side ($x = L_x$) was known. Twelve measurements points have been considered. The applied load considered is a unitary uniformly distributed mechanic load, as depicted in Figure A.2.

As stated previously, a dual BEM has been implemented to numerically solve the direct problem. The external boundary of the plate has been discretized with six quadratic elements per side. The crack boundary was discretized using ten discontinuous quadratic elements, where the crack tip elements are discontinuous quarter-point (see [23, 9]).

Table A.1: Material properties for MEE $BaTiO_3 - CoFe_2O_4$ composite with $V_f = 0.5$.

| Properties | $BaTiO_3$ | $CoFe_2O_4$ | $V_f = 0.5$ |
|---|---|---|---|
| $C_{11}(GPa)$ | 166 | 286 | 226 |
| $C_{12}(GPa)$ | 78 | 170 | 125 |
| $C_{22}(GPa)$ | 162 | 269.5 | 216 |
| $C_{66}(GPa)$ | 43 | 45.3 | 44 |
| $e_{16}(C/m^2)$ | 11.6 | 0 | 5.8 |
| $e_{21}(C/m^2)$ | -4.4 | 0 | $-2.2$ |
| $e_{22}(C/m^2)$ | 18.6 | 0 | 9.3 |
| $\epsilon_{11}(\times 10^{-10} C^2/Nm^2)$ | 112 | 0.8 | 56.4 |
| $\epsilon_{12}(\times 10^{-10} C^2/Nm^2)$ | 126 | 0.93 | 63.5 |
| $h_{16}(N/Am)$ | 0 | 550 | 275 |
| $h_{21}(N/Am)$ | 0 | 580.3 | 290.2 |
| $h_{22}(N/Am)$ | 0 | 699.7 | 350 |
| $\gamma_{11}(\times 10^{-6} Ns^2/C^2)$ | 5 | 590 | 297 |
| $\gamma_{12}(\times 10^{-6} Ns^2/C^2)$ | 10 | 157 | 350 |
| $\beta_{11}(\times 10^{-12} Ns/VC)$ | – | – | 5.367 |
| $\beta_{12}(\times 10^{-12} Ns/VC)$ | – | – | 2737.5 |

Table A.2: Crack parameters range.

| | $x_c$ | $y_c$ | $L(\%L_x)$ | $\theta$ |
|---|---|---|---|---|
| min | 0.1875 | 0.1875 | 3.125 | 0 |
| max | 0.8125 | 0.8125 | 25.00 | 180 |

### A.5.2 Neural network parameters

The following neural network parameters were selected through trial-and-error:

- Architecture: $N_i$ neurons in the input layer, 25 neurons in the first hidden layer, 20 neurons in the second hidden layer and 4 neurons in the output layer.
- Training set: 1500 input / output entries
- Validation set: 1500 input / output entries;
- Training algorithm: Levenberg-Marquardt [10];
- Goal MSE: $1 \times 10^{-5}$.
- Maximum number of iterations: 100.

The training set was selected among random possibilities to obtain a uniform distribution of the damage parameters. Early stopping [19] was applied in every NN. The

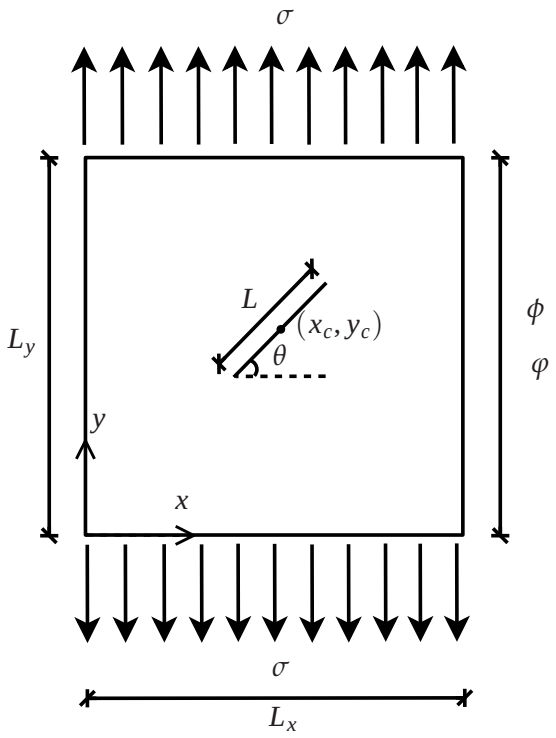


Figure A.2: Scheme of the direct problem.

training set is composed of 1500 inputs, where 600 are used in training and 600 in the validation. The validation set has the purpose of inspectioning the evolution of the NN error for non trained inputs. If the error of the validation set starts increasing, the NN training is interrumpted to prevent overfitting. The remaining 300 inputs are used to evaluate the performance of the NN.

The NN were trained with three different types of inputs. For one case, only the electric potential $\phi$ was given as training information to the NN. Then, only the magnetic potential $\varphi$ was given as input. Finally, a combination of electric and magnetic potential has been used as NN input. If simple entries are used, $N_i = 12$, otherwise $N_i = 24$.

A validation error (VE) is defined as the distance between real and identified parameters like [22]

$$\text{Validation Error} = VE = \frac{\sqrt{\sum (y-t)^2}}{\sum t} \tag{A.14}$$

where $y$ and $t$ are the identified and real parameters, respectively. The NN output are the crack tips positions, defined by the parameters $x_c$, $y_c$, $L$ and $\theta$. These parameters were taken in their normalized form as shown in Table A.2, and the orientation parameter $\theta$ was normalized dividing its value in degrees by 180.

Additionally, a variable *dist* was introduced to verify the quality of the identification provided by the NN, defined as

$$dist = \frac{1}{2}\left(\sqrt{(x_{g_1} - x_1)^2 + (y_{g_1} - y_1)^2} + \sqrt{(x_{g_2} - x_2)^2 + (y_{g_2} - y_2)^2}\right) \tag{A.15}$$

where $(x_1, y_1)$ and $(x_2, y_2)$ are the coordinates of the crack tips predicted by the NN and $(x_{g_1}, y_{g_1})$ y $(x_{g_2}, y_{g_2})$ are the actual coordinates of the crack tips.

The influence of noise was also considered. At the present work, pseudo-experimental inputs were created by adding noise to the numerical results [22] as stated in Eq. (A.16)

$$u_I^{exp} = u_I^* + \varrho\xi\sqrt{\frac{1}{N_i}\sum_{i=1}^{N_i} u_I^{*2}} \tag{A.16}$$

where $\varrho$ is the amount of noise, varying from 0 to 0.2. $\xi$ is a random variable with mean 0 and standard deviation 1. The root mean square (RMS) is used as an estimation of the differences that are noted from the predicted values $u_I^{exp}$ to the real observation $u_I^*$. The NN input is the distortion caused by the presence of the damage in the plate and is defined as

$$u_I^* = u_I - u_I^0 \tag{A.17}$$

where $u_I$ and $u_I^0$ are the extended displacement solution, i.e., the electric potential, the magnetic potential, or a combination of both, for a damaged and undamaged plate, respectively.

Two crack configurations were employed to check the accuracy of the different damage identification approaches, as depicted in Figures A.3(a) and A.3(b).

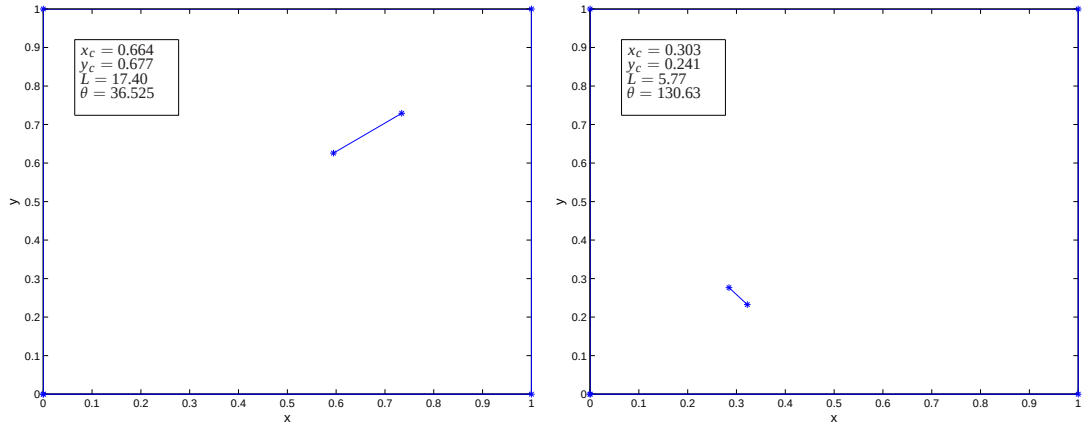


(a) Large crack (b) Small crack

Figure A.3: Reference cracks

### A.5.3 Damage identification with standard neural networks (SNN)

As an initial approach, the use of a standard neural network will be considered for the identification of different types of cracks. Table A.3 contains the identification results for different inputs and noise levels for the reference cracks.

Table A.3: Crack identification of the reference cracks for standard neural networks.

| Large crack - Fig. A.3(a) | | | | | |
|---|---|---|---|---|---|
| Noise | Input | $x_c$ | $y_c$ | $L(\%L_x)$ | $\theta$ |
| Real crack | | 0.6645 | 0.6775 | 17.40 | 36.525 |
| 0% | $\varphi$ | 0.65887 | 0.69319 | 17.9649 | 47.3811 |
| | $\phi$ | 0.60064 | 0.65961 | 19.5449 | 45.6093 |
| | $\varphi;\phi$ | 0.72415 | 0.67208 | 18.7203 | 49.5334 |
| 5% | $\varphi$ | 0.66779 | 0.6684 | 18.4642 | 43.9075 |
| | $\phi$ | 0.60869 | 0.67894 | 20.3594 | 51.1768 |
| | $\varphi;\phi$ | 0.69575 | 0.68753 | 17.5319 | 42.7067 |
| 20% | $\varphi$ | 0.65921 | 0.63103 | 17.0954 | 40.523 |
| | $\phi$ | 0.63244 | 0.694 | 18.0284 | 47.5609 |
| | $\varphi;\phi$ | 0.64676 | 0.62902 | 21.576 | 51.6481 |
| Small crack - Fig. A.3(b) | | | | | |
| Real crack | | 0.3034 | 0.2545 | 5.77 | 130.63 |
| 0% | $\varphi$ | 0.41499 | 0.46291 | 5.6909 | 110.2559 |
| | $\phi$ | 0.48112 | 0.47546 | 5.0827 | 116.3737 |
| | $\varphi;\phi$ | 0.50256 | 0.44989 | 5.623 | 141.1442 |
| 5% | $\varphi$ | 0.38293 | 0.42109 | 6.3789 | 118.1424 |
| | $\phi$ | 0.45828 | 0.49505 | 4.8963 | 101.9654 |
| | $\varphi;\phi$ | 0.50059 | 0.42833 | 5.0722 | 133.2922 |
| 20% | $\varphi$ | 0.44047 | 0.51858 | 5.9013 | 106.443 |
| | $\phi$ | 0.49 | 0.49836 | 7.0933 | 93.9798 |
| | $\varphi;\phi$ | 0.50823 | 0.45806 | 6.5904 | 129.6393 |

To illustrate these results, Figures A.4(a) and A.4(b) show the identification calculated by the NN for different levels of noise and applying the electric and magnetic potentials as inputs of the standard NN. The large crack is identified with reasonable precision for all applied noise levels (Figure A.4(a)). However, the NN provides a bad identification for the small crack (Figure A.4(b)).

### A.5.4 Training set division (TSD)

The SNN is not able to perform an accurate identification for small crack patterns. In this work, the position of the identified small crack given by the SNN is always close to the central area of the plate. One possible explanation of this fact is that the SNN can not reduce the error for this pattern without sacrificing the generalization capability of the NN (early stopping), since a small crack represents just a small distortion of the response at the boundaries.

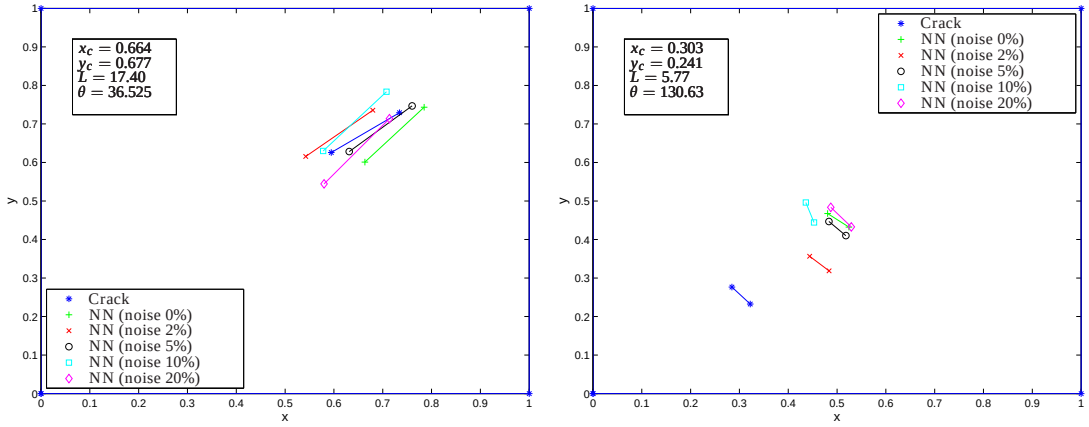


(a) (b)

Figure A.4: Damage identification with standard neural networks. Input: eletric and magnetic potentials $\varphi; \phi$.

The solution considered to overcome this limitation was to divide the training set. This approach was successfully implemented by Benders et al. [4] and Zhao [30] for modular NN, which consist in a divide-and-conquer procedure. In this formulation, a complex task is separated in several sub-tasks, and a central integration machine is responsible for assembling the final solution. In our case the training set has been divided into five regions: a central region defined by a circle of radius 1.75/8 plus four equally distributed regions as depicted in Figure A.5. The central regionis defined to better check the performance of the resulting TSD approach, once observed the tendency of the SNN to sistematically predict the position of the small cracks around the center of the plate. Subsequently, the patterns of each region were trained by individual NN. The parameter selected to uniquely define whether a particular crack belongs to one of these five regions is the crack center position.

The approach used in the present work is similar to the ones found in modular NN. However, in the present work each NN has been trained with patterns for a specific region, therefore it is only able to identify the cracks in its corresponding area. Each individual NN can provide a crack identification result, so there is no need of a central integration machine to give the final crack identification.

Figure A.6 presents the NN mean square error, the mean validation error (MVE) over the trained NN, number of training iterations and the number of valid identification patterns according to the parameter *dist* and the MVE. The MVE shows a slow increase with the noise, which indicates the generalization capabilities of the NN are little affected by noise increments. However, one can observe the decay of precision with increase of noise levels. In all NN inputs the number of reasonable identified patterns

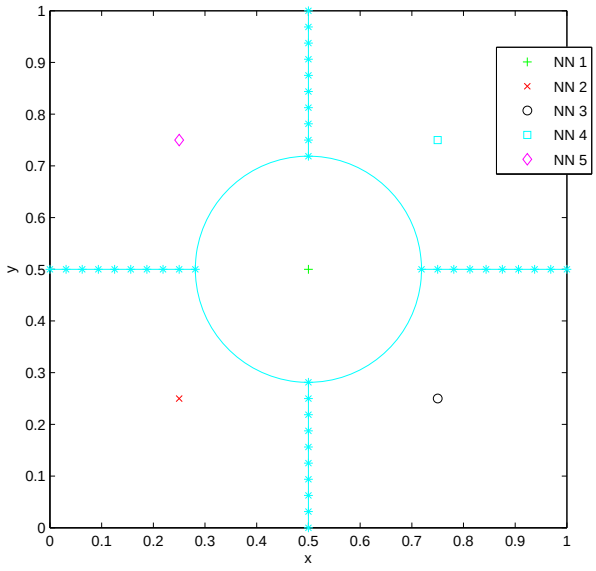


Figure A.5: Training set division.

is located between 70% (for high noise levels) and 90% (no noise). Through evaluation of the identification of randomly chosen cracks, it was verified that reasonable identification results exhibit values up to 0.2 of the *dist* parameter and MVE up to 0.5.

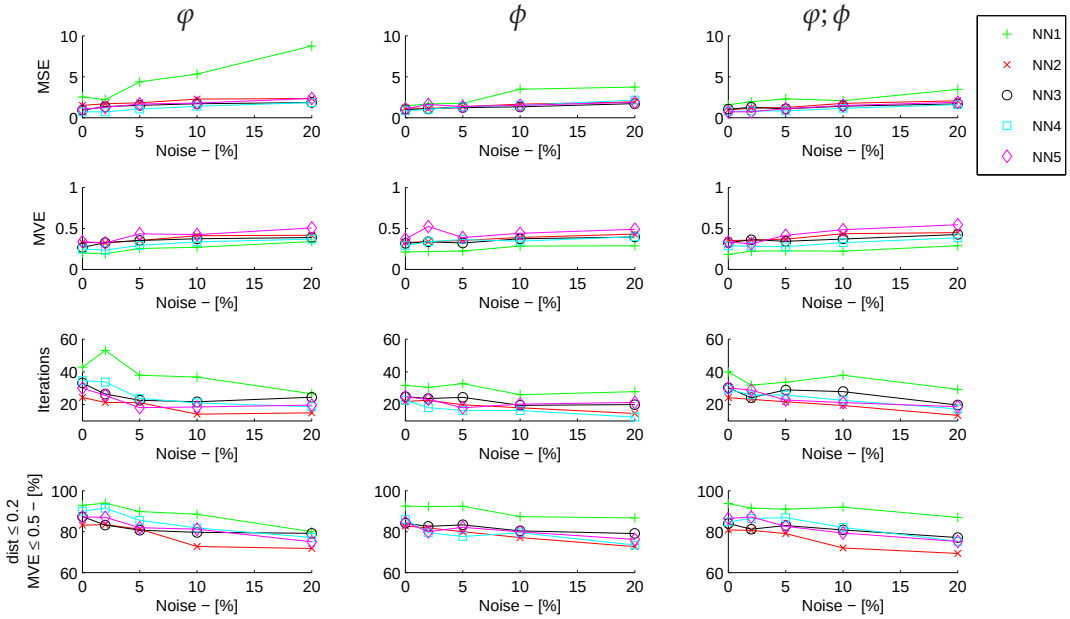


Figure A.6: NN training parameters.

Figures A.7(a) and A.7(b) illustrate the identification results of the reference cracks

for the combined electric and magnetic potentials input.

Table A.4 shows the identification results of the reference cracks for every division and the noiseless case only. Non reliable crack identification is obtained when evaluating an input that does not belong to the correct TSD. For the large crack identification, crack configurations outside the plate are found. For the small crack identification, only NN2 (the region where the real crack is placed in our example), predicts a crack center located inside its training space. Meanwhile, NN1, NN3, NN4 and NN5 predict a crack center position that, although inside the limits of the plate, is outside their respective training spaces, thus disproving the validity of the identification results. As expected, in all the numerical tests performed with TSD, there is only one NN that predicts the crack center position within the limits of its own training space.

Table A.5 contains the relevant information for the other NN input types. After adopting the training set division, the NN perform a good damage identification for all crack patterns and noise levels.

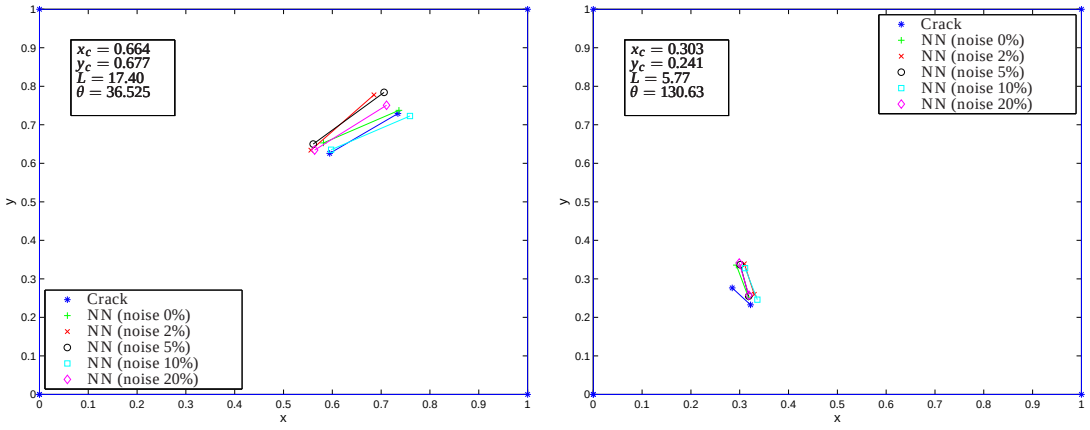


(a) (b)

Figure A.7: Damage identification for partitioned training set. Input: eletric and magnetic potentials $\varphi; \phi$.

Figure A.8 details the patterns distribution for each NN in function of the *dist* parameter and considering the MVE lower than 0.5. The quality of the identification results is similar for NN 2 to NN 5, for all types of inputs. The larger presence of NN 1 is due to the difference in the number of elements, since this NN includes more training patterns that the others NN. Most of the analysed inputs have $0.05 \leq dist \leq 0.1$, which does not denote a perfect identification but still represent a good approximation of the real crack, particularly when noise is present. Hence, it confirms that the applied training set division is a good method to improve the accuracy of the NN.

Figures A.9 and A.10 compare the SNN and TSD in terms of the *dist* parameter, considering the combination of electric and magnetic potentials as inputs of the NN. From

Table A.4: Detail of the crack identification of the reference cracks. Input: eletric and magnetic potentials $\varphi;\phi$. Noiseless case.

| Large crack - Fig. A.3(a) | | | | |
|---|---|---|---|---|
| Division | $x_c$ | $y_c$ | $L(\%L_x)$ | $\theta$ |
| Real crack | 0.6645 | 0.6775 | 17.40 | 36.525 |
| NN1 | −0.0751 | −0.4222 | 11.7723 | 107.2144 |
| NN2 | 1.8310 | 1.0303 | 22.1265 | 82.3948 |
| NN3 | 0.3564 | −0.0291 | 14.2854 | 46.1595 |
| NN4 | 0.65921 | 0.69524 | 17.6001 | 28.6191 |
| NN5 | 0.2472 | −0.0274 | 3.4812 | 104.4277 |
| Small crack - Fig. A.3(b) | | | | |
| Real crack | 0.3034 | 0.2545 | 5.77 | 130.63 |
| NN1 | 0.3281 | 0.2477 | 14.2822 | 17.6224 |
| NN2 | 0.30552 | 0.29391 | 8.6892 | 106.6033 |
| NN3 | 0.3731 | 0.0368 | 17.9431 | 140.8951 |
| NN4 | 0.1364 | 0.9880 | 21.4755 | 77.0152 |
| NN5 | 0.2539 | 0.4145 | 17.3986 | 117.3591 |

Table A.5: NN crack identification of the reference cracks. Training set division.

| Large crack - Fig. A.3(a) | | | | | |
|---|---|---|---|---|---|
| Noise | Input | $x_c$ | $y_c$ | $L(\%L_x)$ | $\theta$ |
| Real crack | | 0.6645 | 0.6775 | 17.40 | 36.525 |
| 0% | $\varphi$ | 0.63108 | 0.71814 | 19.666 | 35.3246 |
| | $\phi$ | 0.69849 | 0.67507 | 19.1954 | 37.0037 |
| | $\varphi;\phi$ | 0.65921 | 0.69524 | 17.6001 | 28.6191 |
| 5% | $\varphi$ | 0.67208 | 0.68629 | 16.7503 | 33.8668 |
| | $\phi$ | 0.66473 | 0.688 | 17.2202 | 28.074 |
| | $\varphi;\phi$ | 0.63343 | 0.71694 | 19.7807 | 42.7372 |
| 20% | $\varphi$ | 0.68213 | 0.69602 | 17.3683 | 26.0387 |
| | $\phi$ | 0.71882 | 0.67688 | 15.5476 | 36.2791 |
| | $\varphi;\phi$ | 0.6374 | 0.69253 | 18.777 | 38.2878 |
| Small crack - Fig. A.3(b) | | | | | |
| Real crack | | 0.3034 | 0.2545 | 5.77 | 130.63 |
| 0% | $\varphi$ | 0.30761 | 0.29776 | 4.5854 | 112.5911 |
| | $\phi$ | 0.32413 | 0.28823 | 9.0529 | 99.0733 |
| | $\varphi;\phi$ | 0.30552 | 0.29391 | 8.6892 | 106.6033 |
| 5% | $\varphi$ | 0.3304 | 0.28197 | 4.6299 | 102.8331 |
| | $\phi$ | 0.31884 | 0.29312 | 7.8783 | 103.9154 |
| | $\varphi;\phi$ | 0.30974 | 0.29582 | 8.3484 | 102.0944 |
| 20% | $\varphi$ | 0.31 | 0.30484 | 8.3622 | 106.1683 |
| | $\phi$ | 0.30557 | 0.30174 | 7.0414 | 106.8252 |
| | $\varphi;\phi$ | 0.30889 | 0.29928 | 8.5941 | 103.2668 |

Figure A.9, the SNN provides the best identification results when using the electric as only input of the NN. The correct identification rate is up to 80% for the noiseless

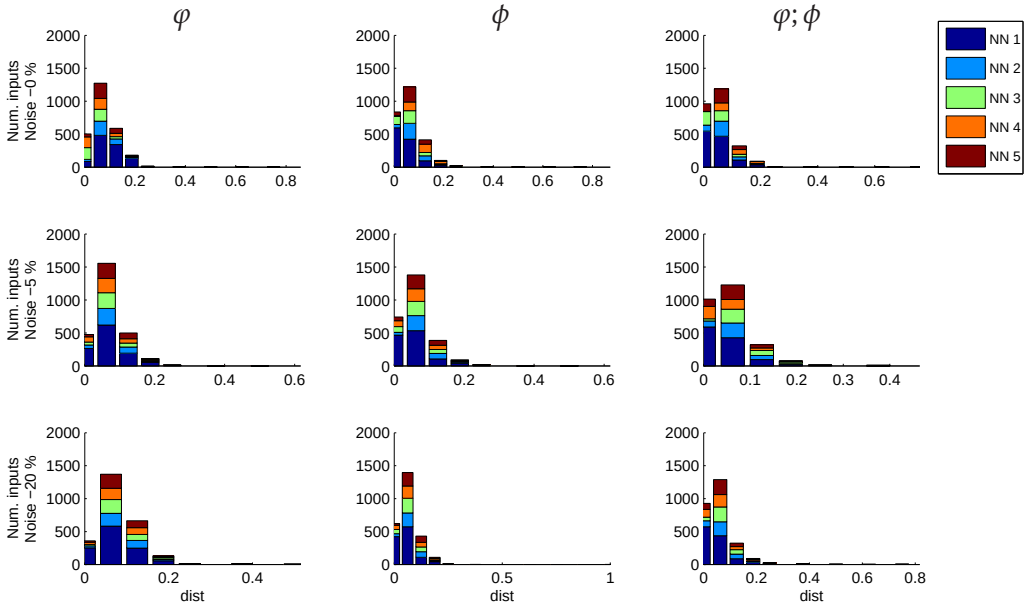


Figure A.8: *dist* parameter histograms with VE lower than 0.5. Training set division. Input: eletric and magnetic potentials $\varphi; \phi$.

cases, and decreases to 60% for high noise levels. However, considering the same input type, the identification results obtained with the TSD approach are noise insensitive, with minimal correct identification results of 75% for high noise levels, up to 90% when noise is disconsidered. From Figure A.10, the distribution of the *dist* parameter is similar for both methods when noise is zero. Nevertheless, the number of inputs where $dist = 0$ is considerable higher with the TSD approach, specially for high noise level cases.

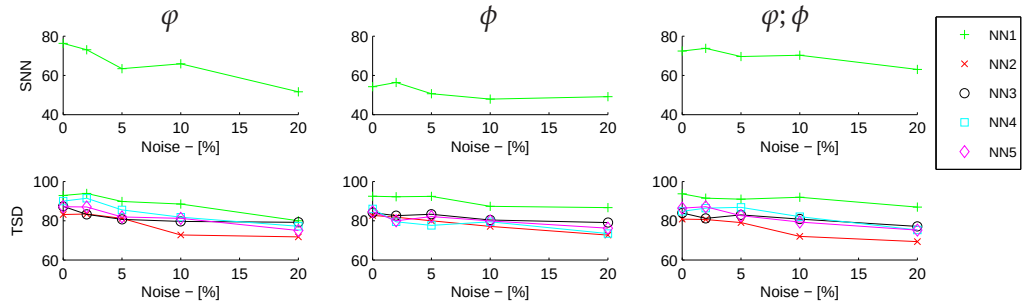


Figure A.9: *dist* parameter for several noise levels. Input: eletric and magnetic potentials $\varphi; \phi$.

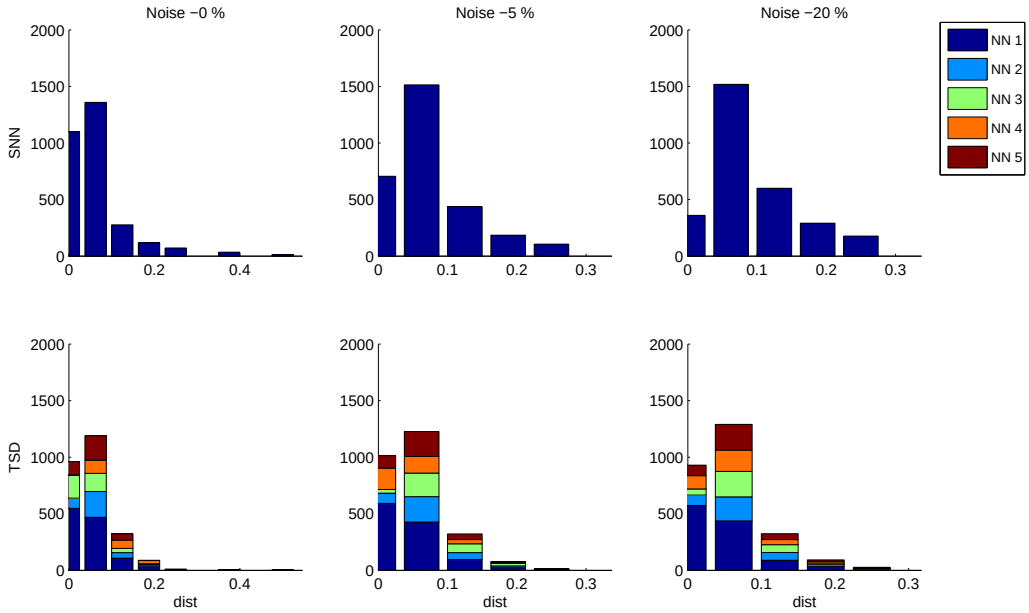


Figure A.10: *dist* parameter histograms for several noise levels. Input: eletric and magnetic potentials $\varphi; \phi$.

## A.6 Summary and conclusions

This work presents a new damage identification framework for MEE materials using an artificial intelligence tool. It is shown that SNN are not capable to identify all types of crack patterns correctly. To overcome this limitation, a division of the training set (TSD) was adopted, with each part being assigned to independent NN. This division was based in regions of the plate, using the fact that the SNN has the tendency to identify cracks in the central area of the plate. The identifications results after the TSD have largely improved. In general, the neural networks present good results in identifying a crack using only some partial information of the BEM solution. The input type affects the identification behavior of the networks. Better results are achieved when using the combination of electric and magnetic potentials rather than any of these potentials alone, as it could be expected. The NN simulation may be used as a good estimation of the crack location in MEE materials.

## Acknowledgments

This work was funded by the *Ministerio de Ciencia e Innovación*, Spain, research project DPI2010-21590-C02-02.

## Bibliography


[1] M. H. Aliabadi. Boundary element formulations in fracture mechanics. *Applied Mechanics Reviews*, 50(2):83–96, 1997.

[2] A. L. Araújo, C. M. M. Soares, J. Herskovits, and P. Pedersen. Parameter estimation in active plate structures using gradient optimisation and neural networks. *Inverse Problems in Science and Engineering*, 14(5):483–493, 2006.

[3] D. M. Barnett and J. Lothe. Dislocations and line charges in anisotropic piezoelectric insulators. *Phys. stat. sol.*, 76:105–111, 1975.

[4] T. Bender, V. S. Gordon, and M. Daniels. Partitioning strategies for Modular Neural Networks. In *Proceedings of International Joint Conference on Neural Networks*, pages 296–301, 2009.

[5] C. H. Chue and T. J. C. Liu. Magnetoelectroelastic antiplane analysis of a bimaterial $BaTiO_3 - CoFe_2O_4$ composite wedge with an interface crack. *Theoretical and Applied Fracture Mechanics*, 44:275–296, 2005.

[6] L. Comino, G. Rus, and R. Gallego. Combining topological sensitivity and genetic algorithms for identification of inverse problems in anisotropic materials. *Computational Mechanics*, 41:231–242, 2008.

[7] C. F. Gao, H. Kessler, and H. Balke. Crack problems in magnetoelectroelastic solids. Part I: exact solution of a crack. *International Journal of Engineering Science*, 41:969–981, 2003.

[8] C. F. Gao, P. Tong, and T. Y. Zhang. Fracture mechanics for a mode III crack in a magnetoelectroelastic solid. *International Journal of Solids and Structures*, 41:6613–6629, 2004.

[9] F. García-Sánchez, R. Rojas-Díaz, A. Sáez, and C. Zhang. Fracture of magnetoelectroelastic composite materials using boundary element method (BEM). *Theoretical and Applied Fracture Mechanics*, 47(3):192–204, 2007.

[10] M. T. Hagan, H. B. Demuth, and M. Beale. *Neural Networks Design*. PWS Publishing Company, Boston, MA, USA, 1996.

[11] S. Haykin. *Neural Networks: A Comprehensive Foundation*. Prentice Hall, Upper Saddle River, NJ, USA, 2nd edition, 1999.

[12] A. S. Islam and K. S. Craig. Damage detection in composite structures using piezoelectric materials. *Smart Materials and Structures*, 3:318–328, 1994.

[13] X. Jiang and E. Pan. Exact solution for 2D polygonal inclusion problem in anisotropic magnetoelectroelastic full-, half-, and bimaterial-planes. *International Journal of Solids and Structures*, 41:4361–4382, 2004.

[14] S. Kubo, T. Sakagami, T. Suzuki, T. Maeda, and K. Nakatani. Use of the piezoelectric film for the determination of cracks and defects - The passive and active electric potential CT method. *Journal of Physics: Conference Series*, 135, 2008. art. no. 012057.

[15] Y. J. Liu, S. Mukherjee, N. Nishimura, M. Schanz, W. Ye, A. Sutradhar, E. Pan, N. A. Dumont, A. Frangi, and A. Saez. Recent advances and emerging applications of the boundary element method. *Applied Mechanics Reviews*, 64(3):art. no. 031001, 2011.

[16] Y. Lu, L. Ye, Z. Su, L. Zhou, and L. Cheng. Artificial neural network (ANN)-based crack identification in aluminium plates with Lamb wave signals. *Journal of Intelligent Material Systems and Structures*, 20:39–49, 2009.

[17] R. Palma, G. Rus, and R. Gallego. Probabilistic inverse problem and system uncertainties for damage detection in piezoelectrics. *Mechanics of Materials*, 41(9):1000–1016, 2009.

[18] E. Pan. Exact solution for simply supported and multilayered magneto-electroelastic plates. *Journal of Applied Mechanics*, ASME 68:608–618, 2001.

[19] L. Prechelt. Automatic early stopping using cross validation: Quantifying the criteria. *Neural Networks*, 11(4):761–767, 1998.

[20] A. G. Ramm. *Inverse Problem: Mathematical and Analytical Techniques with Applications to Engineering*. Springer, New York, USA, 2005.

[21] R. Rojas-Díaz, N. Sukumar, A. Sáez, and F. García-Sánchez. Fracture in magnetoelectroelastic materials using the extended finite element method. *International Journal for Numerical Methods in Engineering*, 88:1238–1259, 2011.

[22] G. Rus, R. Palma, and J. L. Pérez-Aparicio. Optimal measurement setup for damage detection in piezoelectric plates. *International Journal of Engineering Science*, 47:554–572, 2009.

[23] A. Sáez, R. Gallego, and J. Domínguez. Hypersingular quarter-point boundary elements for crack problems. *International Journal for Numerical Methods in Engineering*, 38:1681–1701, 1995.

[24] A. K. Soh and J. X. Liu. On the constitutive equations of magnetoelectroelastic solids. *Journal of Intelligent Material Systems and Structures*, 16:597–602, 2005.

[25] Z. Su and L. Ye. *Identification of Damage using Lamb waves*. Springer, London, UK, 2009.

[26] A. Tarantola. *Inverse Problem Theory and Methods for Model Parameter Estimation*. Society for Industrial and Applied Mathematics, Philadelphia, PA, USA, 2nd edition, 2004.

[27] Z. Waszczyszyn and L. Ziemiański. Neural networks in mechanics of structures and materials - New results and prospects of applications. *Computers and Structures*, 79(22-25):2261–2276, 2001.

[28] T. L. Wu and J. H. Huang. Closed-form solutions for the magnetoelectric coupling coefficients in fibrous composites with piezoelectric and piezomagnetic phases. *International Journal of Solids and Structures*, 37(21):2981–3009, 2000.

[29] Y. G. Xiu, G. R. Liu, Z. P. Wu, and X. M. Huang. Adaptive multilayer perceptron networks for detection of cracks in anisotropic laminated plates. *Internation Journal of Solids and Structures*, 38:5625–5645, 2001.

[30] Z.-Q. Zhao. A novel modular neural network for imbalanced classification problems. *Pattern Recognition Letters*, 30:783–788, 2009.

[31] X. C. Zhong and X. F. Li. Magnetoelectroelastic analysis for an opening crack in a piezoelectromagnetic solid. *European Journal of Mechanics*, 26:405–417, 2007.

## Paper B: Crack identification in magnetoelectroelastic materials using neural networks, self-organizing algorithms and boundary element method

The original version of this paper can be found in **www.elsevier.com**

- DOI: 10.1016/j.compstruc.2013.05.005
- Journal Name: Computers & Structures
- ISSN: 0045-7949
- ISI 2011: Q1 (10/118) Impact factor: 1.874
- SCIMAGO 2011: Q1 (7/68) SJR: 1.265

# Crack identification in magnetoelectroelastic materials using neural networks, self-organizing algorithms and boundary element method

Authors: Gabriel Hattori and Andrés Sáez

ABSTRACT

In this paper, a hybrid approach that combines both supervised (neural networks) and unsupervised (self-organizing algorithms) techniques is developed for damage identification in magnetoelectroelastic (MEE) materials containing cracks. A hypersingular boundary element (BEM) formulation is used to obtain the solution to the direct problem (elastic displacements, electric and magnetic potentials) and create the corresponding training sets. Furthermore, the noise sensitivity of the resulting approach is analyzed. Results show that the proposed tool can be successfully applied to identify the location, orientation and length of different crack configurations.

**Keywords**: Damage identification; Inverse problems; Smart materials; Neural networks; Self-organizing algorithms

## B.1 Introduction

Smart materials have attracted special attention in the last few years due to their ample range of applications, as sensors and / or actuators to monitor and control the structural response. In particular, this is the case of magnetoelectroelastic (MEE) composites that exhibit coupling properties among different fields: mechanical, electric and magnetic. Due to their brittleness, damage is susceptible to appear in MEE components when in service or even during the manufacture process. This fact has motivated many authors to analyze the fracture behavior of MEE materials since the beginning of their engineering applications, by means of both analytical [3, 7, 11, 12, 20, 47] or numerical approaches [5, 14, 32, 36, 49], to cite a few references. However, little attention has been paid to the inverse damage identification problems in such smart materials.

Damage identification is one of the branches of inverse problems [44], and it is an extensively covered topic (see for example [19, 21, 41]) for materials with no electric / magnetic coupling properties. Artificial intelligent (AI) techniques are popular to model damage identification problems due to their generality and ample range of application. AI techniques have the advantage of considering the solution of the direct problem, i.e., the effect of the damage in the response, to later solve the inverse damage

identification problem. Although many authors have applied AI techniques to damage identification, the references are quite limited when it comes to smart materials: in [33], genetic algorithms and the finite element method were used to identify holes in piezoelectric ceramics, while in [28] probabilistic theory was applied for damage identification in piezoelectrics. An analytical approach, also for piezoelectric materials, may be found in [37]. The authors [17] have analyzed the use of neural networks (NN) for the crack identification of MEE materials. This preliminary work revealed that standard NN were not sufficiently robust to identify every crack pattern. Hence, a training set division (TSD) was further introduced, which assumed that some information of the problem was needed beforehand in order to define an adequate TSD. Nevertheless, such information may not be accessible in most of the damage identification problems, so that some non-user based division is clearly desirable.

The objective of the present study is to analyze the application of NN to damage identification of MEE materials combined with self-organizing algorithms. For this purpose, the dual boundary element (BEM) formulation previously developed in reference [13] for 2D static fracture analysis of MEE materials is used to solve the direct problem, thus obtaining the training sets. Training sets consist of the MEE field variables at the boundaries for different sizes, positions and crack orientations. The crack patterns that define the global training set are then further separated into several training groups by means of self-organizing techniques. Following such TSD, a back-propagation NN [18] is responsible to perform the identification for each of the resulting groups. Two different self-organizing algorithms are proposed in this work, namely, K-means [35] and Gaussian Mixtures [8]. The performance of the trained NN is validated by several examples involving the identification of cracked configurations of non-trained inputs. The noise sensitivity of the NN is also verified, leading to an adequate tool for damage identification in MEE composites.

This paper is organized as follows. The analyzed problem and the solving strategy are outlined in Section 2. Section 3 is dedicated to summarize the MEE constitutive equations as well as the BEM formulation used to solve the direct problem and obtain the training and validation data sets. The artificial intelligence tools, NN and self-organizing algorithms, are explained in Section 4. The damage identification numerical results are presented and analyzed in Section 5. Finally, some concluding remarks are presented in Section 6.

## B.2 Inverse problems and solving strategy

The inverse analysis may be defined as the identification of a parameter set $x^* \in X$ from measured or reference data $y^* \in Y$ with a known direct mapping $\psi : X \rightarrow Y$. In practice, deterministic models do not apply since they describe reality only in an ideal-

ized sense. This occurs because it is rare to have an inverse problem that respects all of the Hadamard conditions: a solution exists, this solution is unique and it is associated to only one set of parameters. Thus, input-output relations are usually expressed as

$$y = \psi(x) + \Lambda \tag{B.1}$$

where $\Lambda$ is the error associated to the measurement of $y$.

Inverse problems may be classified in terms of the parameter set to be identified: domain, governing equations, boundary conditions, applied load, material properties, etc. Presently, the main trend when tackling inverse problems is based on optimization approaches oriented towards finding the minimum of a given objective function. Such function must be defined in terms of some selected parameters that characterize the structural response. In this paper we address the case of crack identification in MEE materials, so that parameters directly related to the crack location and geometry shall be selected to identify the damaged state, as detailed in next section.

In situations where the behavior of the physical system is too complex or not entirely known, a black box model may be chosen to represent the inverse problem. For this purpose, the neural networks (NN) have been widely used in damage identification [25, 41, 42], delamination [40], structural health monitoring [22, 23, 29], and many other applications. Fig. B.1 illustrates a black box model, where the solution (say, the measured structural response of the damaged structure to a given load) is known a priori and the parameter set (that characterizes the damage) is unknown. The black box model is obtained by successive adjusts, comparing the output parameter with some known reference data until an acceptable error is attained.

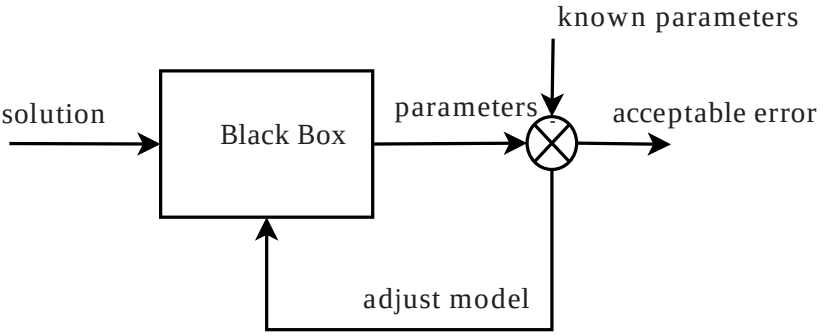


Figure B.1: Black box model scheme.

### B.2.1 Crack identification in MEE materials

Fig. B.2 illustrates a bidimensional MEE material with a crack-type damage. Let $\Omega$ be the domain, with boundary $\Gamma$, so that $\Gamma = \Gamma_{crack} \cup \Gamma_c$ with $\Gamma_{crack} = \Gamma^+_{crack} \cup \Gamma^-_{crack}$ defining

the two crack faces, and $\Gamma_c$ being the exterior non-cracked boundary. A straight crack $\Gamma_{crack}$ is defined by four parameters: the crack center $(x_c, y_c)$, the crack length $L$ and the crack orientation $\theta$, with respect to the $x$-axis. Let $\Gamma_p$ denote the partial boundary (accessible) where the disturbances in the field variables caused by the damage will be measured to become the input data set for the inverse problem analysis.

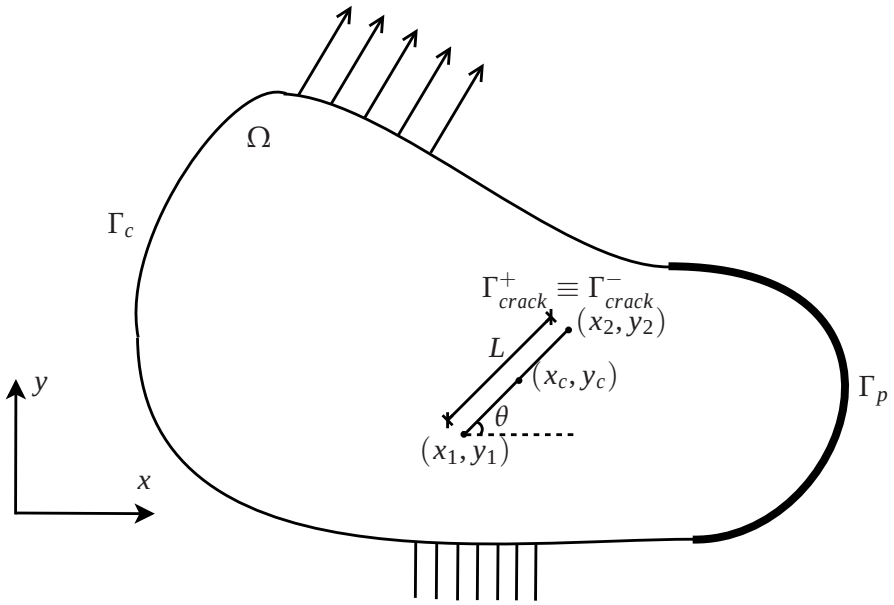


Figure B.2: Scheme of the direct problem.

The objective of this work is to provide a method to detect and quantify the damage in such MEE component using a combination of NN and self-organizing algorithms. For this purpose, the NN training and validation sets will be generated from data obtained by numerically solving a sufficiently large number of direct problems, involving an ample range of crack configurations defined by the parameters $x_c$, $y_c$, $L$ and $\theta$. The numerical data will be obtained by using the BEM formulation proposed in ref. [13], since the BEM has demonstrated its reliability and accuracy for fracture applications [24]. Subsequently, the organizing algorithms are responsible for improving the NN training through the division of the training set into several groups, resulting in the correct identification of all types of crack patterns by the NN. The overall solving strategy will be summarized next, whilst a schematic description of the BEM formulation will be given in Section 3 and details on the NN and the self-organizing techniques will be provided in Section 4.

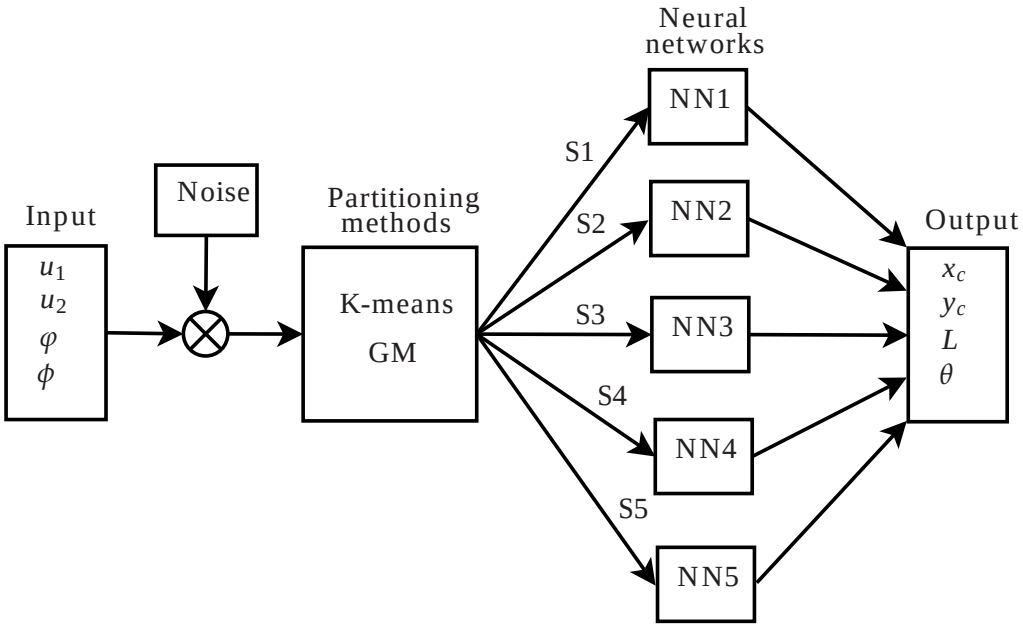


Figure B.3: Scheme of the hybrid AI method.

### B.2.2 Solving strategy

The proposed approach is a hybrid method combining both unsupervised (self-organizing algorithms) and supervised (neural networks) learning methods. The K-means and Gaussian mixtures (GM) methods are analyzed as automated classifiers, in order to overcome the limitations of the TSD approach previously proposed by the authors [17]. To the best of the authors' knowledge, this scheme has not been used before in damage identification.

It shall be remarked that the identification of crack patterns in MEE materials is an ill-conditioned problem, since very small changes in the field variables may correspond to quite different crack configurations. For this reason, noise is added to the training set to improve the NN crack identification, the addition of noise directly to the training set acts as a small extension of the training space boundaries. Thus, a training set input with noise is defined as [33]

$$u_I^{exp} = u_I^* + \varrho\zeta\sqrt{\frac{1}{N_i}\sum_{i=1}^{N_i} u_I^{*2}} \tag{B.2}$$

where $\varrho$ is the amount of noise, ranging from 0 to 0.2; $\zeta$ is a random variable with mean 0 and standard deviation 1; and $u_I^*$ is defined as

$$u_I^* = u_I - u_I^0 \tag{B.3}$$

where $u_I^{exp}$ define the set of field variables adopted as input reference data, i.e., measured at boundary $\Gamma_p$. In this work, such field variables will be selected from the elastic displacements and the electric and magnetic potentials (or any combination of them), as explained in next section. In Eq. (B.3), $u_I$ and $u_I^0$ are the field variables solution for a damaged and undamaged cases, respectively.

The NN output is the positions of the crack tips, uniquely defined by the parameters $x_c$, $y_c$, $L$ and $\theta$ (Fig. B.2). To evaluate the identification results a distance parameter is introduced as

$$dist = \frac{1}{2}\left(\sqrt{(x_{g_1} - x_1)^2 + (y_{g_1} - y_1)^2} + \sqrt{(x_{g_2} - x_2)^2 + (y_{g_2} - y_2)^2}\right) \tag{B.4}$$

where $(x_{g_1}, y_{g_1})$ and $(x_{g_2}, y_{g_2})$ are the real coordinates of the crack tips and $(x_1, y_1)$ and $(x_2, y_2)$ are the coordinates of the crack tips predicted by the NN. The NN identification performance is measured by comparing the obtained values of the *dist* parameter. Large values of this parameter mean that the identified crack is far from the actual crack tips positions, while small values indicate the identified crack is close to the actual one.

Therefore, the proposed solving strategy for the analyzed problem may be summarized as follows (see Fig. B.3)

1. Solve the direct problem to create the training set (response of the MEE material due to an applied load)
2. Add noise to the training set
3. Divide the training set using self-organizing algorithms
4. Assign each new training set to a NN
5. Train each NN
6. Check the performance of NN by comparing the NN output with the real crack, calculating the parameters *dist*.

## B.3 Direct problem (BEM)

### B.3.1 Governing equations

The linear MEE 2D problem can be formulated by direct extension of the purely elastic problem, in a similar way as [2] stated for piezoelectric materials. An extended displacement vector $u_I$ is defined that includes the elastic displacement components $u_i$, the electric potential $\phi$ and the magnetic potential $\varphi$ as

$$u_I = \begin{cases} u_i, & \text{I=1,2} \\ \varphi, & \text{I=4} \\ \phi, & \text{I=5} \end{cases} \tag{B.5}$$

where the lowercase subscripts vary from 1 to 2 (elastic), whereas the uppercase subscripts are extended with $I = 1,2$ (elastic), $I = 4$ (electric) and $I = 5$ (magnetic). A generalized stress tensor $\sigma_{iJ}$ may also be defined as

$$\sigma_{iJ} = \begin{cases} \sigma_{ij}, & \text{J=1,2} \\ D_i, & \text{J=4} \\ B_i, & \text{J=5} \end{cases} \tag{B.6}$$

where $\sigma_{ij}$ denotes the elastic stress tensor, $D_i$ are the electric displacements and $B_i$ are the magnetic inductions. These generalized stresses have an associated generalized traction vector $p_J$ given by

$$p_I = \begin{cases} p_i = \sigma_{ij} n_j, & \text{I=1,2} \\ D_n = D_j n_j, & \text{I=4} \\ B_n = B_j n_j, & \text{I=5,} \end{cases} \tag{B.7}$$

with $\mathbf{n} = (n_1, n_2)$ being the outward unit normal to the boundary, $p_i$ the elastic tractions, and $D_n$ and $B_n$ the normal electric displacement and normal magnetic induction, respectively.

The linear MEE constitutive equations may then be written as [38]

$$\sigma_{iJ} = C_{iJKl} u_{K,l} \tag{B.8}$$

where an extended elasticity tensor is specified as

$$C_{iJKl} = \left( \begin{array}{c:c:c} c_{ijkl} & e_{ikl} & h_{ikl} \\ \hdashline e_{lij} & -\epsilon_{il} & -\beta_{il} \\ \hdashline h_{lij} & -\beta_{il} & -\gamma_{il} \end{array} \right) \tag{B.9}$$

with $c_{ijkl}$, $\epsilon_{il}$ and $\gamma_{il}$ being the elastic stiffness, the dielectric permittivities and the magnetic permeabilities tensors; and $e_{lij}$, $h_{lij}$ and $\beta_{il}$ denoting the piezoelectric, the piezomagnetic and the electromagnetic coupling coefficients, respectively.

### B.3.2 BEM formulation for fracture

The dual boundary element method (DBEM) proposed in reference [13] has been used to solve the MEE fracture problem. The main features of this DBEM are next summarized in order to keep the paper as self-contained as possible. This approach implements both the extended displacement boundary integral equation (EDBIE) that relates the extended displacements at a point $\boldsymbol{\xi}$ of the domain $\Omega$, in the absence of body forces, to the extended displacements and tractions at the boundary $\Gamma$

$$c_{IJ}(\boldsymbol{\xi}) u_J(\boldsymbol{\xi}) + \int_\Gamma p^*_{IJ}(\boldsymbol{x}, \boldsymbol{\xi}) u_J(\boldsymbol{x}) d\Gamma(\boldsymbol{x}) = \int_\Gamma u^*_{IJ}(\boldsymbol{x}, \boldsymbol{\xi}) p_J(\boldsymbol{x}) d\Gamma(\boldsymbol{x}) \tag{B.10}$$

and the extended traction boundary integral equation (ETBIE) that follows from differentiation of the EDBIE and substitution into the constitutive law (Eqs. B.7 and B.8)

$$c_{IJ}(\boldsymbol{\xi})p_J(\boldsymbol{\xi}) + N_r \int_\Gamma s^*_{rIJ}(\boldsymbol{x},\boldsymbol{\xi})u_J(\boldsymbol{x})d\Gamma(\boldsymbol{x}) = \\ = N_r \int_\Gamma d^*_{rIJ}(\boldsymbol{x},\boldsymbol{\xi})p_J(\boldsymbol{x})d\Gamma(\boldsymbol{x}) \tag{B.11}$$

where $N_r$ is the outward unit normal to the boundary at the collocation point $\boldsymbol{\xi}$; $c_{IJ}$ is the so-called free term that results from the Cauchy Principal Value integration of the strongly singular kernels $p^*_{IJ}$ and thus depends on the geometry variation at the point $\boldsymbol{\xi}$; $u^*_{IJ}$ and $p^*_{IJ}$ are the extended displacement and traction fundamental solutions or Green's functions and $d^*_{rIJ}$ and $s^*_{rIJ}$ follow from derivation and substitution into the generalized Hooke's law of $u^*_{IJ}$ and $p^*_{IJ}$, respectively. The fundamental solutions are given in B.6 for completeness.

In order to model fracture problems, the EDBIE (B.10) may be applied onto the crack-free boundary $\Gamma_c$ and one of the crack surfaces, say $\Gamma_-$, whilst the ETBIE (B.11) is applied onto the other crack surface $\Gamma_+$ to yield a system of equations to obtain the extended displacements and tractions on the boundary $\Gamma$. Alternatively, if the cracks faces are free of mechanical tractions and electric and magnetic impermeable boundary conditions are considered on the crack faces ($\Delta p_J = p_J^+ + p_J^- = 0$), it will suffice to apply the EDBIE on $\Gamma_c$

$$c_{IJ}u_J + \int_{\Gamma_c} p^*_{IJ}u_J d\Gamma + \int_{\Gamma_+} p^*_{IJ}\Delta u_J d\Gamma = \int_{\Gamma_c} u^*_{IJ}p_J d\Gamma \tag{B.12}$$

and the ETBIE on one of the crack surfaces, say $\Gamma_+$, to obtain a complete set of equations with the unknowns being the extended displacements and tractions on $\Gamma_c$ and the extended crack opening displacements (ECOD: $\Delta u_J = u_J^+ - u_J^-$) on $\Gamma_{crack}$

$$p_J + N_r \int_{\Gamma_c} s^*_{rIJ}u_J d\Gamma + N_r \int_{\Gamma_+} s^*_{rIJ}\Delta u_J d\Gamma = N_r \int_{\Gamma_c} d^*_{rIJ}p_J d\Gamma \tag{B.13}$$

where the free term has been set to 1 because of the additional singularity arising from the coincidence of the two crack surfaces. This is the approach considered in this paper since the ECOD are the relevant magnitudes to obtain the fracture parameters.

When dealing with the DBEM for fracture applications some key issues need to be addressed, like properly modeling the singular behavior of the field variables around the crack tip, defining the meshing strategy together with an accurate scheme for the evaluation of the fracture parameters and, of course, developing adequate integration schemes for the singular integrations arising in both the EDBIE and the ETBIE. A thorough discussion of all these issues may be found in ref. [13] with further details on the implementation and validation of this DBEM approach, that will be next used to obtain the solution to the direct fracture problem in order to define the training and validation

sets for the NN. The basic idea is to discretize the external boundary $\Gamma_c$ and the crack surface $\Gamma_+$ into $E$ elements $\Gamma_e$:

$$\Gamma = \sum_{e=1}^{E} \Gamma_e \tag{B.14}$$

and approximate within each element the boundary variables and the ECOD by interpolation polynomial functions in terms of their modal values. For instance, the extended displacements are approximated as

$$u_I(\mathbf{x}) = \sum_{e=1}^{E} \sum_{\alpha=1}^{R} \Psi_\alpha^e(\mathbf{x}) u_I^{e\alpha} \tag{B.15}$$

where $\Psi_\alpha^e(\mathbf{x})$ are the spatial shape functions, $R$ is the number of nodes of each element and $u_I^{e\alpha}$ denote the values of the extended displacement at node $\alpha$ of the element $e$. As in reference [13], quadratic shape functions are adopted for the spatial discretization away from the crack tips, whilst quarter-point elements are placed adjacent to the crack tips in order to capture the local behavior of the ECOD properly.

This discretization leads to a linear system of algebraic equations to compute the field variables at the boundary nodes, once the boundary conditions are taken into account. Once this boundary value problem is solved, Eqs. (B.10) and (B.11) permit to compute the extended displacements and tractions at any internal point.

## B.4 Neural networks and self-organizing algorithms

The inverse crack identification problem will be addressed by developing an AI tool that combines both back-propagation NN (supervised learning technique) and self-organizing algorithms (unsupervised learning techniques). To better illustrate the key features of this approach, let consider a specific example that will be later used for validation purposes in Section 5. Namely, a plane square plate with side-length $L_s$ of MEE material containing a straight crack inside, as depicted in Fig. B.4. The plate is subjected to known loading conditions and the crack geometry (defined by the parameters $x_c$, $y_c$, $L$ and $\theta$) is to be determined by the AI tool based on the information (extended displacements) that is available for measure only on a part of the boundary $\Gamma_p$ (for instance the right side of the plate in Fig. B.4).

Next the basics of back-propagation NN and self-organizing algorithms will be presented and the advantages of combining both approaches analyzed.

### B.4.1 Back-propagation neural network

The back-propagation NN is one of the most widely used algorithms in inverse problems. This artificial NN is structured into several layers, where each layer is composed

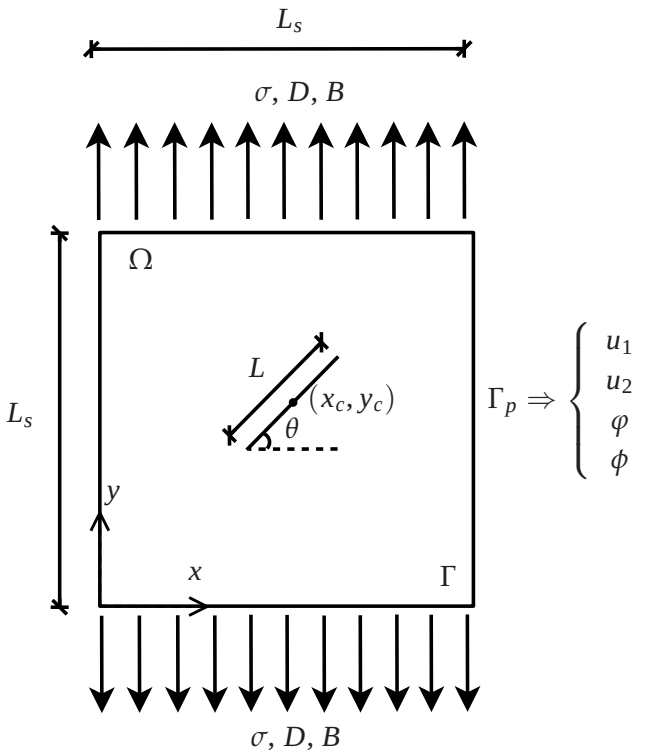


Figure B.4: Scheme of the analyzed inverse problem.

by simple structures called neurons, responsible for receiving and transmitting the information across the network. The connections formed between neurons of different layers are called weight or synapses, that take the main responsibility for the information processing inside the NN. Furthermore, the neurons have an activation function, which modifies the received input. In general, three types of layers may be identified in a NN, as shown in Fig. B.5: the input layer receives the data set, which is next processed forward by one or several hidden layers, and the output layer provide the NN response to the data set. Initially, the NN has to be trained, i.e., the NN weights are updated to learn the pattern of the training set. Then, given a specific input not used in the training process, the NN should be able to provide a reasonable output compatible to the equivalent model which originated the input/output pair. Due to this characteristic, the NN are used to easily obtain an inverse problem model when it is too complex to obtain a mathematical formulation of the inverse problem, for example. A detailled description of the back-propagation NN can be found in [18].

The usual notation to the positions of neurons (or layers) of the NN considers the neuron *i* is in the left of neuron *j*, which is in the left of neuron *k*. Fig. B.5 sketches a back-propagation NN scheme, where:

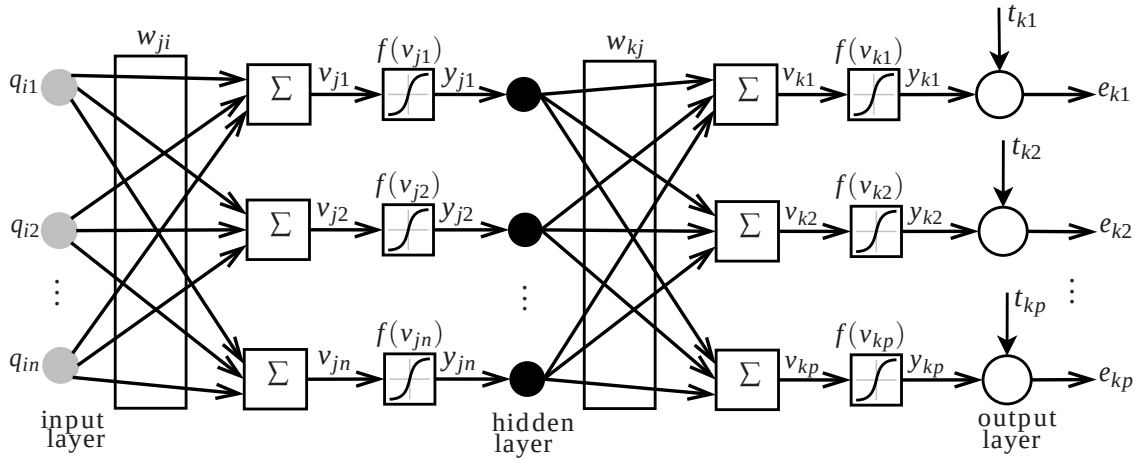


Figure B.5: Scheme of the a back-propagation NN.

- $q_{in}$: neuron input. It can be the network input or the neuron output of the previous layer, $y_{in}$;
- $w_{ji}$: neurons synaptic matrix (weight matrix). Each arrow represent one component of the $w_{ji}$ matrix of the corresponding layer. The notation $w_{ji}$ associates the output of neuron $i$ with the input of neuron $j$;
- $v_{jn}$: sum of all weights multiplied by the input;
- $f(v_{jn})$: activation function;
- $y_{kp}$: neuron output;
- $t_{kp}$: real output associated to the NN input (from the training set);
- $e_{kp}$: error associated to the neuron $k$, defined as $e_{kp} = y_{kp} - t_{kp}$.

The training set can be defined as a $N_i \times M$ matrix, where $N_i$ defines the number of neurons in the input layer and $M$ is the number of inputs composing the training set. The number of neurons in the output layer is defined by the number of parameter desired to be recognized by the NN, say $p$. In this work, the NN input is the formed by $N_i$ measures of the extended displacement $u_I$ taken on the boundary $\Gamma_p$. The NN output is defined by the crack parameters ($x_c$, $y_c$, $L$ and $\theta$), which imposes that 4 neurons have to be used in the output layer.

The NN learning is based on the minimization of the error of the output layer. The mean square error (MSE) is defined as the sum of all the quadratic errors $e_{kl}$ for all the

$p$ neurons of the output layer, for every input of the training set, and is expressed by

$$\overline{\epsilon} = \frac{1}{2M} \sum_{k=1}^{M} \sum_{l=1}^{p} e_{kl}^2 \tag{B.16}$$

The error can be calculated only for the most external layer, therefore a rule that updates all the weights for all layers has to be implemented. One of the available learning rules is the Levenberg-Marquardt algorithm [15] which has been adopted in this work. It consists in using the Jacobian to update the NN weights based on the error of the output layer. The weight update is given by

$$\Delta \mathbf{W} = -(\mathbf{J}^T \mathbf{J} + \delta \mathbf{I}) \mathbf{J}^T \mathbf{e}_k \tag{B.17}$$

where $\mathbf{J}$ is the NN Jacobian, $\delta$ is a parameter to prevent the matrix $\mathbf{J}^T\mathbf{J}$ from being singular and $\mathbf{e}_k = [e_{k1}\ e_{k2}\ \cdots\ e_{kp}]^T$. The $(h, l)$ element of the Jacobian is defined as

$$J_{hl} = \frac{\partial e_h}{\partial w_l} = \frac{\partial e_{kp}}{\partial w_{kj}} \tag{B.18}$$

where $e_h$ is the $h$-th element of the vector $\mathbf{e} = [\mathbf{e}_k^1\ \mathbf{e}_k^2\ \cdots\ \mathbf{e}_k^M]$ containing the NN output error for all the $M$ inputs, and $w_l$ is the $l$-th element of $\mathbf{w} = [w_{ji}\ w_{kj}]$ composed by all the NN weights.

Applying the chain rule on Eq. (B.18), it is shown in [15] that

$$\frac{\partial e_{kp}}{\partial w_{kj}} = \frac{\partial e_{kp}}{\partial v_{kn}} \frac{\partial v_{kn}}{\partial w_{kj}} = \dot{f}(v_{kp}) y_{jn} = S_{kp} y_{jn} \tag{B.19}$$

where $S_{kp}$ is the Marquardt sensitivity, indicating the direction the weights are updated and $\dot{f}(v_{kp})$ denotes the derivation of the activation function with respect to the argument $v_{kp}$. The above expression is valid for the output layer only, then another chain rule has to be applied to obtain the update of the hidden layers, as

$$\frac{\partial e_{kp}}{\partial w_{ji}} = \frac{\partial e_{kp}}{\partial v_{kp}} \frac{\partial v_{kp}}{\partial v_{jn}} \frac{\partial v_{jn}}{\partial w_{ji}} = S_{kp} w_{kj} \dot{f}(v_{jn}) y_{in} \tag{B.20}$$

Finally, with Eqs. (B.19) and (B.20), the Jacobian can be determined and the NN weights update in Eq. (B.17) can be calculated.

### Neural network parameters

For the crack identification problem depicted in Figs. B.2 or B.4, the NN parameters used are:

- Architecture: $N_i$ neurons in the input layer, 25 neurons in the first hidden layer, 20 neurons in the second hidden layer and 4 neurons in the output layer. In the output layer, the linear transfer function was used, for all other layers, the hyperbolic tangent sigmoid transfer function was applied [18]. $N_i$ stands for the used number of measurement positions on the boundary and the 4 output neurons correspond to the $x_c$, $y_c$, $L$ and $\theta$ parameters to be determined;
- Input: four different types of inputs were analyzed separately in this work, with $N_i$ measurements
  - the electric potential $\varphi$
  - the magnetic potential $\phi$
  - the electric and magnetic potentials taken on each measurement position
  - the elastic displacements $u_x$ and $u_y$ taken on each measurement position
- Output: the crack parameters $x_c$, $y_c$, $L$ and $\theta$;
- Training set: 1500 input / output entries;
- Validation set: 1500 input / output entries, not used in training;
- Training algorithm: Levenberg-Marquardt [15];
- Goal MSE: 0.2;
- Maximum number of iterations: 100.

Uncertainities present in inverse problems (for example, noise) need to be regularized in order to obtain a better solution. Several mathematical formulations have been developed for such purpose [16, 27, 45], and some were modified to be applied with NN [4]. In this study, a conjoint Levenberg-Marquardt and Gaussian formulation [10] has been used to smooth the update of the weights of the NN. The mean square error is then redefined as

$$\overline{\epsilon}_{reg} = \alpha\overline{\epsilon} + \beta \sum_{i,j} w_{ij}^2 = \alpha\overline{\epsilon} + \beta\overline{\epsilon}_W \tag{B.21}$$

where $\alpha$ and $\beta$ are defined as

$$\alpha = \frac{\eta}{2\overline{\epsilon}}; \quad \beta = \frac{N_p - \eta}{2\overline{\epsilon}_W} \tag{B.22}$$

where $\eta = N_p - 2\alpha tr(\overline{\epsilon}_{reg})$, $\eta$ is the effective number of parameters and $N_p$ is the total number of parameters in the NN. The parameter $\eta$ quantifies the number of parameters effectively used in the error function reduction [10].

For $\alpha \ll \beta$, the NN error will be smaller, whereas for $\beta \ll \alpha$ the weights are reduced to the detriment of a higher error, and a smoother response from the NN. A balance between $\alpha$ and $\beta$ has to be found during the training process to have a NN with an acceptable error and a sufficiently smooth response.

### B.4.2 Training set division (TSD)

In a recent work, the authors [17] have implemented NN to perform damage identification in 2D MEE materials. It was shown that the use of a single standard NN was not sufficiently robust to identify every crack pattern, as the NN failed when trying to locate small cracks, even when disconsidering the influence of noise. To overcome this limitation, a training set division (TSD) was introduced that partitioned the training set in several groups to subsequently assign each of them to an individual NN. Although the resulting TSD approach in [17] led to very good results, it still lacked of some generality since the decision on the type of division had to be user-driven, once gained some insight on the problem. For instance, for the identification problem depicted in Fig. B.4, the training set was divided in five regions: a central circular region plus four equally distributed regions, as Fig. B.6(b) illustrates. The parameter selected to uniquely define whether a particular crack (i.e., a training set entry) belonged to one of these five regions was the crack center position. Furthermore, when using the resulting AI tool to predict the crack location, the input data had to be assigned to each one of the five NN resulting from the TSD although, as expected, only one of the NN predicted the crack center position within the limits of its own training space. Hence, data manipulation is still important during the postprocessing of the identification results. Moreover, such rearrangement of the training set was only possible due to the use of some particularities of this problem,i.e, the tendency of the NN to locate small crack patterns around the same central region.

Fig. B.6 illustrates the partitioning process of 10% of the training set where each element in the graphic represents the position of a crack center.

In conclusion, although the TSD proposed in [17] showed that the learning process clearly improves when considering smaller training sets with similar patterns, it is desirable to implement an automated division technique that: (1) performs the mapping using only the data set, without requiring any prior information on the problem; and (2) permits to determine beforehand which NN should recognize a specific input pattern. This later condition may be fulfilled if the mapping is based just on intrinsic properties of the training set. For this purpose, the TSD will be next performed by means of self-organizing algorithms. Two different algorithms are considered in the present work and their performance is analyzed and evaluated next, namely K-means [35] and Gaussian Mixtures [8].

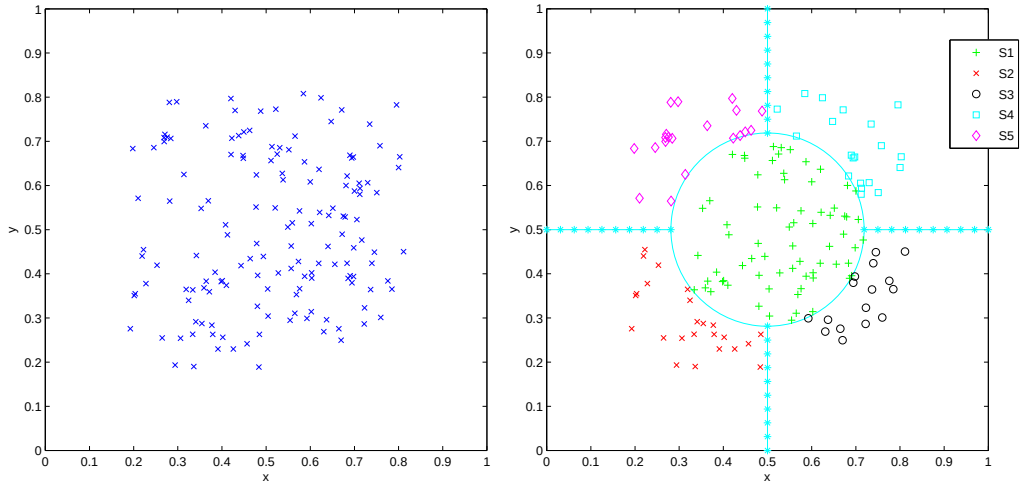


(a) Before partitioning (b) After partitioning

Figure B.6: Sample of the training set partitioning: square plate with sides normalized to 1.

### B.4.3 Self-organizing algorithms

These techniques require no error minimization with some known reference solution, depending uniquely on the given data set. For this reason, it is said that self-organizing algorithms are unsupervised methods. The main idea of the technique is to form groups with elements which have similar properties. The only parameter that has to be specified in the method is the desired number of groups to be created.

Some authors have employed self-organizing techniques in damage identification. In [30], the K-means algorithm has been used with the acoustic emission to identify the center-hole of 2D carbon / carbon faillure mechanisms during tensile tensile loading. In [26], the experimental data was processed by a covariance driven stochastic subspace identification algorithm, in order to increase the stability, so a hierarchical clustering algorithm was applied to recognize the first twelve vibration modes of a real bridge. Clustering was used to separate the measured data into two types of damage in composite materials in [48]. A revision of the most common algorithms may be found in more detail in [43].

In this study, the self-organizing methods will be used to separate the training set into five groups, as Fig. B.3 illustrates. As pointed before, the division of the training set enhances the quality of crack identification with the TSD, by allocating crack patterns with similar characteristics into smaller training sets.

For our purposes, the Principal Component Analysis (PCA) will be used as well, in order to facilitate the partitioning. PCA is a well known method for dimension re-

duction without losing information from the data [1]. In this work, each input of the training set, with dimension $N_i \times 1$, is reduced to a bidimensional vector.

The two algorithms used in this paper are briefly described next.

### K-means

K-means is a method based on punctual observation of the database. The only information given to the algorithm is the $N_g$ groups that have to be formed. Each group has a centroid, which has the property of presenting the minimum sum of the distances to all elements of a given group. A rigorous mathematical deduction of the algorithm convergence can be found in [35].

The K-means can be defined through the minimization of a functional cost

$$\min f(\mathbf{K}, \mathbf{Q}) = \sum_{l=1}^{N_g} \sum_{i=1}^{M} \kappa_{il} d(K_l, q_i) \tag{B.23}$$

$$\text{subject to} \quad \sum_{l=1}^{N_g} \kappa_{il} = 1 \tag{B.24}$$

$$\kappa_{il} = 0 \text{ or } 1$$

where $\mathbf{K} = [K_1 \cdots K_l \cdots K_{N_g}]$, $K_l$ is the position of the $l$-th centroid, $\mathbf{q}_i$ is the $i$-th input (with dimension $N_i \times 1$) of the training set matrix $\mathbf{Q} = [\mathbf{q}_1 \ q_2 \cdots \ \mathbf{q}_M]$, $\kappa_{il}$ is a partition matrix element, which assumes value 1 if the $i$-th element belongs to the $l$-th group, and 0 if not, $d(\cdot)$ is the Euclidean distance between $K_l$ and $q_i$.

The partition matrix is responsible for assigning each input $\mathbf{q}_i$ to a group. Each group is determined by its centroid, which represents the average Euclidian distance of the group members. When an element changes of group, the mean distance of each affected group is also modified, thus leading to an update of each group centroid position. For every update, elements may come close to other centroids than the actual one, leading to a new group interchange. In the K-means algorithm, the changes between groups are performed until some convergence is achieved, and the variation of elements between the groups have come to a minimum.

Fig. B.7 illustrates the generated mapping of the training set using the K-means algorithm, where each element represent a crack pattern. The electric potential $\varphi$ was used for the PCA decomposition and the number of training entries assigned to each of the five sets S1, S2, S3, S4 and S5 is indicated in the Figure.

The algorithm of the K-means used in this work can be summarized as

1. A mapping is created using the PCA in the training set;

2. $K_g$ centroids are selectioned in the created mapping and assigned to $K_g$ distincts groups. The means of each group are calculated, assuming as parameter the Euclidian distance between the elements;

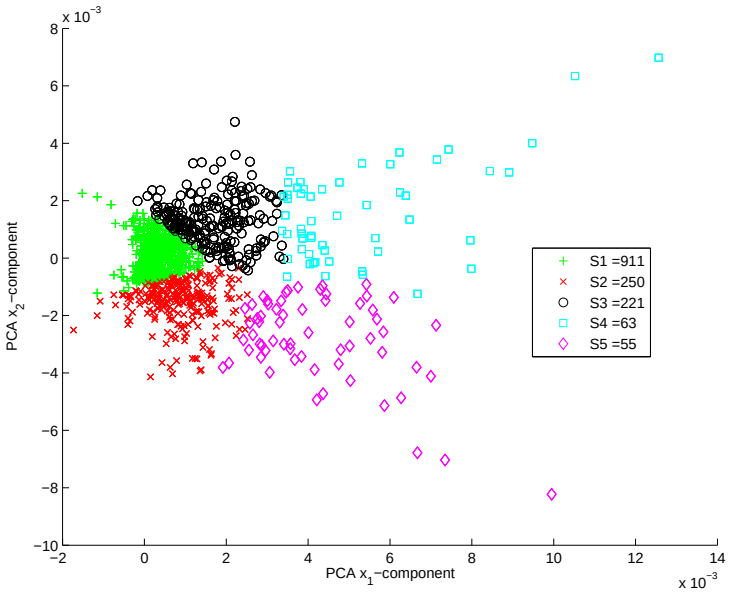


Figure B.7: Training set mapping. K-means. Input: electric potential $\varphi$.

3. The distance of the elements is measured with respect to the actual centroid. Each element is assigned to the closest centroid;

4. The elements are relocated to the group with similar properties (mean). For each new (or lost) element, the centroid position is also updated;

5. Step 4 is repeated until some sort of equilibrium is attained, for example, small variation (say $< 10\%$) of elements between the groups.

### Gaussian Mixtures (GM)

This type of approach attempts to find the most probable division of data, i.e., to establish the elements that have a probability of belonging to a particular group. The mixture is the set of $N_g$ distributions, representing $N_g$ clusters. The method searches for probabilistic attributes of each distribution as the mean and standard variation, and thus calculates the probabilities for each component of the group.

However, it is not known the prior distribution that the components of the groups should have. Thus, an iterative algorithm is used to determine the $N_g$ distributions. The algorithm used is the *Expectation Maximization* (EM), an efficient iterative procedure to obtain the Maximum Likelihood Estimate (MLE) when some data parameters are unknown. The algorithm consists of two steps, an Estimation step (E-step), where the unknown data is estimated given the observed data and the current state of the

model parameters. Then a maximization step (M-step) is executed, where the likelihood function is maximized under the assumption that the previously unknown data has been determined. A detailed deduction of the method can be found in [8].

A GM model is defined by a weighted sum of $N_g$ Gaussian densities as [31]

$$f(\mathbf{q}|\lambda) = \sum_{i=1}^{N_g} \alpha_i g(\mathbf{q}|\boldsymbol{\mu}_i, \boldsymbol{\Sigma}_i) \tag{B.25}$$

$$\sum_{i=1}^{N_g} \alpha_i = 1 \tag{B.26}$$

where $\mathbf{q}$ is a $N$-dimensional continuous valued data vector, $\lambda$ are the model parameters, $\alpha_i, i = 1 \cdots N_g$ are the mixture weights and $g(\mathbf{q}|\boldsymbol{\mu}_i, \boldsymbol{\Sigma}_i), i = 1 \cdots N_g$ are the component Gaussian densities and are defined as

$$g(\mathbf{q}|\boldsymbol{\mu}_i, \boldsymbol{\Sigma}_i) = \frac{1}{\sqrt{((2\pi)^N |\Sigma_i|)}} exp\left(-\frac{1}{2}(\mathbf{q} - \boldsymbol{\mu}_i)^T \Sigma_i^{-1} (\mathbf{q} - \boldsymbol{\mu}_i)\right) \tag{B.27}$$

where $\boldsymbol{\mu}_i$ is the mean vector and $\boldsymbol{\Sigma}_i$ is the covariance matrix. These two parameters plus the mixture weights compose the GM model and can be collectively represented as $\lambda = \{\alpha_i, \boldsymbol{\mu}_i, \boldsymbol{\Sigma}_i\}$.

Given the training set matrix $\mathbf{Q}$ with $M$ columns, the EM is used to find the best fit of the parameters $\lambda$ with the training set. The GM likelihood can be stated as

$$log\ f(\mathbf{Q}|\lambda) = \prod_{m=1}^{M} log\ f(\mathbf{q}_m|\lambda) \tag{B.28}$$

Starting from an initial model $\lambda^n$, a new model $\lambda^{n+1}$ is estimated (E-step) such that

$$log\ f(\mathbf{Q}|\lambda^{n+1}) \geq log\ f(\mathbf{Q}|\lambda^n) \tag{B.29}$$

Next, in the M-step, $\lambda^{n+1}$ is updated, corresponding to the reestimation of $\alpha_i$, $\boldsymbol{\mu}_i$ and $\boldsymbol{\Sigma}_i$ as

$$\alpha_i^{n+1} = \frac{1}{M} \sum_{m=1}^{M} Pr(i|\mathbf{q}_m, \lambda) \tag{B.30}$$

$$\mu_i^{n+1} = \frac{\sum_{m=1}^{M} Pr(i|\mathbf{q}_m, \lambda) q_m}{\sum_{m=1}^{M} Pr(i|\mathbf{q}_m, \lambda)} \tag{B.31}$$

$$\Sigma_i^{n+1} = \frac{\sum_{m=1}^{M} Pr(i|\mathbf{q}_m, \lambda) q_m^2}{Pr(i|\mathbf{q}_m, \lambda)} - \mu_i^{n+1} \tag{B.32}$$

and the *a posteriori* probability for component $i$ is expressed by

$$Pr(i|\mathbf{q}_m, \lambda) = \frac{\alpha_i g(\mathbf{q}_m|\boldsymbol{\mu}_i, \boldsymbol{\Sigma}_i)}{\sum_{k=1}^{N_g} \alpha_k g(\mathbf{q}_m|\boldsymbol{\mu}_k, \boldsymbol{\Sigma}_k)} \tag{B.33}$$

where $\mu_i$ and $\Sigma_i$ are arbitrary elements of $\boldsymbol{\mu}_i$ and $\boldsymbol{\Sigma}_i$, respectively.

Fig. B.8 shows the training set division using the PCA and GM. Again, the electric potential $\varphi$ was used for the PCA dimension reduction. One can observe that in the GM partitioning the S2 set is delimitated by the S1 set. This is consistent with the probabilistic particularity of the GM.

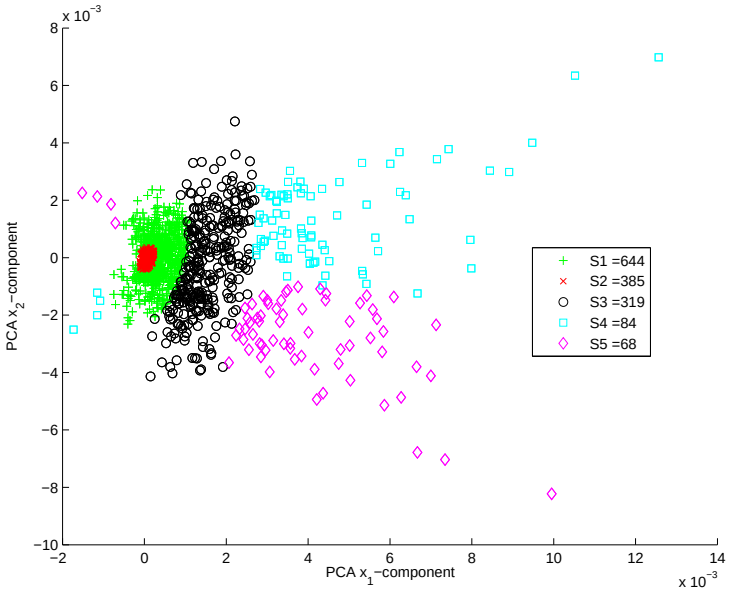


Figure B.8: Training set mapping. Gaussian Mixtures.Input: electric potential $\varphi$.

The Gaussian mixtures method can be summarized as

1. A mapping is created using the PCA in the training set;
2. Initial estimation of the distribution parameters (properties of the formed groups);
3. Calculation of the probability that a given element belongs to a given group;
4. Re-estimation of the distribution parameters;
5. Repeat steps 3 and 4 until the algorithm converges. The maximum value of Eq. (B.28) was used as stopping criteria. The final parameter to be obtained is the maximum likelihood of the distributions for the data of the mixture.

From Figs. B.7 and B.8, one can observe that both the K-means and GM methods do not necessarily lead to a uniform distribution of the elements of the training set. Some groups may have significantly more elements than the others since more crack patterns may be similar depending of the applied partitioning method. However, the groups are formed to have the smoother possible distribution, resulting in easier patterns for

the NN to learn. The NN identification results are also conditioned by the number of divisions imposed to the self-organizing methods, as it will be shown in the next section.

## B.5 Implementation and validation results

To validate the proposed identification method, a bidimensional square plate was used (Fig. B.4), where each side has $L_s = 8$ cm, of a MEE composite with equal fractions ($V_f = 0.5$) of piezoelectric ($BaTiO_3$) and piezomagnetic ($CoFe_2O_4$) phases. A unitary uniformly distributed mechanic load was applied on the top and bottom of the MEE plate. The properties of each composite component are explicited in Table B.1 [39] using the Voigt notation [46], as well as the resulting electromagnetic behavior of the MEE material. The crack parameters range considered is found in Table B.2. The crack center position and the crack length have been normalized with respect to $L_s$ and the orientation angle $\theta$ has been normalized dividing its value in degrees by 180.

Table B.1: Magnetoelectroelastic material properties.

| Properties | $BaTiO_3$ | $CoFe_2O_4$ | $V_f = 0.5$ |
|---|---|---|---|
| $C_{11}(GPa)$ | 166 | 286 | 226 |
| $C_{12}(GPa)$ | 78 | 170 | 125 |
| $C_{22}(GPa)$ | 162 | 269.5 | 216 |
| $C_{66}(GPa)$ | 43 | 45.3 | 44 |
| $e_{16}(C/m^2)$ | 11.6 | 0 | 5.8 |
| $e_{21}(C/m^2)$ | -4.4 | 0 | $-2.2$ |
| $e_{22}(C/m^2)$ | 18.6 | 0 | 9.3 |
| $\epsilon_{11}(\times 10^{-10} C^2/Nm^2)$ | 112 | 0.8 | 56.4 |
| $\epsilon_{12}(\times 10^{-10} C^2/Nm^2)$ | 126 | 0.93 | 63.5 |
| $h_{16}(N/Am)$ | 0 | 550 | 275 |
| $h_{21}(N/Am)$ | 0 | 580.3 | 290.2 |
| $h_{22}(N/Am)$ | 0 | 699.7 | 350 |
| $\gamma_{11}(\times 10^{-6} Ns^2/C^2)$ | 5 | 590 | 297 |
| $\gamma_{12}(\times 10^{-6} Ns^2/C^2)$ | 10 | 157 | 350 |
| $\beta_{11}(\times 10^{-12} Ns/VC)$ | – | – | 5.367 |
| $\beta_{12}(\times 10^{-12} Ns/VC)$ | – | – | 2737.5 |

The training set is composed by the extended displacements $u_I$ on the right side of the plate, for a large number of random combinations of the damage parameters, allowing a uniform representation of all possible crack configuration. The randomness of the NN input can be defined as:

$$C_p = C_{pr} + \varpi\zeta \tag{B.34}$$

Table B.2: Crack parameters range.

| | $\frac{x_c}{L_s}$ | $\frac{y_c}{L_s}$ | $\frac{L}{L_s}$ | $\frac{\theta}{180}$ |
|---|---|---|---|---|
| min | 0.1875 | 0.1875 | 0.0312 | 0 |
| max | 0.8125 | 0.8125 | 0.2500 | 1 |

where $C_p$ is one of the crack parameters, $C_{pr}$ is a value between the crack parameter range given in Table B.2, $\varpi$ is a ponderation number depending on the crack parameter and $\zeta$ is a random Gaussian component with mean 0 and standard deviation 1. The crack parameter range was vectorized using an interval of $0.25/L_s$ for the center crack position ($x_c$,$y_c$) parameter and the crack length $L$ parameter and an interval of $15/180$ for the crack orientation $\theta$ parameter. The $\varpi$ constant was set to $15/180$ to the $\theta$ parameter and $0.25/L_s$ for the remaining ones.

In order to solve the direct problem with the DBEM formulation described in Section 3, and thus generate the training set, each side of the external boundary was discretized with six quadratic elements. The crack boundary was discretized using ten discontinuous quadratic elements, where the crack tip elements are discontinuous quarter-point (see [34]).

Two crack configurations will be used to verify the accuracy of the different damage identification approaches. Figs. B.9(a) and B.9(b) represent the adopted reference solutions, where the x and y-axis have been normalized in terms of the plate side $L_s$.

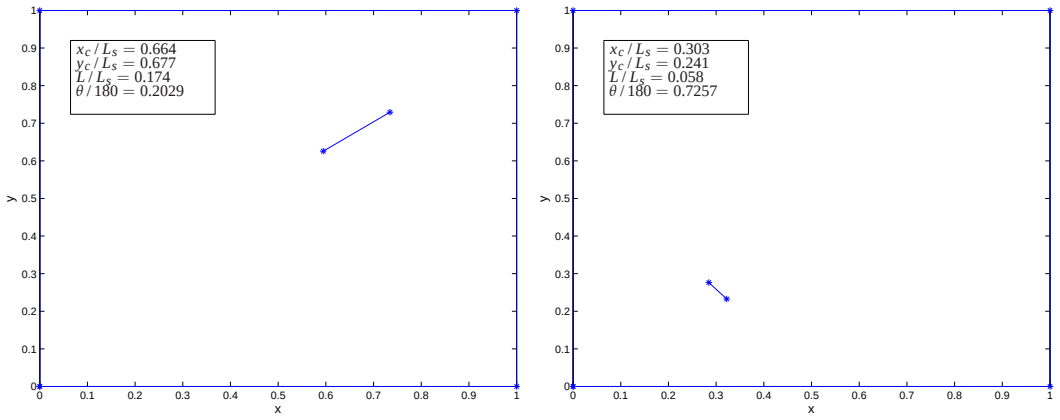


(a) Large crack (b) Small crack

Figure B.9: Reference cracks

### B.5.1 Neural network training parameters

To verify the proper training of the NN, two parameters were analyzed, namely the MSE and the number of iterations, as shown in Figs. B.10 and B.11, respectively. The objective of these graphics is to show whether the NN has achieved convergence within the limits of allowed training iterations (100 in this work). We also analyzed how the different input types led to different values of the MSE, which will indicate the better choice of the input type, presenting the lowest MSE for the training set. Four different types of input data are considered, depending on the information available for measure at $\Gamma_p$: (1) the input only consists of electric potential $\varphi$ values at $\Gamma_p$; (2) the input only consists of magnetic potential $\phi$ values at $\Gamma_p$; (3) the input consists of values of both electric and magnetic potentials at $\Gamma_p$; and (4) the input consists of values of the elastic displacements $u_x$ and $u_y$ at $\Gamma_p$. In these figures NN1, NN2, NN3, NN4 and NN5 denote the NN assigned to each of the five groups S1, S2, S3, S4 and S5, respectively, that follow from applying the TSD. The obtained results for both K-means and GM are presented for comparison purposes.

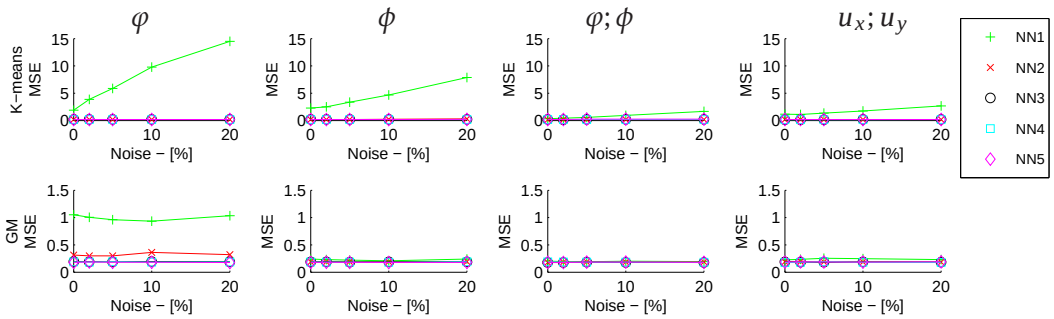


Figure B.10: NN training parameters. Mean Square Error for different combinations of input data.

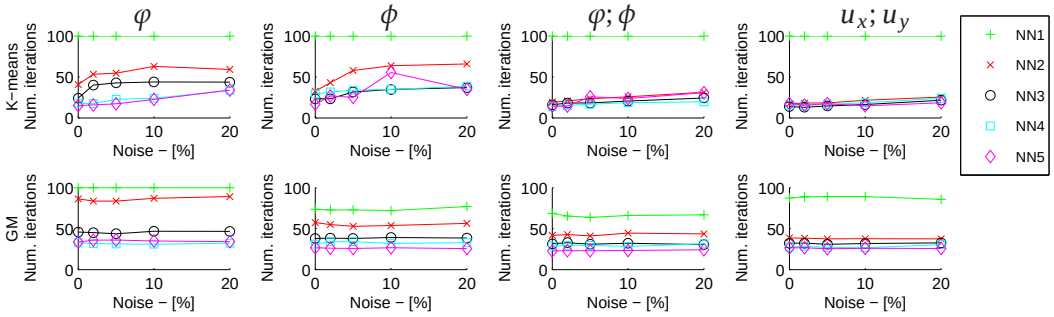


Figure B.11: NN training parameters. Number of iterations for different combinations of input data.

From Figs. B.10 and B.11, the NN achieves convergence (MSE $\leq$ 0.2 and number of iterations less or equal than 100) either when using combined inputs (electric and magnetic potential; elastic displacements) for both K-means and GM, or using the magnetic potential together with the GM algorithm. In these cases one can remark that the MSE remains basically constant with increasing noise levels. Although the NN1 of the K-means method was unable to achive convergence, it keeps low MSE levels when using combined type of inputs. No improvement in the quality of the identification was attained when increasing the number of iterations or decreasing the maximum admissible MSE value.

### B.5.2 Neural network damage identification performance

The performance of the NN with the validation set is given by the *dist* parameter, defined by Eq. (B.4). It can be visualized in Fig. B.12 for the two partitioning methods employed.

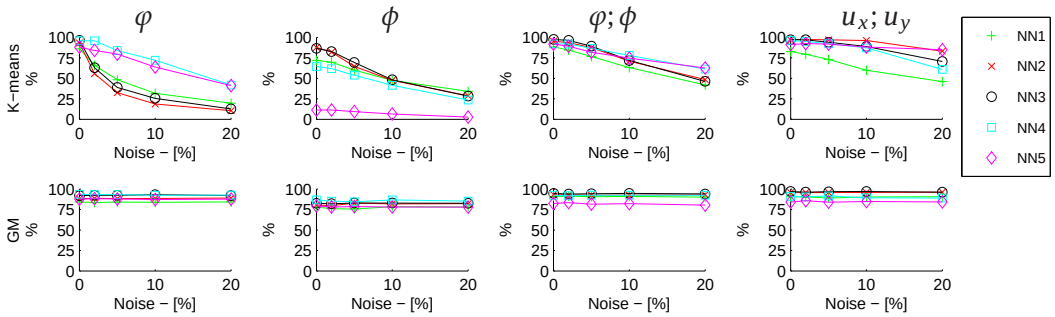


Figure B.12: NN identification performance: percentage of validation set predicting crack geometry with $dist\,/\,L_s \leq 0.1$.

A comparison between the NN output and the real cracks is shown in Fig. B.12 using the validation set. It is important to remark that the objective of the hybrid approach is to obtain the smallest values of the *dist* parameter for as many crack patterns as possible. For this matter, it was considered that an input is successfully identified if $dist\,/\,L_s \leq 0.1$. Identified cracks with values higher than this limit were disconsidered in this graphic. The results are shown in terms of percentage of the total patterns of the validation set.

For the K-means partitioning, the combined inputs lead to better identification results. The NN identification performance decreases with noise levels. High assessment accuracy is found for the noiseless cases, in contrast with poor identification performance for high noise levels. In contrast with the K-means, the NN trained with the GM algorithm present excellent results for all analyzed input types, with the elastic

displacements input leading to the best identification results. Moreover, the identification results are quite noise insensitive, a desirable characteristic in damage evaluation schemes.

Table B.3: Detailed information of number of inputs per $dist\,/\,L_s$ parameter. Input: elastic displacements $u_x; u_y$. Validation set: 1500 inputs.

| K-means | | | | | | | | | | | |
|---|---|---|---|---|---|---|---|---|---|---|---|
| | | $dist\,/\,L_s$ | | | | | | | | | |
| | | 0 | 0.04 | 0.08 | 0.12 | 0.16 | 0.20 | 0.40 | 0.60 | 0.80 | 1.00 |
| Noise | 0% | 547 | 649 | 133 | 57 | 25 | 33 | 22 | 6 | 4 | 24 |
| | 5% | 406 | 691 | 177 | 73 | 33 | 35 | 30 | 7 | 7 | 41 |
| | 20% | 335 | 686 | 251 | 89 | 48 | 56 | 21 | 5 | 3 | 6 |
| Gaussian mixtures | | | | | | | | | | | |
| Noise | 0% | 765 | 526 | 112 | 50 | 13 | 15 | 8 | 5 | 1 | 5 |
| | 5% | 779 | 516 | 105 | 38 | 17 | 23 | 15 | 5 | 1 | 1 |
| | 20% | 790 | 522 | 106 | 33 | 19 | 12 | 6 | 5 | 0 | 7 |

The *dist* parameter is detailled in Table B.3 for the elastic displacements input, since this one presents the best identification performance. One can analyze quantitatively how the *dist* parameter values are distributed in the validation set, for all used partitioning methods. For all cases, the majority of the inputs have $dist\,/\,L_s \leq 0.08$, which means the crack tip positions given by the NN are close to the real crack. It can be observed that the identification ratio decreases with the noise levels for the K-means partitioning. As pointed before, the GM NN do not present loss of precision with increasing noise.

Fig. B.13 illustrates the identification results of the reference cracks for the K-means and GM NN, with the elastic displacements as NN input and evaluating different noise levels. Excellent identification results were achieved for the large crack (Figs. B.13(a) and B.13(c)). The K-means NN did not lead to good results when identifying the small crack (Fig. B.13(b)), while the GM NN can identify smaller cracks accurately (Fig. B.13(d)), for all noise levels. Table B.4 contains the identification information for the other types of inputs for the GM networks, where both reference cracks are identified for all input types and noise levels, showing high precision for every case.

### B.5.3 Some remarks about the choice of the number of divisions with self-organizing methods

The optimal choice of how many clusters have to be formed is also an issue of study. In this sense, clustering methods are similar to the NN, where the architecture of the network is the most important feature to be determined. A specific field of study is

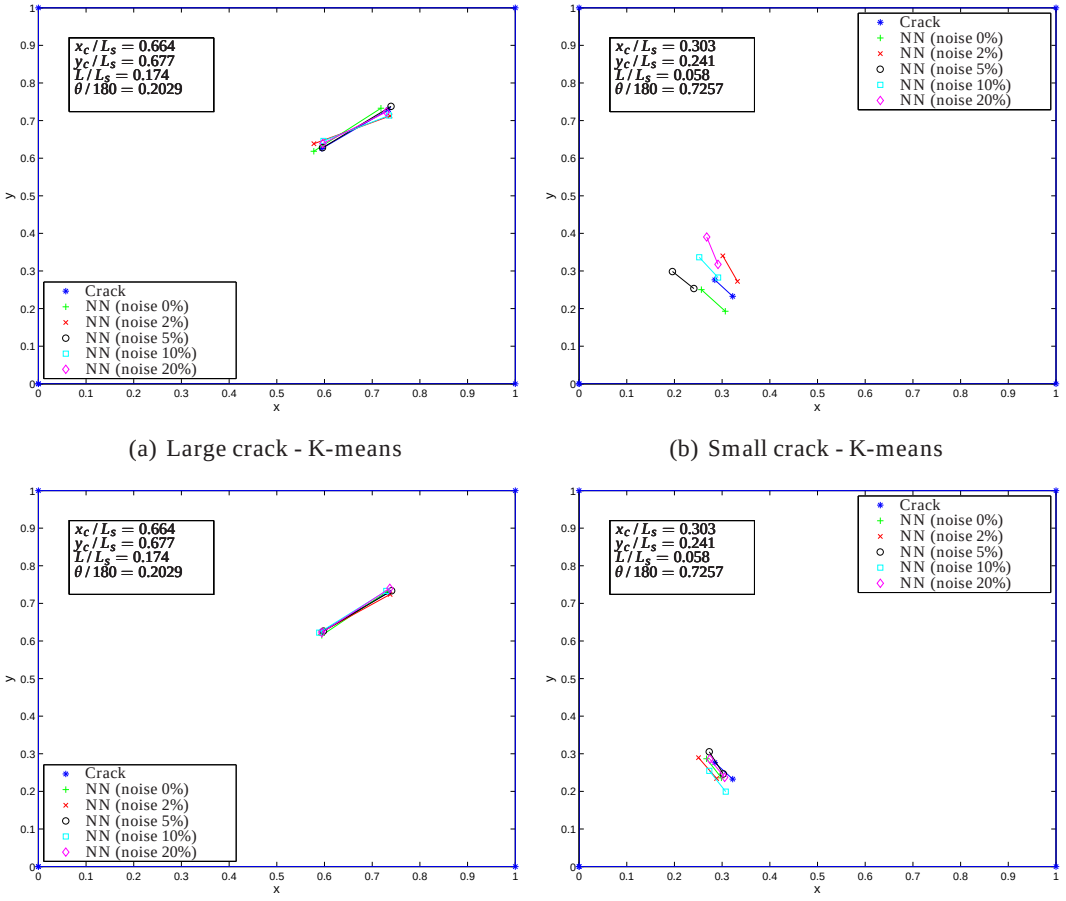


(a) Large crack - K-means

(b) Small crack - K-means

(c) Large crack - GM

(d) Small crack - GM

Figure B.13: Crack identification. Input: elastic displacements $u_x; u_y$.

dedicated to obtain methods to optimize the number of divisions for a given data set. Dunn's index [9] or the Davies-Bouldin index [6] were some of the first methods to evaluate the quality of the unsupervised methods. In this work we determined the number of division by analyzing the number of elements per group and the performance of the trained NN using the parameter *dist*.

The formation of an excessive number of groups may implicate a low ratio of elements per group, which may cause overfitting of the NN trained with these crack patterns. On the other hand, not having sufficient divisions of the training set may implicate in a suboptimal NN identification performance. Table B.5 shows the distribution of the number of identified crack patterns of the validation set using the *dist* parameter, assuming different number of formed groups. Table B.6 details the percentage of elements of the training set which belong to each group.

Table B.4: Crack identification of the reference solutions. Gaussian Mixtures.

| Large crack - Fig. B.9(a) | | | | | |
|---|---|---|---|---|---|
| Noise | Input | $\frac{x_c}{L_s}$ | $\frac{y_c}{L_s}$ | $\frac{L}{L_s}$ | $\frac{\theta}{180}$ |
| Real crack | | 0.6645 | 0.6775 | 0.1740 | 0.2029 |
| 0% | $\varphi$ | 0.6630 | 0.67498 | 0.1693 | 0.2009 |
| | $\phi$ | 0.6645 | 0.67783 | 0.1753 | 0.1999 |
| | $\varphi;\phi$ | 0.6645 | 0.67752 | 0.1740 | 0.2022 |
| | $u_x;u_y$ | 0.6645 | 0.6775 | 0.1740 | 0.2028 |
| 5% | $\varphi$ | 0.6657 | 0.6773 | 0.1806 | 0.2032 |
| | $\phi$ | 0.6648 | 0.6783 | 0.1697 | 0.2056 |
| | $\varphi;\phi$ | 0.6646 | 0.6775 | 0.1742 | 0.2035 |
| | $u_x;u_y$ | 0.6646 | 0.6774 | 0.1740 | 0.2028 |
| 20% | $\varphi$ | 0.6655 | 0.6792 | 0.1733 | 0.2097 |
| | $\phi$ | 0.6647 | 0.6774 | 0.1753 | 0.2053 |
| | $\varphi;\phi$ | 0.6646 | 0.6776 | 0.1744 | 0.2038 |
| | $u_x;u_y$ | 0.6646 | 0.6776 | 0.1740 | 0.2030 |
| Small crack - Fig. B.9(b) | | | | | |
| Real crack | | 0.3034 | 0.2415 | 0.0577 | 0.7257 |
| 0% | $\varphi$ | 0.2873 | 0.2518 | 0.0524 | 0.6902 |
| | $\phi$ | 0.3015 | 0.2052 | 0.0528 | 0.7369 |
| | $\varphi;\phi$ | 0.1879 | 0.1975 | 0.0456 | 0.6848 |
| | $u_x;u_y$ | 0.2831 | 0.2612 | 0.0599 | 0.7048 |
| 5% | $\varphi$ | 0.2915 | 0.2654 | 0.0514 | 0.7059 |
| | $\phi$ | 0.3324 | 0.2342 | 0.0691 | 0.6903 |
| | $\varphi;\phi$ | 0.2712 | 0.2557 | 0.0599 | 0.6243 |
| | $u_x;u_y$ | 0.2889 | 0.2610 | 0.0719 | 0.6658 |
| 20% | $\varphi$ | 0.3258 | 0.2770 | 0.0520 | 0.7233 |
| | $\phi$ | 0.2522 | 0.2308 | 0.0505 | 0.7153 |
| | $\varphi;\phi$ | 0.2642 | 0.2721 | 0.0452 | 0.6379 |
| | $u_x;u_y$ | 0.2822 | 0.2642 | 0.0618 | 0.6782 |

The performance of the K-means division is very similar for every number of used divisions. In this case, 3 divisions of the training set are sufficient to enable the NN to perform a good identification. The NN performance is better with 7 divisions when noise is neglected, and for high levels of noise, 5 divisions are more appropriate.

The obtained identification results using the GM algorithm shows that the NN identification results are similar with 3 and 7 divisions, and NN identification improvement is clearly noticed with 5 divisions. In this study, we can conclude that the results are optimal when considering 5 divisions.

Table B.5: Comparison between the number of divisions with self-organizing algorithms. *dist* parameter

| | | $dist / L_S$ | | | | | | | | | |
|---|---|---|---|---|---|---|---|---|---|---|---|
| | | 0 | 0.04 | 0.08 | 0.12 | 0.16 | 0.20 | 0.40 | 0.60 | 0.80 | 1.00 |
| K-means - 3 divisions | | | | | | | | | | | |
| Noise | 0% | 534 | 624 | 154 | 62 | 33 | 54 | 18 | 6 | 4 | 11 |
| | 5% | 423 | 676 | 179 | 76 | 38 | 41 | 28 | 13 | 7 | 19 |
| | 20% | 268 | 648 | 222 | 112 | 81 | 70 | 45 | 17 | 8 | 29 |
| K-means - 5 divisions | | | | | | | | | | | |
| Noise | 0% | 547 | 649 | 133 | 57 | 25 | 33 | 22 | 6 | 4 | 24 |
| | 5% | 406 | 691 | 177 | 73 | 33 | 35 | 30 | 7 | 7 | 41 |
| | 20% | 335 | 686 | 251 | 89 | 48 | 56 | 21 | 5 | 3 | 6 |
| K-means - 7 divisions | | | | | | | | | | | |
| Noise | 0% | 595 | 552 | 115 | 67 | 35 | 40 | 38 | 16 | 7 | 35 |
| | 5% | 447 | 641 | 175 | 65 | 36 | 68 | 23 | 16 | 8 | 21 |
| | 20% | 310 | 629 | 220 | 96 | 55 | 65 | 49 | 13 | 14 | 49 |
| Gaussian mixtures - 3 divisions | | | | | | | | | | | |
| Noise | 0% | 627 | 537 | 126 | 62 | 34 | 41 | 37 | 16 | 6 | 14 |
| | 5% | 550 | 513 | 158 | 72 | 46 | 61 | 49 | 16 | 12 | 23 |
| | 20% | 597 | 544 | 160 | 53 | 43 | 50 | 20 | 20 | 4 | 9 |
| Gaussian mixtures - 5 divisions | | | | | | | | | | | |
| Noise | 0% | 765 | 526 | 112 | 50 | 13 | 15 | 8 | 5 | 1 | 5 |
| | 5% | 779 | 516 | 105 | 38 | 17 | 23 | 15 | 5 | 1 | 1 |
| | 20% | 790 | 522 | 106 | 33 | 19 | 12 | 6 | 5 | 0 | 7 |
| Gaussian mixtures - 7 divisions | | | | | | | | | | | |
| Noise | 0% | 592 | 489 | 155 | 72 | 40 | 56 | 35 | 18 | 10 | 33 |
| | 5% | 521 | 521 | 175 | 98 | 40 | 57 | 35 | 15 | 13 | 25 |
| | 20% | 604 | 493 | 169 | 73 | 37 | 59 | 22 | 17 | 8 | 18 |

Table B.6: Comparison of number of divisions in percentage of the training set. K-means and GM

| | Components per group (%) | | | | | | |
|---|---|---|---|---|---|---|---|
| | 3 divisions | | | 5 divisions | | 7 divisions | |
| K-means | 75.93 | 12.87 | 11.20 | – | – | – | – |
| | 60.73 | 16.67 | 14.73 | 4.20 | 3.67 | – | – |
| | 47.47 | 23.00 | 10.53 | 8.20 | 5.73 | 3.60 | 1.47 |
| GM | 57.00 | 23.60 | 19.40 | – | – | – | – |
| | 42.87 | 25.67 | 21.60 | 5.13 | 4.73 | – | – |
| | 32.33 | 21.27 | 17.20 | 12.00 | 7.27 | 5.80 | 4.13 |

## B.6 Summary and conclusions

This work presents a new damage identification framework for MEE materials, combining supervised and unsupervised artificial intelligence techniques, to result into a hybrid approach. The direct problem was solved with a DBEM formulation, and only part of the solution on the boundary was used to assess the damage. A number of solutions of the direct problem composed the employed NN data set. In order to simulate more realistic experimental conditions, noise was introduced into the data set. The electric potential, the magnetic potential, a combined input with electric and magnetic potentials, and the elastic displacements were studied as inputs for the NN. Self-organizing algorithms were used to partition the training set, and each formed group was trained by an individual NN. A regularization scheme was used along with the training algorithm to smooth the response provided by the NN. A validation set was used to verify the generalization of the NN. It was seen that the Gaussian Mixtures self-organizing algorithm provides excellent identification results. Additionally, the input type affects the identification behavior of the networks: better results are achieved when using the elastic displacements or the combination of electric and magnetic potentials. The NN simulation may be used as a good estimation of the crack location in MEE materials.

## Acknowledgments

The authors were suported by a National Spanish Research Project from the *Ministerio de Economía y Competitividad*, reference DPI2010-21590-C02-02. G. Hattori thanks Dr. Ramón Rojas-Díaz for the fruitful discussions.

## Appendix: Static fundamental solutions for MEE materials

The fundamental solution of an infinite MEE material subject to a static point force can be expressed explicitly in terms of the Stroh's formalism. The displacement and traction at the observation point $\mathbf{x} = (x_1, x_2)$ in the J-direction due to an extended point load applied at the source point $\xi = (\xi_1, \xi_2)$ in I-direction is given by [13]

$$u^*_{IJ}(\mathbf{x}, \xi) = -\frac{1}{\pi}\Re(A_{JM}Q_{MI}ln(z^x_M - z^\xi_M)) \tag{B.35}$$

$$p^*_{IJ}(\mathbf{x}, \xi) = \frac{1}{\pi}\Re\left(B_{JM}Q_{MI}\frac{\mu_M n_1 - n_2}{z^x_M - z^\xi_M}\right) \tag{B.36}$$

where $\Re$ represent the real part and the summation rule on repeated indices applies. $z^x_M$ and $z^\xi_M$ are the observation and source points location on the complex plane and are

expressed as

$$z_M^x = x_1 + \mu_M x_2 \tag{B.37}$$

$$z_M^\xi = \xi_1 + \mu_M \xi_2 \tag{B.38}$$

where the index $M$ takes the values 1,2,4,5 and $\mu_M$ are the roots of the characterist equation of the material with positive imaginary part. These roots are obtained by solving the following eigenproblem

$$\left(\begin{array}{c|c} -\mathbf{L}^{-1}\mathbf{N} & -\mathbf{L}^{-1} \\ \hline \mathbf{Z} - \mathbf{N}^T\mathbf{L}^{-1}\mathbf{N} & -\mathbf{N}^T\mathbf{L}^{-1} \end{array}\right) \left(\begin{array}{c} \mathbf{A}_M \\ \hline \mathbf{B}_M \end{array}\right) = \mu_M \left(\begin{array}{c} \mathbf{A}_M \\ \hline \mathbf{B}_M \end{array}\right) \tag{B.39}$$

where matrices $\mathbf{A}$ and $\mathbf{B}$ are also obtained and

$$\mathbf{Z} = \mathbf{C}_{1JK1}; \mathbf{N} = \mathbf{C}_{2JK1}; \mathbf{L} = \mathbf{C}_{2JK2} \tag{B.40}$$

which are defined from the extended constitutive matrix $C_{iJKl}$ in Eq. (B.9).

Finally the matrix $\mathbf{Q}$ is calculated from

$$\mathbf{Q} = \mathbf{A}^{-1}(\mathbf{P}^{-1} + \overline{\mathbf{P}}^{-1})^{-1} \tag{B.41}$$

with $\mathbf{P} = i\mathbf{A}\mathbf{L}^{-1}$ and $\bar{\cdot}$ stands for the complex conjugate.

The kernels $s^*_{rIJ}$ and $d^*_{rIJ}$, necessary for the calculation of the boundary integral equation given in Eq. (B.11) are obtained as

$$d^*_{rIJ} = C_{rIMs} u^*_{MJ,s} \tag{B.42}$$

$$s^*_{rIJ} = C_{rIMs} p^*_{MJ,s} \tag{B.43}$$

## Bibliography


[1] H. Abdi and L. Williams. Principal component analysis. *Wiley Interdisciplinary Reviews: Computational Statistics*, 2:433–459, 2010.

[2] D. M. Barnett and J. Lothe. Dislocations and line charges in anisotropic piezoelectric insulators. *Phys. stat. sol.*, 76:105–111, 1975.

[3] Y. Benveniste. Magnetoelectric effect in fibrous composites with piezoelectric and piezomagnetic phases. *Physical Review*, B 51:16424–16427, 1995.

[4] M. Burger and A. Neubauer. Analysis of Tikhonov regularization for function approximation by neural networks. *Neural Networks*, 16:79–90, 2003.

[5] C. H. Chue and T. J. C. Liu. Magnetoelectroelastic antiplane analysis of a bimaterial $BaTiO_3 - CoFe_2O_4$ composite wedge with an interface crack. *Theoretical and Applied Fracture Mechanics*, 44:275–296, 2005.

[6] D. L. Davies and D. W. Bouldin. A cluster separation measure. *IEEE Transactions on Pattern Analysis and Machine Intelligence*, 1(2):224–227, 1979.

[7] W. F. Deeg. *The analysis of dislocation, crack and inclusion problems in piezoelectric solids*. PhD thesis, Stanford University, USA, 1980.

[8] A. P. Dempster, N. M. Laird, and D. B. Rubin. Maximum likelihood from incomplete data via the em algorithm. *Journal of the Royal Statistical Society. Series B (Methodological)*, 39(1):1–38, 1977.

[9] J. C. Dunn. Well-separated clusters and optimal fuzzy partitions. *Journal of Cybernetica*, 4(1):95–104, 1974.

[10] F. D. Foresee and M. T. Hagan. Gauss-Newton approximation to Bayesian learning. In *International Conference in Neural Networks*, volume 3, pages 1930–1935, 1997.

[11] C. F. Gao, H. Kessler, and H. Balke. Crack problems in magnetoelectroelastic solids. Part I: exact solution of a crack. *International Journal of Engineering Science*, 41:969–981, 2003.

[12] C. F. Gao, H. Kessler, and H. Balke. Crack problems in magnetoelectroelastic solids. Part II: General solution of collinear cracks. *International Journal of Engineering Science*, 41:983–994, 2003.

[13] F. García-Sánchez, R. Rojas-Díaz, A. Sáez, and C. Zhang. Fracture of magnetoelectroelastic composite materials using boundary element method (BEM). *Theoretical and Applied Fracture Mechanics*, 47(3):192–204, 2007.

[14] F. García-Sánchez, A. Sáez, and J. Domínguez. Anisotropic and piezoelectric materials fracture analysis by BEM. *Computer and Structures*, 83:804–820, 2005.

[15] M. T. Hagan, H. B. Demuth, and M. Beale. *Neural Networks Design*. PWS Publishing Company, Boston, MA, USA, 1996.

[16] M. Hanke, A. Neubauer, and O. Scherzer. A convergence analysis of the Landweber iteration for nonlinear ill-posed problems. *Numerische Mathematik*, 72:21–37, 1995.

[17] G. Hattori and A. Sáez. Damage identification in multifield materials using neural networks. *Inverse Problems in Science and Engineering*, 2013.

[18] S. Haykin. *Neural Networks: A Comprehensive Foundation*. Prentice Hall, Upper Saddle River, NJ, USA, 2nd edition, 1999.

[19] A. S. Islam and K. S. Craig. Damage detection in composite structures using piezoelectric materials. *Smart Materials and Structures*, 3:318–328, 1994.

[20] X. Jiang and E. Pan. Exact solution for 2D polygonal inclusion problem in anisotropic magnetoelectroelastic full-, half-, and bimaterial-planes. *International Journal of Solids and Structures*, 41:4361–4382, 2004.

[21] S. Kubo, T. Sakagami, T. Suzuki, T. Maeda, and K. Nakatani. Use of the piezoelectric film for the determination of cracks and defects - The passive and active electric potential CT method. *Journal of Physics: Conference Series*, 135, 2008. art. no. 012057.

[22] J. Lee and S. Kim. Structural damage detection in the frequency domain using neural networks. *Journal of Intelligent Material Systems and Structures*, 18(8):785–792, 2007.

[23] J. Lee, G. Kirikera, I. Kang, M. Schulz, and V. Shanov. Structural health monitoring using continuous sensors and neural network analysis. *Smart Materials and Structures*, 15(5):1266–1274, 2006.

[24] Y. Liu, S. Mukherjee, N. Nishimura, M. Schanz, W. Ye, A. Sutradhar, E. Pan, N. Dumont, A. Frangi, and A. Saez. Recent advances and emerging applications of the boundary element method. *Applied Mechanics Reviews*, 64(3), 2011.

[25] Y. Lu, L. Ye, Z. Su, L. Zhou, and L. Cheng. Artificial neural network (ANN)-based crack identification in aluminium plates with Lamb wave signals. *Journal of Intelligent Material Systems and Structures*, 20:39–49, 2009.

[26] F. Magalhes, A. Cunha, and E. Caetano. Online automatic identification of the modal parameters of a long span arch bridge. *Mechanical Systems and Signal Processing*, 23(2):316–329, 2009.

[27] V. Martins. Métodos level set para problemas inversos. Master's thesis, Universidade Federal de Santa Catarina - UFSC, 2005.

[28] R. Palma, G. Rus, and R. Gallego. Probabilistic inverse problem and system uncertainties for damage detection in piezoelectrics. *Mechanics of Materials*, 41(9):1000–1016, 2009.

[29] P. Pandey and S. Barai. Multilayer perceptron in damage detection of bridge structures. *Computers and Structures*, 54(4):597–608, 1995.

[30] Y. Z. Pappas, Y. P. Markopoulos, and V. Kostopoulos. Failure mechanisms analysis of 2D carbon / carbon using acoustic emission monitoring. *Applied Mechanics Reviews*, 64(3), 2011.

[31] D. A. Reynolds, T. F. Quatieri, and R. Dunn. Speaker verification using adapted gaussian mixture models. *Digital Signal Processing: A Review Journal*, 10(1):19–41, 2000.

[32] R. Rojas-Díaz, N. Sukumar, A. Sáez, and F. García-Sánchez. Fracture in magnetoelectroelastic materials using the extended finite element method. *International Journal for Numerical Methods in Engineering*, 88:1238–1259, 2011.

[33] G. Rus, R. Palma, and J. L. Pérez-Aparicio. Optimal measurement setup for damage detection in piezoelectric plates. *International Journal of Engineering Science*, 47:554–572, 2009.

[34] A. Sáez, R. Gallego, and J. Domínguez. Hypersingular quarter-point boundary elements for crack problems. *International Journal for Numerical Methods in Engineering*, 38:1681–1701, 1995.

[35] S. Z. Selim and M. A. Ismail. K-means-type algorithms: A generalized convergence theorem and characterization of local optimality. *IEEE Transactions on Pattern Analysis and Machine Intelligence*, PAMI-6(1):81–87, 1984.

[36] J. Sladek, V. Sladek, P. Solek, and E. Pan. Fracture analysis of cracks in magneto-electro-elastic solids by the MLPG. *Computational Mechanics*, 42:697–714, 2008.

[37] J. Sladek, V. Sladek, P. H. Wen, and Y. C. Hon. Inverse fracture problems in piezoelectric solids by local integral equation method. *Engineering Analysis with Boundary Elements*, 33:1089–1099, 2009.

[38] A. K. Soh and J. X. Liu. On the constitutive equations of magnetoelectroelastic solids. *Journal of Intelligent Material Systems and Structures*, 16:597–602, 2005.

[39] Z. F. Song and G. C. Sih. Crack initiation behavior in magnetoelectroelastic composite under in-plane deformation. *Theoretical and Applied Fracture Mechanics: Mechanics and Physics of Fracture*, 39:189–207, 2003.

[40] Z. Su and L. Ye. Lamb wave-based quantitative identification of delamination in CF / EP composite structures using artificial neural algorithm. *Composite Structures*, 66(1-4):627–637, 2004.

[41] Z. Su and L. Ye. *Identification of Damage using Lamb waves*. Springer, London, UK, 2009.

[42] M. W. Suh and M. B. Shim. Crack identification using hybrid neuro-genetic technique. *Journal of Sound and Vibration*, 238(4):617–635, 2000.

[43] P.-N. Tan, M. Steinbach, and V. Kumar. *Introduction to data mining*. Addison-Wesley, 2006.

[44] A. Tarantola. *Inverse Problem Theory and Methods for Model Parameter Estimation*. Society for Industrial and Applied Mathematics, Philadelphia, PA, USA, 2nd edition, 2004.

[45] A. Tikhonov and V. Arsénine. Méthodes de résolution de problmes mal posés. *MIR*, 1976.

[46] W. Voigt. *Lehrbuch der Kristallphysik*. B.G. Teubner, 1928.

[47] T. L. Wu and J. H. Huang. Closed-form solutions for the magnetoelectric coupling coefficients in fibrous composites with piezoelectric and piezomagnetic phases. *International Journal of Solids and Structures*, 37(21):2981–3009, 2000.

[48] B. L. Yang, X. M. Zhuang, T. H. Zhang, and X. Yan. Damage mode identification for the clustering analysis of AE signals in thermoplastic composites. *Journal of Nondestructive Evaluation*, 28(3-4):163–168, 2009.

[49] X. C. Zhong and X. F. Li. Magnetoelectroelastic analysis for an opening crack in a piezoelectromagnetic solid. *European Journal of Mechanics*, 26:405–417, 2007.

## Paper C: New anisotropic crack-tip enrichment functions for the extended finite element method

The original version of this paper can be found in **www.springer.com**

- DOI: 10.1007/s00466-012-0691-0
- Journal Name: Computational Mechanics
- ISSN: 0178-7675
- ISI 2011: Q1 (15/132) Impact factor: 2.065
- SCIMAGO 2011: Q1 (5/68) SJR: 1.859

# New anisotropic crack-tip enrichment functions for the extended finite element method

Authors: Gabriel Hattori, Ramón Rojas-Díaz, Andrés Sáez, Natarajan Sukumar and Felipe García-Sánchez

ABSTRACT

In this paper, the extended finite element method (X-FEM) is implemented to analyze fracture mechanics problems in elastic materials that exhibit general anisotropy. In the X-FEM, crack modeling is addressed by adding discontinuous enrichment functions to the standard FE polynomial approximation within the framework of partition of unity. In particular, the crack interior is represented by the Heaviside function, whereas the crack-tip is modeled by the so-called crack-tip enrichment functions. These functions have previously been obtained in the literature for isotropic, orthotropic, piezoelectric and magnetoelectroelastic materials. In the present work, the crack-tip functions are determined by means of the Stroh's formalism for fully anisotropic materials, thus providing a new set of enrichment functions in a concise and compact form. The proposed formulation is validated by comparing the obtained results with other analytical and numerical solutions. Convergence rates for both topological and geometrical enrichments are presented. Performance of the newly derived enrichment functions is studied, and comparisons are made to the well-known classical crack-tip functions for isotropic materials.

**Keywords**: Crack-tip enrichment functions; Anisotropic materials; X-FEM; Stroh's formalism

## C.1 Introduction

The strong demand for materials with a high strength per unit weight ratio in different branches of engineering has led to the development of different analytical and numerical techniques to solve fracture mechanics problems in anisotropic materials. Pioneering works by Muskhelishvili [15] and Sih et al. [20], or more recently, works by Nobile and Carloni [16], developed analytical techniques to solve crack problems in anisotropic and orthotropic plates. However, these methods are limited to simple geometries and load combinations. Therefore, numerical methods become essential to analyze more complicated engineering applications. In particular, models based on the boundary element method (both the classical [22] and the dual [11, 17, 23] approxima-

tions), meshless (meshless local Petrov-Galerkin [21]), and the finite element method (FEM) [7], have been developed.

All the above-mentioned numerical techniques have proven to be accurate and robust to solve crack problems. However, in the case of the FEM, its direct application is unwieldly, since the mesh must conform to the crack geometry, mesh refinement is required near the crack-tip, and for crack propagation simulations, remeshing is needed. To circumvent these difficulties, the extended finite element method (X-FEM), first presented by Belytschko and co-workers [6, 13], has emerged as a powerful alternative in computational fracture. It has been successfully applied to solve crack problems in materials with different constitutive laws: see, for example, the works by Moës et al. [13] in isotropic media, Sukumar et al. [25] in bimaterials, Asadpoure and Mohammadi [2] in orthotropic materials, Béchet et al. [5] in piezoelectric solids and Rojas-Díaz et al. [19] in magnetoelectroelastic materials. Abbas and Fries [1] have obtained enrichment functions that can be applied to brittle as well as cohesive cracks. In the X-FEM, additional (enrichment) functions are added to the classical finite element polynomial approximation through the framework of partition of unity [3]. To model the crack discontinuity, the crack interior is represented by a discontinuous (Heaviside) function, whereas the behavior around the crack-tip is modeled by the asymptotic crack-tip enrichment functions.

In this work, a new set of crack-tip enrichment functions is derived to simulate two-dimensional elastic fracture in general anisotropic media. These new functions are obtained in a concise and compact form in terms of the Stroh's formalism [24]. The resulting formulation is validated by comparison of the obtained results for several crack configurations with previous analytical and / or numerical solutions. Two different enrichment strategies have been adopted: the conventional X-FEM using a topological enrichment and a geometrical (fixed area) enrichment [4, 12]. Convergence rates for both enrichments are presented and performance of the newly derived enrichment functions is further analyzed and compared with the classical crack-tip functions for isotropic materials.

The paper is structured as follows. The governing equations are stated in Section 2. The theoretical foundations of the X-FEM are presented in Section 3, and the new crack-tip enrichment functions are derived in Section 4 and the computation of fracture parameters using the domain form of the contour interaction integral is briefly described in Section 5. Several crack problems are solved in Section 6 to validate the approach and characterize its convergence. The main conclusions from this study are summarized in Section 7.

## C.2 Governing equations

### C.2.1 Basic equations

In an anisotropic elastic domain, the static equilibrium equations in the presence of body forces **b** are given by

$$\sigma_{ij,j} + b_i = 0 \tag{C.1}$$

Both the stress and strain tensors are symmetric: $\sigma_{ij} = \sigma_{ji}$; $\varepsilon_{ij} = \varepsilon_{ji}$.

$$\varepsilon_{ij} = \frac{1}{2}(u_{i,j} + u_{j,i}) \tag{C.2}$$

The linear constitutive relations between stresses $\sigma_{ij}$ and strains $\varepsilon_{kl}$ are given by the generalized Hooke's law

$$\sigma_{ij} = C_{ijkl}\varepsilon_{kl} \tag{C.3}$$

where $C_{ijkl}$ define the material constants tensor, satisfying the following symmetry relations

$$C_{ijkl} = C_{jikl} = C_{ijlk} = C_{klij} \tag{C.4}$$

that lead to a tensor with only 21 independent components for the 3D case, and 6 components in the 2D case.

### C.2.2 Stroh's formalism

To satisfy the equilibrium equations stated in (C.1), the displacement field in a generally anisotropic plane domain may be written as [24, 27]

$$\mathbf{u} = \mathbf{a}f(z) \tag{C.5}$$

where $z = x_1 + \mu_m x_2$ is the transformation into the complex plane of the physical coordinates $(x_1, x_2)$, and $\mu_m$ represents the complex roots with positive imaginary part, of the characteristic equation of the material. Such an equation follows from derivation of (C.5), and subsequent substitution of (C.3) into the equilibrium relations (C.1), leading to

$$\{\mathbf{Z} + (\mathbf{M} + \mathbf{M}^T)\mu_m + \mathbf{L}\mu_m^2\}\mathbf{a} = \mathbf{0} \tag{C.6}$$

with

$$\mathbf{Z} := \mathbf{C}_{1ij1}; \quad \mathbf{M} := \mathbf{C}_{2ij1}; \quad \mathbf{L} := \mathbf{C}_{2ij2} \tag{C.7}$$

Equation (C.6) can be rearranged and further expressed as the following eigenvalue problem

$$\left(\begin{array}{c|c} -\mathbf{L}^{-1}\mathbf{M} & -\mathbf{L}^{-1} \\ \hline \mathbf{Z} - \mathbf{M}^T\mathbf{L}^{-1}\mathbf{M} & -\mathbf{M}^T\mathbf{L}^{-1} \end{array}\right)\left(\frac{\mathbf{A}_m}{\mathbf{B}_m}\right) = \mu_m\left(\frac{\mathbf{A}_m}{\mathbf{B}_m}\right) \quad \text{(no sum on } m\text{)} \tag{C.8}$$

Since the tensors $\mathbf{A}$ and $\mathbf{B}$ and the eigenvalues $\mu_m$ depend only on the material properties, they are independent of the geometrical position of the adopted coordinated system. These characteristics allow the calculation of precise and general terms by means of the Stroh's formalism.

### C.2.3 Asymptotic fields around the crack-tip

The asymptotic displacement field around a crack-tip in a plane anisotropic domain was first derived by Sih et al. [20]. Adopting a polar coordinate system $(r,\theta)$ with origin at the crack-tip, the displacement field can be expressed by means of the Stroh's formalism [26] as

$$u_i(r,\theta) = \sqrt{\frac{2}{\pi}}\Re\left(K_\alpha A_{im} B^{-1}_{m\alpha}\sqrt{r\left(\cos\theta + \mu_m \sin\theta\right)}\right) \tag{C.9}$$

where the summation convention over repeated indices holds; $i,m = 1,2$; $\alpha = I,\ II$ is associated with the fracture modes; and $\Re(\cdot)$ is the real part of $(\cdot)$.

Similarly, the asymptotic stress fields may be written as

$$\sigma_{ij}(r,\theta) = (-1)^j\sqrt{\frac{1}{2\pi}}\Re\left(K_\alpha B_{im} B^{-1}_{m\alpha}\frac{\delta_{j1}\mu_m + \delta_{j2}}{\sqrt{r\left(\cos\theta + \mu_m \sin\theta\right)}}\right) \tag{C.10}$$

where $\delta_{jk}$ is the Kronecker-delta.

## C.3 Extended finite element formulation

Equation (C.10) reveals that the discontinuity induced by the crack leads to a non-smooth behavior of the field variables, with resulting singular gradient that needs to be taken into account. For this purpose, the extended finite element method [6, 13] is adopted in which the classical FEM polynomial space is enriched through the framework of partition of unity [3] with the addition of special shape functions: the crack jump is represented by a discontinuous (Heaviside) function and the crack-tip $\sqrt{r}$-behavior is modeled by asymptotic crack-tip enrichment functions. In this way, the FE mesh does not need to match the crack geometry and only a subset of nodes close to the crack needs to be enriched. Currently, the X-FEM is a well-established technique and its advantages over conventional FEM for problems with non-smooth behavior are well-recognized [10].

### C.3.1 Crack modeling and selection of enriched nodes

Consider a domain $\Omega \subset \mathbf{R}^2$ with boundary $\Gamma$, which contains a crack $\Gamma_c = \Gamma_c^- \cup \Gamma_c^+$. The domain is discretized by finite elements, so that $\mathcal{N}$ denotes the nodal set. Displace-

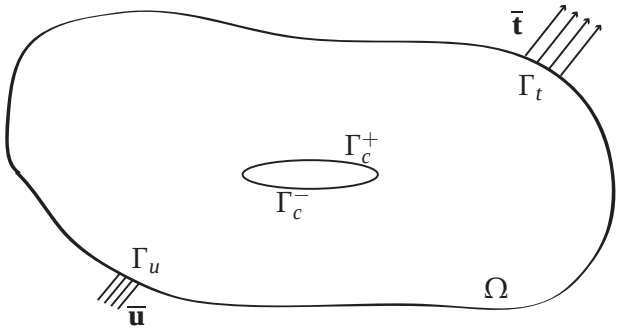


Figure C.1: Boundary-value problem with an internal crack.

ments are prescribed on $\Gamma_u$, whereas tractions are imposed on $\Gamma_t$, so that $\Gamma = \Gamma_u \cup \Gamma_t$ as illustrated in Figure C.1. The displacement approximation in the X-FEM can be written as [13]

$$\mathbf{u}^h(\mathbf{x}) = \sum_{i \in \mathcal{N}} N_i(\mathbf{x})\mathbf{u}_i + \sum_{j \in \mathcal{N}^{\mathcal{H}}} N_j(\mathbf{x})H(\mathbf{x})\mathbf{a}_j + \sum_{k \in \mathcal{N}^{\mathcal{CT}}} N_k(\mathbf{x}) \sum_{\alpha} F_\alpha(\mathbf{x})\mathbf{b}_k^\alpha \tag{C.11}$$

where $N_i$ is the standard finite element shape function associated with node $i$, $\mathbf{u}_i$ is the vector of nodal degrees of freedom for classical finite elements, and $\mathbf{a}_j$ and $\mathbf{b}_k^\alpha$ are the added set of degrees of freedom that are associated with enriched basis functions. $H(\mathbf{x})$ is the generalized Heaviside function, defined as $+1$ or $-1$, depending on whether it is evaluated above or below the crack, respectively. The Heaviside function thus enables modeling of a crack that fully cuts a finite element. Additionally, at the nodes around the crack-tip, crack-tip functions $F_\alpha(\mathbf{x})$ are included. They are described in more detail in Section C.4. In elastic materials, $\mathbf{b}_k^\alpha$ is an 8-component vector for two-dimensional problems, since only two nodal variables ($u_1$, $u_2$) and four enrichment functions are needed to describe all the possible deformation states in the vicinity of the crack-tip. This holds for both the well-known isotropic crack-tip functions [13] as well as for the orthotropic [2] and fully anisotropic cases, as will be shown next.

Figure C.2 illustrates the classical topological enrichment strategy [13] to model a crack in the X-FEM. The nodes that are enriched with the Heaviside function (set $\mathcal{N}^H$) are marked with a filled circle and they belong to elements fully cut by the crack. The nodes that are enriched with crack-tip enrichment functions (set $\mathcal{N}^{CT}$) are marked with a square and they belong to elements that contain the crack-tip.

More recently, an alternative enrichment strategy that leads to improved results was proposed by Laborde et al. [12] (geometrical enrichment): some nodes around the ones belonging to the elements that contain the crack-tips are also enriched with the crack-tip functions, in order to improve the convergence of the method. Here we adopt a fixed area enrichment, so that all nodes lying inside a circle of diameter $2r_e$ centered at

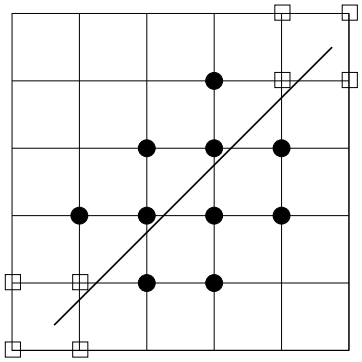

Figure C.2: Node selection for topological enrichment.

the crack-tip are enriched with the crack-tip functions, as is depicted in Figure C.3.

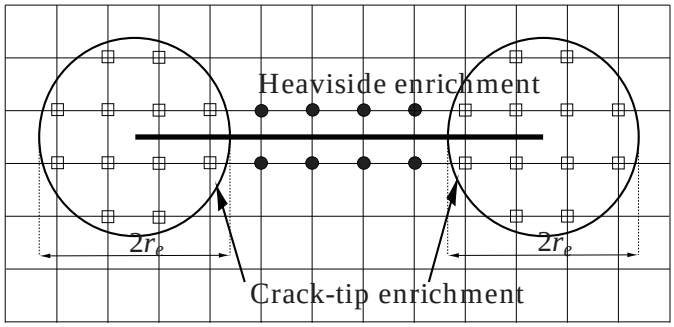


Figure C.3: Node selection for geometrical enrichment.

### C.3.2 Weak formulation and discrete equations

Let $\mathbf{u}$ be the displacement vector and $\sigma$ the stress tensor. The weak form (principle of virtual work) for a continuum elastostatic problem in a general anisotropic solid is given by

$$\int_\Omega \sigma : \delta\varepsilon \, d\Omega = \int_{\Gamma_t} \bar{\mathbf{t}} \cdot \delta\mathbf{u} \, d\Gamma + \int_\Omega \mathbf{b} \cdot \delta\mathbf{u} \, d\Omega \tag{C.12}$$

where $\delta$ is the variation operator, $\bar{\mathbf{t}}$ is the prescribed traction vector and $\mathbf{b}$ are the body forces. On substituting the trial and test approximations in the above equation, and using the arbitrariness of nodal variations, we obtain the discrete equations:

$$\mathbf{Kd} = \mathbf{f} \tag{C.13}$$

where $\mathbf{K}$ is the global stiffness matrix and $\mathbf{f}$ is the force vector.

The element contribution to $\mathbf{K}$ and $\mathbf{f}$ are as follows:

$$\mathbf{k}_{ij}^{e} = \begin{bmatrix} \mathbf{k}_{ij}^{uu} & \mathbf{k}_{ij}^{ua} & \mathbf{k}_{ij}^{ub} \\ \mathbf{k}_{ij}^{au} & \mathbf{k}_{ij}^{aa} & \mathbf{k}_{ij}^{ab} \\ \mathbf{k}_{ij}^{bu} & \mathbf{k}_{ij}^{ba} & \mathbf{k}_{ij}^{bb} \end{bmatrix} \tag{C.14a}$$

$$\mathbf{f}_{i}^{e} = \begin{Bmatrix} \mathbf{f}_{i}^{u} & \mathbf{f}_{i}^{a} & \mathbf{f}_{i}^{b\alpha} \end{Bmatrix}^{T} \quad (\alpha = 1,4) \tag{C.14b}$$

where the indices $u$, $a$, $b$ refer to the nodal displacements vector, the Heaviside enriched nodes and the crack-tip enriched nodes, respectively.

$$\mathbf{k}_{ij}^{rs} = \int_{\Omega_e} (\mathbf{B}_i^r)^T \mathbf{C} (\mathbf{B}_i^s)\, d\Omega \quad (r,s = u,a,b) \tag{C.15a}$$

$$\mathbf{f}_{i}^{u} = \int_{\partial\Omega_e} N_i \bar{\mathbf{t}} d\Gamma + \int_{\Omega_e} N_i \mathbf{b} d\Omega \tag{C.15b}$$

$$\mathbf{f}_{i}^{a} = \int_{\partial\Omega_e} N_i H \bar{\mathbf{t}} d\Gamma + \int_{\Omega_e} N_i H \mathbf{b} d\Omega \tag{C.15c}$$

$$\mathbf{f}_{i}^{b\alpha} = \int_{\partial\Omega_e} N_i F_\alpha \bar{\mathbf{t}} d\Gamma + \int_{\Omega_e} N_i F_\alpha \mathbf{b} d\Omega \quad (\alpha = 1,4) \tag{C.15d}$$

In (C.15), $\mathbf{B}_i^u$, $\mathbf{B}_i^a$ and $\mathbf{B}_i^b$ are the matrices of shape function derivatives, which are defined as

$$\mathbf{B}_i = \begin{bmatrix} N_{i,x} & 0 \\ 0 & N_{i,y} \\ N_{i,y} & N_{i,x} \end{bmatrix} \tag{C.16a}$$

$$\mathbf{B}_i^a = \begin{bmatrix} (N_i H)_{,x} & 0 \\ 0 & (N_i H)_{,y} \\ (N_i H)_{,y} & (N_i H)_{,x} \end{bmatrix} \tag{C.16b}$$

$$\mathbf{B}_i^{b\alpha} = \begin{bmatrix} (N_i F_\alpha)_{,x} & 0 \\ 0 & (N_i F_\alpha)_{,y} \\ (N_i F_\alpha)_{,y} & (N_i F_\alpha)_{,x} \end{bmatrix} \quad (\alpha = 1,4) \tag{C.16c}$$

## C.4 Enrichment functions

Crack-tip enrichment functions are defined by the set of functions that span the asymptotic fields around the crack-tip [6]. Such displacement fields are given in (C.9) for a plane anisotropic solid. By expanding the summation in (C.9), these asymptotic dis-

placements may be expressed as follows:

$$u_1(r,\theta) = \sqrt{\frac{2r}{\pi}}[K_I(\Re\{A_{11}B_{11}^{-1}\beta_1 + A_{12}B_{21}^{-1}\beta_2\}) + K_{II}(\Re\{A_{11}B_{12}^{-1}\beta_1 + A_{22}B_{22}^{-1}\beta_2\})] \tag{C.17a}$$

$$u_2(r,\theta) = \sqrt{\frac{2r}{\pi}}[K_I(\Re\{A_{21}B_{11}^{-1}\beta_1 + A_{22}B_{21}^{-1}\beta_2\}) + K_{II}(\Re\{A_{21}B_{12}^{-1}\beta_1 + A_{22}B_{22}^{-1}\beta_2\})] \tag{C.17b}$$

where

$$\beta_i = \sqrt{\cos\theta + \mu_i \sin\theta} \tag{C.17c}$$

and $\mu_i$ are the eigenvalues from (C.8) with the positive imaginary part.

Therefore, four crack-tip enrichment functions may be directly derived from (C.17a) and (C.17b), to yield

$$F_l(r,\theta) = \sqrt{r}\begin{pmatrix} \Re\{A_{11}B_{11}^{-1}\beta_1 + A_{12}B_{21}^{-1}\beta_2\} \\ \Re\{A_{11}B_{12}^{-1}\beta_1 + A_{12}B_{22}^{-1}\beta_2\} \\ \Re\{A_{21}B_{11}^{-1}\beta_1 + A_{22}B_{21}^{-1}\beta_2\} \\ \Re\{A_{21}B_{12}^{-1}\beta_1 + A_{22}B_{22}^{-1}\beta_2\} \end{pmatrix} \tag{C.18}$$

which may be expressed in matrix form as

$$\mathbf{F}(r,\theta) = \sqrt{r}\left(\Re\left[\frac{\mathbf{B}^{-1}\mathbf{A}_1\boldsymbol{\beta}}{\mathbf{B}^{-1}\mathbf{A}_2\boldsymbol{\beta}}\right]\right) \tag{C.19}$$

where $\mathbf{A}_1$ and $\mathbf{A}_2$ correspond to the first and second row of matrix $\mathbf{A}$, respectively, and

$$\boldsymbol{\beta} = \begin{bmatrix} \beta_1 & 0 \\ 0 & \beta_2 \end{bmatrix} \tag{C.20}$$

The matrices $\mathbf{A}$ and $\mathbf{B}$ depend only on the material properties, but are independent of the adopted coordinate system and the geometry of the problem. In contrast to the isotropic enrichment functions, the anisotropic enrichment functions depend on the material properties of the domain, and are concisely obtained using the Stroh's formalism. It should be remarked that, from a mathematical point of view, Stroh's formalism is valid for anisotropic material behavior laws and it does not further lead to the isotropic enrichment functions, since this is a degenerate case where repeated roots occur for the characteristic equation of the material. However, the derived enrichment functions for anisotropic materials may be readily applied to the isotropic case by simply introducing a small perturbation to one of the repeated Stroh's eigenvalues, leading to stable and precise results as well.

## C.5 Computation of the stress intensity factors

As in previous extended finite element studies [2,13], we adopt the domain form of the contour interaction integral to calculate the stress intensity factors (SIFs). In order to make this paper self-contained, a brief description of this approach follows.

The classical path independent $J$-integral is expressed by [18]

$$J = \int_{\Gamma_q} (W\delta_{1j} - \sigma_{ij}u_{i,1})n_j \, d\Gamma_q \tag{C.21}$$

where the indexes $i$ and $j$ vary from 1 to 2 in a two-dimensional solid, $\Gamma_q$ is an arbitrary closed contour that contains the crack-tip, $n_j$ is the $j$-th component of the outward unit vector normal to such a contour, and $W$ is the strain energy density, which for a linear material can be expressed as

$$W = \frac{1}{2}(\sigma_{ij}\varepsilon_{ij}) \tag{C.22}$$

Applying the divergence theorem to (C.21) the following equivalent domain expression may be obtained for homogeneous materials:

$$J = \int_A (\sigma_{ij}u_{i,1} - W\delta_{1j})q_{,j} \, dA \tag{C.23}$$

where $A$ is the area inside the contour $\Gamma_q$ and $q$ is an arbitrary smoothing function such that it is unity at the crack tip and zero on $\Gamma_q$.

Next, let us consider two independent states: a principal one, which is the object of interest and denoted as state (1), and an auxiliary state, denoted as (2). This auxiliary state may be chosen to coincide with the crack-tip asymptotic field, so that it satisfies both equilibrium and the traction-free boundary condition on the crack surface. Such auxiliary state is expressed in terms of the generalized Stroh's formalism [24,27] in (C.9) and (C.10).

The superposition of these two states produces another equilibrium state [2, 13] for which the $J$-integral is

$$J^{(S)} = \int_A \left( (\sigma_{ij}^{(1)} + \sigma_{ij}^{(2)})(u_{i,1}^{(1)} + u_{i,1}^{(2)}) - W^{(S)}\delta_{1j} \right) q_{,j} dA \tag{C.24}$$

with

$$W^{(S)} = \frac{1}{2}\left[ (\sigma_{ij}^{(1)} + \sigma_{ij}^{(2)})(\varepsilon_{ij}^{(1)} + \varepsilon_{ij}^{(2)}) \right] \tag{C.25}$$

The $J$-integral in (C.24) can be further decomposed into three distinct integrals as

$$J^{(S)} = J^{(1)} + J^{(2)} + M^{(1,2)} \tag{C.26}$$

where $M^{(1,2)}$ is the interaction integral, defined as

$$M^{(1,2)} = \int_A (\sigma_{ij}^{(1)}u_{i,1}^{(2)} + \sigma_{ij}^{(2)}u_{i,1}^{(1)} - W^{(1,2)}\delta_{1j})q_{,j} dA \tag{C.27}$$

with

$$W^{(1,2)} = \frac{1}{2}(\sigma_{ij}^{(1)}\varepsilon_{ij}^{(2)} + \sigma_{ij}^{(2)}\varepsilon_{ij}^{(1)}) \tag{C.28}$$

The $J$-integral is related to the energy release rate, and it may be written in terms of the SIFs as [26]:

$$J = \frac{1}{2}\mathbf{K}_N\mathbf{Y}\mathbf{K}_N^T \tag{C.29}$$

where $\mathbf{K}_N = [K_I \quad K_{II}]$ and $\mathbf{Y}$ is the $(2\times 2)$ Irwin matrix, which depends on the material properties

$$\mathbf{Y} = \Re(i\cdot\mathbf{A}\mathbf{B}^{-1})$$

where $\mathbf{A}$ and $\mathbf{B}$ are defined in (C.8).

Thus, for plane problems, the following relation holds for every equilibrium state

$$J = \frac{1}{2}K_{II}^2 Y_{11} + \frac{1}{2}K_I^2 Y_{22} + K_I K_{II} Y_{12} \tag{C.30}$$

Substituting this expression into (C.26), the interaction integral $M^{(1,2)}$ can be rewritten as

$$\begin{aligned} M^{(1,2)} =& K_{II}^{(1)}K_{II}^{(2)}Y_{11} + K_I^{(1)}K_I^{(2)}Y_{22} + \\ & (K_I^{(1)}K_{II}^{(2)} + K_{II}^{(1)}K_I^{(2)})Y_{12} \end{aligned} \tag{C.31}$$

The individual mode $I$ and mode $II$ SIFs may be evaluated by solving the system of linear algebraic equations obtained from (C.31) by choosing appropriate auxiliary states. If the auxiliary state is chosen so that $K_I^{(2)} = 1$ and $K_{II}^{(2)} = 0$, (C.31) is reduced to

$$M^{(1,I)} = K_I^{(1)}Y_{22} + K_{II}^{(1)}Y_{12} \tag{C.32}$$

whereas selecting an auxiliary state satisfying $K_I^{(2)} = 0$ and $K_{II}^{(2)} = 1$, (C.31) is reduced to

$$M^{(1,II)} = K_{II}^{(1)}Y_{11} + K_I^{(1)}Y_{12} \tag{C.33}$$

Therefore, the determination of the SIF is reduced to solve the following system of linear equations:

$$\begin{pmatrix} M^{(1,II)} \\ M^{(1,I)} \end{pmatrix} = \mathbf{Y}\begin{pmatrix} K_{II}^{(1)} \\ K_I^{(1)} \end{pmatrix} \tag{C.34}$$

## C.6 Numerical results

The performance of the proposed enrichment functions is evaluated by solving several fracture problems. A convergence study is further conducted to characterize our approach. To this end, the obtained results are compared with available solutions in the

literature, derived either analytically or numerically by means of the boundary element method (BEM) [11, 23].

In all simulations bi-linear quadrilateral elements are used, with a $2 \times 2$ Gaussian quadrature for non-enriched finite elements and a $5 \times 5$ quadrature for elements with enriched nodes but not cut by the crack. The elements cut by the crack are partitioned into triangles [8], as Figure C.4 illustrates, and a 7 point triangular Gaussian quadrature is used within each subtriangle.

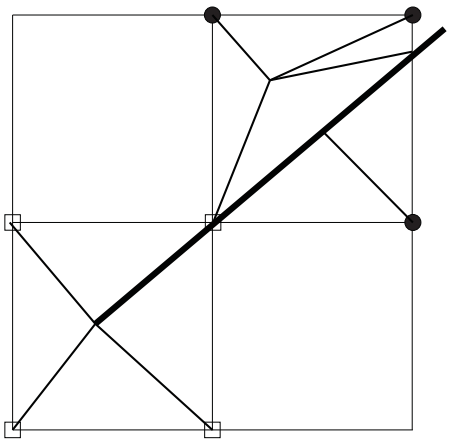

Figure C.4: Partitioning elements that are cut by a crack.

### C.6.1 Convergence study

Consider an anisotropic plate occupying $[0, 2a]^2$, with a center-crack of length $a$ with crack-tips located at $(a/2, a)$ and $(3a/2, a)$. The material properties of the anisotropic plate are given by: $C_{11} = 90.6448$ GPa, $C_{12} = 23.7448$ GPa, $C_{16} = 41.2055$ GPa, $C_{22} = 23.8568$ GPa, $C_{26} = 16.6346$ GPa and $C_{66} = 30.9390$ GPa.

The Dirichlet conditions corresponding to $K_I = 1$ and $K_{II} = 0$ are imposed on the boundaries. Convergence is analyzed in terms of the relative error in the energy norm, defined as

$$E_{rel} = \frac{||\mathbf{u} - \mathbf{u}^*||_{E(\Omega)}}{||\mathbf{u}^*||_{E(\Omega)}} = \frac{(\int_\Omega (\boldsymbol{\varepsilon} - \boldsymbol{\varepsilon}^*)^T \mathbf{C} (\boldsymbol{\varepsilon} - \boldsymbol{\varepsilon}^*) d\Omega)^{1/2}}{(\int_\Omega \boldsymbol{\varepsilon}^{*T} \mathbf{C} \boldsymbol{\varepsilon}^* d\Omega)^{1/2}}$$

where the superscript $*$ refers to the exact analytical solution for the displacement and strain fields.

Figure C.5 shows the obtained relative error in the energy norm versus the mesh density on a logarithmic scale. Results are obtained for both topological and geometrical enrichment strategies. The geometrical fixed area enrichment is done for two radii of the enriched domain, namely $r_e/a = 0.2$ and $r_e/a = 0.3$. Furthermore, two sets of enrichment functions are considered: the newly derived anisotropic crack-tip functions

proposed in this work, and the simpler enrichment functions for isotropic solids [9], namely

$$F_{iso}(r,\theta) = \left\{ \sqrt{r}\cos\frac{\theta}{2}, \sqrt{r}\sin\frac{\theta}{2}, \sqrt{r}\sin\frac{\theta}{2}\sin\theta, \sqrt{r}\cos\frac{\theta}{2}\sin\theta \right\}$$

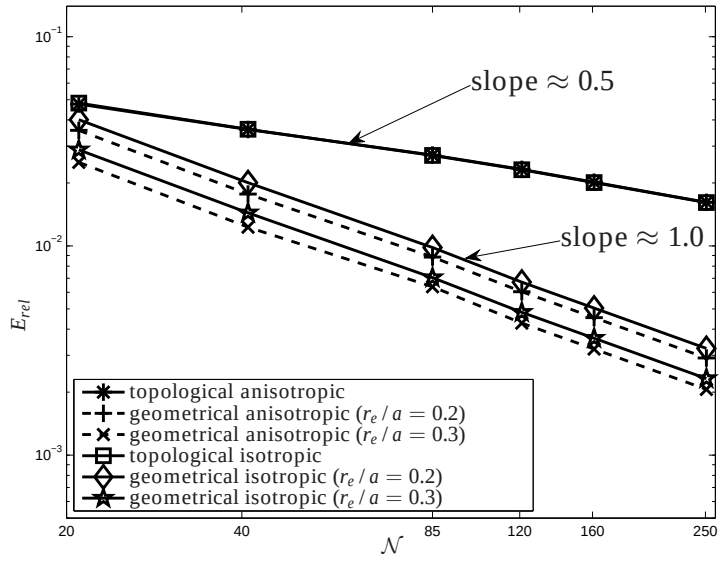


Figure C.5: Relative energy norm for different types of crack-tip enrichments.

It can be noticed that the errors in the energy norm calculated with topological enrichment are similar when using either the anisotropic or the isotropic crack-tip functions. However, differences are apparent with geometrical enrichment. For this case, although isotropic enrichment leads to a reasonable approximation with a simpler enrichment function, the error in the energy norm obtained with the isotropic enrichment functions is about 10% larger than the one obtained with the anisotropic enrichment functions. Convergence rates are in accordance with finite element theory and consistent with previous extended finite element studies [14, 25]: slopes of approximately 0.5 and 1 are obtained when using topological and geometrical enrichment, respectively.

### C.6.2 Center-crack in an orthotropic plate

A square plate ($h/w = 1$) with a center-crack of length $2a$ under uniform traction at two opposite sides is analyzed (Figure C.6). The size of the crack is defined by $a/w = 0.2$. Results are obtained using topological and geometrical enrichment (fixed area with $r_e/a = 0.3$), as well as with both the enrichment functions derived in this work for anisotropic behavior and the simpler isotropic enrichment functions.

Different material properties are considered. The shear modulus and the Poisson's

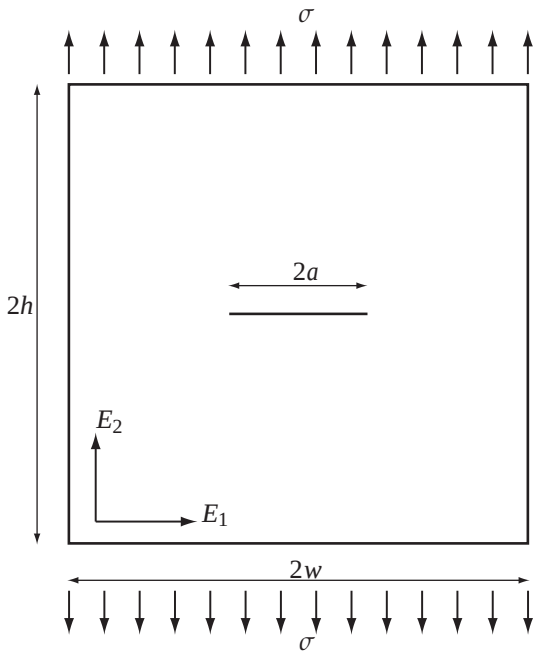


Figure C.6: Square plate with a center-crack under uniform traction.

ratio are fixed: $G_{12} = 6$ GPa and $\nu_{12} = 0.03$, and the Young moduli $E_1$ and $E_2$ are calculated from the expressions:

$$E_1 = G_{12}(\varphi + 2\nu_{12} + 1) \tag{C.35}$$

$$E_2 = E_1 / \varphi \tag{C.36}$$

with $\varphi$ being a material parameter defined by the ratio between Youngs moduli. The numerical results are compared with those obtained using the boundary element method in References [11, 23] and the extended finite element method in Reference [2].

The plate is discretized using two different $N_e \times N_e$ meshes, with $N_e = 45$ and $N_e = 85$. The normalized mode $I$ SIF ($K_I / (\sigma\sqrt{\pi a})$), calculated for several values of the material parameter $\varphi$ are shown in Figures C.7 and C.8 for the $N_e = 45$ and the $N_e = 85$ meshes, respectively.

It can be observed that the results obtained with X-FEM are in good agreement with the ones calculated via BEM and with the orthotropic X-FEM enrichment functions. Moreover, the geometrical enrichment leads to a slightly better approximation as compared to the topological enrichment. The difference in between the adopted reference BEM results [11] and the X-FEM results is shown in Table C.1 for the two FE meshes, as well as for the different enrichment strategies and crack-tip enrichment functions considered. Results are shown with a precision of four decimal digits so that comparisons to those obtained using isotropic enrichment functions can be made.

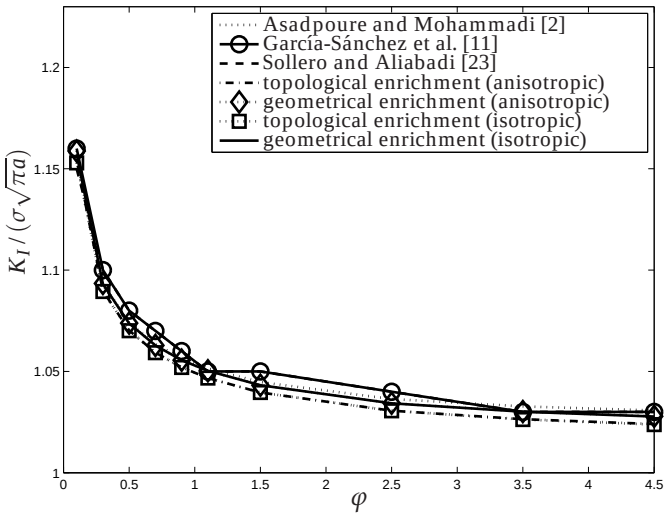


Figure C.7: Results for the orthotropic square plate with a center-crack ($45 \times 45$ FE mesh).

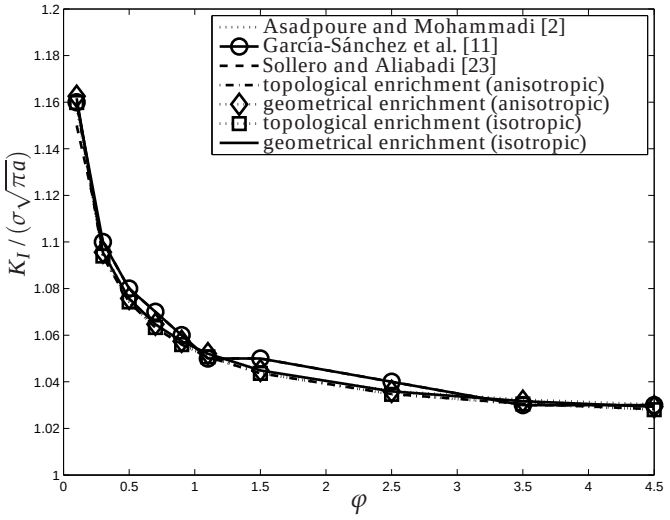


Figure C.8: Results for the orthotropic square plate with a center-crack ($85 \times 85$ FE mesh).

### C.6.3 Double edge-crack in an anisotropic plate

A square plate ($h/w = 1$) with a double edge-crack ($a/w = 0.5$) is considered. The plate is subjected to a uniform traction applied on opposite sides, as depicted in Figure C.9.

The plate is a symmetric angle ply composite laminate consisting of four graphite-

Table C.1: Difference (%) between the normalized mode *I* SIF obtained with X-FEM and the reference BEM solution [11]. Orthotropic plate with center-crack.

| $\varphi$ | $45 \times 45$ mesh | | | |
|---|---|---|---|---|
| | Anisotropic | | Isotropic | |
| | Topological | Geometrical | Topological | Geometrical |
| 0.1 | 0.4399 | 0.1097 | 0.4926 | 0.2413 |
| 0.3 | 0.8684 | 0.5986 | 0.8699 | 0.6294 |
| 0.5 | 0.8329 | 0.5740 | 0.8307 | 0.5849 |
| 0.7 | 0.9211 | 0.6685 | 0.9193 | 0.6722 |
| 0.9 | 0.6677 | 0.4191 | 0.6670 | 0.4198 |
| 1.1 | 0.2173 | 0.0286 | 0.2181 | 0.0290 |
| 1.5 | 0.8856 | 0.6468 | 0.8893 | 0.6466 |
| 2.5 | 0.7795 | 0.5476 | 0.7907 | 0.5508 |
| 3.5 | 0.2141 | 0.0167 | 0.2321 | 0.0097 |
| 4.5 | 0.4413 | 0.2116 | 0.4654 | 0.2220 |
| $\varphi$ | $85 \times 85$ mesh | | | |
| | Anisotropic | | Isotropic | |
| | Topological | Geometrical | Topological | Geometrical |
| 0.1 | 0.0323 | 0.2187 | 0.0609 | 0.1469 |
| 0.3 | 0.5883 | 0.3968 | 0.5881 | 0.4140 |
| 0.5 | 0.5726 | 0.3915 | 0.5706 | 0.3977 |
| 0.7 | 0.6693 | 0.4937 | 0.6679 | 0.4958 |
| 0.9 | 0.4207 | 0.2483 | 0.4202 | 0.2487 |
| 1.1 | 0.0263 | 0.1968 | 0.0259 | 0.1971 |
| 1.5 | 0.6504 | 0.4851 | 0.6527 | 0.4847 |
| 2.5 | 0.5546 | 0.3945 | 0.5607 | 0.3957 |
| 3.5 | 0.0069 | 0.1656 | 0.0023 | 0.1622 |
| 4.5 | 0.2231 | 0.0659 | 0.2349 | 0.0713 |

epoxy laminae, with the following elastic properties: $E_1 = 144.8$ GPa, $E_2 = 11.7$ GPa, $G_{12} = 9.66$ GPa and $\nu_{12} = 0.21$. To analyze the influence of the fiber orientation on the SIF, the fibers are rotated from $\phi = 0^\circ$ to $\phi = 90^\circ$.

Due to the symmetry of the problem, only half of the plate is discretized, using two different meshes with $45 \times 95$ and $85 \times 175$ elements, respectively. Figures C.10 and C.11 present the variation of the mode *I* normalized SIF $K_I / (\sigma\sqrt{\pi a})$ with respect to the direction of the fibers $\phi$ for each mesh. The normalized SIF calculated with X-FEM show good agreement with the reference BEM solutions [11, 23]. As expected, better results are obtained when using the finer mesh with geometrical enrichment (with $r_e / a = 0.3$).

The difference between the X-FEM results and the reference BEM solution [11] are given in Table C.2 for the $85 \times 175$ mesh.

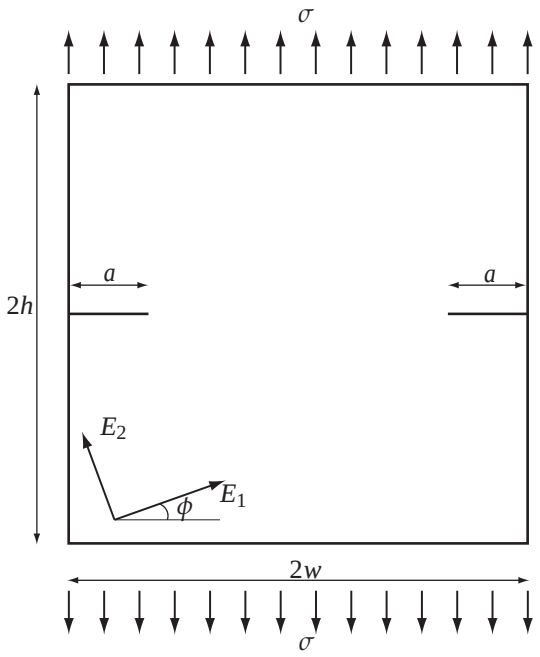


Figure C.9: Square plate with double edge-crack under uniform traction.

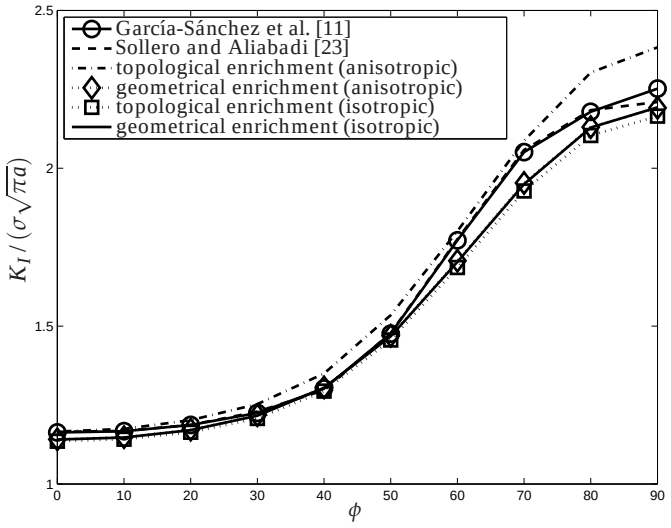


Figure C.10: Results for the anisotropic square plate with a double edge-crack ($45 \times 95$ FE mesh).

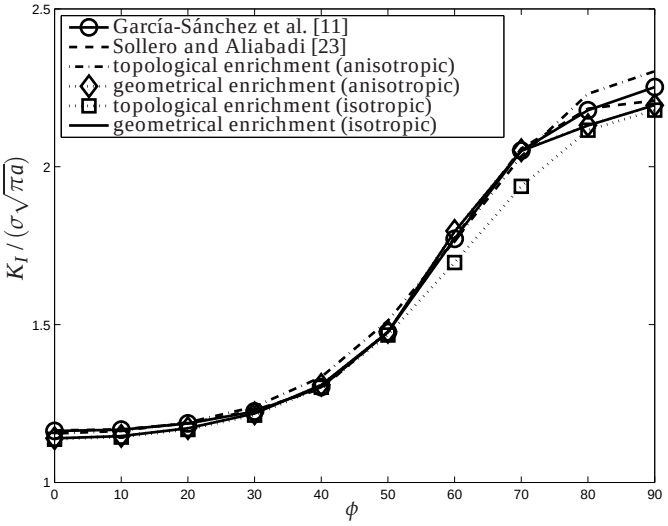


Figure C.11: Results for the anisotropic square plate with a double edge-crack (85 × 175 FE mesh).

Table C.2: Difference (%) between the normalized mode *I* SIF obtained with X-FEM and the reference BEM solution [11]. Plate with double edge-crack.

| $\phi(^\circ)$ | Anisotropic | | Isotropic | |
|---|---|---|---|---|
| | Topological | Geometrical | Topological | Geometrical |
| 0° | 2.3827 | 2.1387 | 2.4300 | 2.1759 |
| 10° | 2.0287 | 1.7646 | 2.0765 | 1.8033 |
| 20° | 1.5723 | 1.2415 | 1.6303 | 1.2894 |
| 30° | 1.2332 | 0.7937 | 1.2994 | 0.8480 |
| 40° | 0.3971 | 0.9580 | 0.3501 | 0.9058 |
| 50° | 0.7346 | 0.0557 | 0.7591 | 0.1322 |
| 60° | 4.4156 | 2.4605 | 4.4188 | 2.5704 |
| 70° | 5.8270 | 3.8994 | 5.8253 | 3.9919 |
| 80° | 3.1199 | 2.4017 | 3.1228 | 2.4335 |
| 90° | 1.3978 | 0.6911 | 1.3907 | 0.6614 |

### C.6.4 Slanted center-crack in an anisotropic plate

A rectangular plate ($h/w = 2$) with an inclined center-crack is considered (see Figure C.12). Uniform traction is applied on opposite sides of the plate. The material is a glass-epoxy composite with properties: $E_1 = 48.26$ GPa, $E_2 = 17.24$ GPa, $G_{12} = 6.89$ GPa and $\nu_{12} = 0.29$. The crack length is $2a = 0.4w$ and the crack is inclined at an angle of 45°. The directions of the fibers are rotated from $\phi = 0^\circ$ to 180°.

The numerical results are given in Figure C.13 for the normalized mode *I* SIF ($K_I/\sigma\sqrt{\pi a}$)

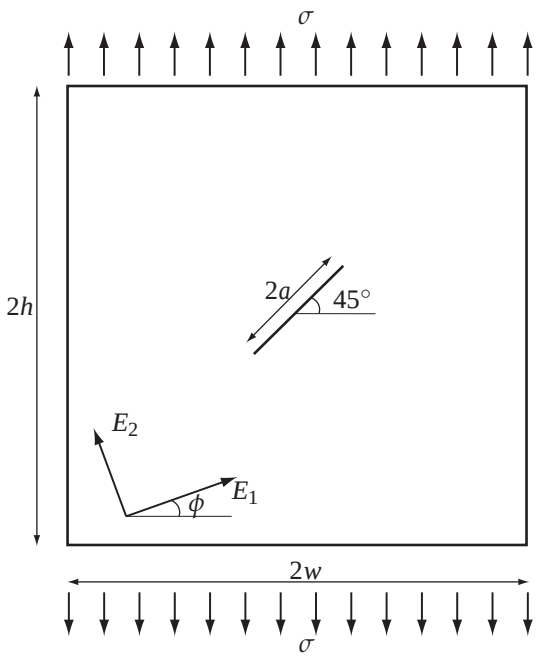


Figure C.12: Slanted center-crack under uniform traction.

and in Figure C.14 for the normalized mode $II$ SIF ($K_{II}/\sigma\sqrt{\pi a}$), considering a $85 \times 175$ mesh. As in previous examples, a normalized radius of $r_e/a = 0.3$ was adopted for the geometrical enrichment.

Good agreement is observed between the obtained X-FEM results and the reference BEM solution [11]. Differences between both sets of results are given in Tables C.3 and C.4.

## C.7 Concluding remarks

In this paper, we presented an extended finite element formulation for the analysis of fracture problems in plane fully anisotropic materials. New crack-tip enrichment functions were derived in a compact form using Stroh's formalism. Fracture parameters were accurately computed by means of the interaction integral method. Several crack configurations were analyzed, and the accuracy of the obtained results compared favorably with those available in the literature [11, 23]. Results based on anisotropic crack-tip enrichment functions was compared with those obtained using isotropic crack-tip functions. Furthermore, both topological and geometrical enrichment strategies were adopted, and it was demonstrated that the latter yielded better accuracy at the optimal rate of convergence in energy. Although the differences between both types of enrichment are small, the anisotropic enrichment function provide better results than

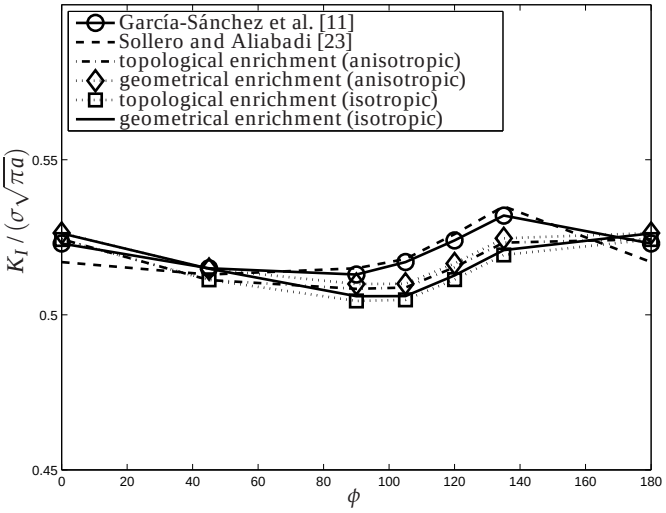


Figure C.13: Normalized mode *I* SIF for a slanted center-crack (85 × 175 FE mesh).

Table C.3: Difference (%) between the normalized mode *I* SIF obtained with X-FEM and the reference BEM solution [11]. Plate with slanted center-crack.

| $\phi$ | Anisotropic | | Isotropic | |
|---|---|---|---|---|
| | Topological | Geometrical | Topological | Geometrical |
| 0° | 0.1516 | 0.0962 | 0.1717 | 0.0819 |
| 45° | 1.1000 | 0.5624 | 1.0582 | 0.5048 |
| 90° | 1.1449 | 0.9689 | 1.9120 | 1.7344 |
| 105° | 1.8646 | 1.7598 | 2.6425 | 2.5376 |
| 120° | 1.9719 | 1.8644 | 2.7595 | 2.6561 |
| 135° | 1.9912 | 1.8579 | 2.7603 | 2.6226 |
| 180° | 0.1516 | 0.0962 | 0.1717 | 0.0819 |

the isotropic ones. The proposed formulation is versatile and can be extended to model coupled phenomena such as thermoelasticity, piezoelectricity and magnetoelectroelasticity. Moreover, the new enrichment functions allow one to explore other types of problems, such as crack identification in fully anisotropic two-dimensional materials.

## Acknowledgements

This work was funded by the *Ministerio de Ciencia e Innovación*, Spain, research project DPI2010-21590-C02-02.

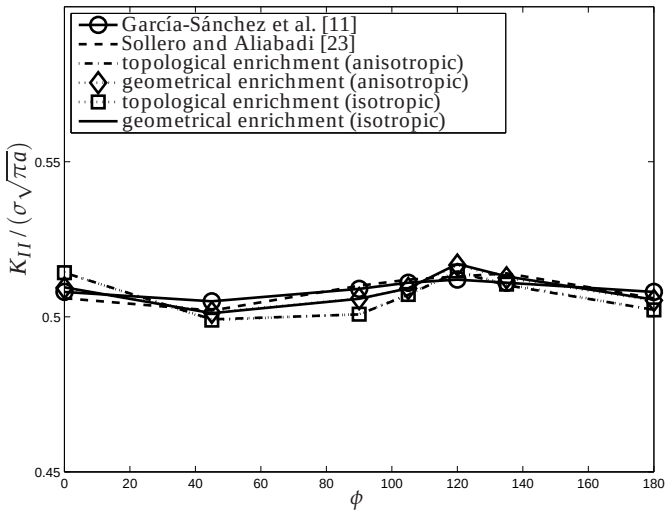


Figure C.14: Normalized mode *II* SIF for a slanted center-crack (85 × 175 FE mesh).

Table C.4: Difference (%) between the normalized mode *II* SIF obtained with X-FEM and the reference BEM solution [11]. Plate with slanted center-crack.

| $\phi$ | Anisotropic | | Isotropic | |
|---|---|---|---|---|
| | Topological | Geometrical | Topological | Geometrical |
| 0° | 0.3451 | 1.0546 | 0.3026 | 1.0808 |
| 45° | 1.6632 | 1.4036 | 1.6648 | 1.3965 |
| 90° | 1.8654 | 0.9698 | 1.8555 | 0.9723 |
| 105° | 0.9673 | 0.6836 | 0.9614 | 0.6816 |
| 120° | 0.2618 | 0.5503 | 0.2842 | 0.5850 |
| 135° | 0.4615 | 0.1919 | 0.4340 | 0.1528 |
| 180° | 2.0109 | 1.8399 | 2.0534 | 1.8661 |

## Bibliography

[1] S. Abbas and T. P. Fries. A unified enrichment scheme for fracture problems. *IOP Conference Series: Materials Science and Engineering*, 10(1):012045, 2010.

[2] A. Asadpoure and S. Mohammadi. Developing new enrichment functions for crack simulation in orthotropic media by the extended finite element method. *International Journal for Numerical Methods in Engineering*, 69:2150–2172, 2007.

[3] I. Babuška and J. M. Melenk. The partition of unity method. *International Journal for Numerical Methods in Engineering*, 4:607–632, 1997.

[4] E. Béchet, H. Minnebo, N. Möes, and B. Burgardt. Improved implementation and

robustness study of the X-FEM for stress analysis around cracks. *International Journal for Numerical Methods in Engineering*, 64:1033–1056, 2005.

[5] E. Béchet, M. Scherzer, and M. Kuna. Application of the X-FEM to the fracture of piezoelectric materials. *International Journal for Numerical Methods in Engineering*, 77:1535–1565, 2009.

[6] T. Belytschko and T. Black. Elastic crack growth in finite elements with minimal remeshing. *International Journal for Numerical Methods in Engineering*, 45:601–620, 1999.

[7] T. J. Boone, P. A. Wawrzynek, and A. R. Ingraffea. Finite element modelling of fracture propagation in orthotropic materials. *Engineering Fracture Mechanics*, 26:185–201, 1987.

[8] J. Dolbow, N. Moës, and T. Belytschko. An extended finite element method for modeling crack growth with frictional contact. *Computer Methods in Applied Mechanics and Engineering*, 190:6825–6846, 2001.

[9] M. Fleming, Y. A. Chu, B. Moran, and T. Belytschko. Enriched element-free Galerkin methods for crack tip fields. *International Journal for Numerical Methods in Engineering*, 40:1483–1504, 1997.

[10] T. P. Fries and T. Belytschko. The extended / generalized finite element method: An overview of the method and its applications. *International Journal for Numerical Methods in Engineering*, 84:253–304, 2010.

[11] F. García-Sánchez, A. Sáez, and J. Domínguez. Traction boundary elements for cracks in anisotropic solids. *Engineering Analysis with Boundary Elements*, 28:667–676, 2004.

[12] P. Laborde, J. Pommier, Y. Renard, and M. Salaün. High-order extended finite element method for cracked domains. *International Journal for Numerical Methods in Engineering*, 64:354–381, 2005.

[13] N. Möes, J. Dolbow, and T. Belytschko. A finite element method for crack growth without remeshing. *International Journal for Numerical Methods in Engineering*, 46:131–150, 1999.

[14] S. N. Mousavi, S. E. Generalized Gaussian quadrature rules for discontinuities and crack singularities in the extended finite element method. *Computer Methods in Applied Mechanics and Engineering*, 199(49-52):3237–3249, 2010.

[15] N. I. Muskhelishvili. *Some basic problems of the mathematical theory of elasticity*. Leiden: Noordhoff, 1953.

[16] C. C. Nobile, L. Fracture analysis for orthotropic cracked plates. *Composite Structures*, 68(3):285–293, 2005.

[17] E. Pan and B. Amadei. Fracture mechanics analysis of cracked 2-D anisotropic media with a new formulation of the boundary element method. *International Journal of Fracture*, 77:161–74, 1996.

[18] J. R. Rice. A path independent integral and the approximate analysis of strain concentration by notches and cracks. *Journal of Applied Mechanics*, 33:379–386, 1968.

[19] R. Rojas-Díaz, N. Sukumar, A. Sáez, and F. García-Sánchez. Fracture in magnetoelectroelastic materials using the extended finite element method. *International Journal for Numerical Methods in Engineering*, 88:1238–1259, 2011.

[20] G. C. Sih, P. C. Paris, and G. R. Irwin. On cracks in rectilinearly anisotropic bodies. *International Journal of Fracture*, 1:189–203, 1965.

[21] J. Sladek, V. Sladek, and S. N. Atluri. Meshless local Petrov-Galerkin method in anisotropic elasticity. *Computer Modeling in Engineering and Sciences*, 6:477–489, 2004.

[22] P. Sollero and M. H. Aliabadi. Fracture mechanics analysis of anisotropic plates by the boundary element method. *International Journal of Fracture*, 64:269–284, 1993.

[23] P. Sollero and M. H. Aliabadi. Anisotropic analysis of cracks in composite laminates using the dual BEM. *Composite Structures*, 31:229–233, 1995.

[24] A. N. Stroh. Dislocation and cracks in anisotropic elasticity. *Philosophical magazine*, 3:625–646, 1958.

[25] N. Sukumar, Z. Y. Huang, J. H. Prévost, and Z. Suo. Partition of unity enrichment for bimaterial interface cracks. *International Journal for Numerical Methods in Engineering*, 59:1075–1102, 2004.

[26] Z. Suo. Singularities, interfaces and cracks in dissimilar anisotropic media. *Proceedings of the Royal Society of London. Series A, Mathematical and Physical Sciences*, 427(1873):331–358, 1990.

[27] T. C. T. Ting. *Anisotropic Elasticity*. Oxford University Press, New York, 1996.

## Paper D: Far field Green's functions for time-harmonic loading in magnetoelectroelastic materials


- Conference name: Boundary Element Techniques and Meshless Methods (BeTeQ)
- Proceedings: Advances in Boundary Element & Meshless Techniques XIV
- Location and date: Paris, 2013
- Editors: A. Sellier and M. H. Aliabadi
- ISBN: 978-0-9576731-0-6

# Far field Green's fundamental solution for dynamic loading in magnetoelectroelastic materials

Authors: Gabriel Hattori, Andrés Sáez and Anders Boström

ABSTRACT

Smart materials such as magnetoelectroelastic (MEE) composites have been studied extensively in the last few years. These materials exhibit an inherent coupling between the elastic, electric and magnetic fields. One of the most widely used numerical tools for simulating its operation under both static and dynamic loading conditions is the boundary element method (BEM), which requires suitable Green's functions as the kernel of the method. Although such functions have been deduced for dynamic loading in terms of the Radon transform [6] by Rojas-Díaz et al. [9], the resulting fundamental solution is implicit, and it has to be computed in terms of surface integrals over a unit sphere, whose kernels show a highly oscillatory behavior for far field points. This fact leads to very time-consuming computational codes unless a far field asymptotic approximation is further developed

**Keywords**: Green's functions; BEM; magnetoelectroelastic materials; far-field.

## D.1 Introduction

The number of applications using smart materials has increased in the last few years. Sensors, actuators, transducers, electric generators, energy harvesters, medical applications, are just some of the recent applications of smart materials. The main characteristic of these materials is their coupling behavior. Examples of smart materials include the piezoelectric material, presenting coupling between the elastic and electric fields, and the magnetoelectroelastic (MEE) materials, presenting a more sophisticated coupling among the elastic, eletric and magnetic fields.

A number of authors have studied the behavior of these materials numerically using the boundary element method (BEM), which has been proved to be stable and accurate specially in fracture mechanics problems. The kernel of the BEM lays on the Green's functions, responsible for characterizing the behavior of the discretized medium, and it has been obtained for piezoelectric [2,5] and MEE materials [4,9] under different loading conditions. In particular, [9] obtained a Green's function through an integral over a unit radius sphere by means of the Radon transform [6]. In this case, the oscillatory

behavior of the integrand increases with the frequency, becoming infeasible the evaluation of the Green's function for high frequencies or when the distance between the collocation and the observation points is large.

To overcome this situation, a far field Green's functions have been deduced for MEE materials. The proposed approach is based on the work of [10], combining the residue theorem and the method of stationary phase.

## D.2 Formulation

The Hooke's law applied to a transversely isotropic MEE material with $x_3$ direction as the symmetry axis is given in Eq.(D.1) using the Voigt notation [11].

$$\begin{pmatrix} \sigma_{11} \\ \sigma_{22} \\ \sigma_{33} \\ \sigma_{23} \\ \sigma_{13} \\ \sigma_{12} \\ \hdashline D_1 \\ D_2 \\ D_3 \\ \hdashline B_1 \\ B_2 \\ B_3 \end{pmatrix} = \left(\begin{array}{cccccc:c:ccc:ccc} C_{11} & C_{12} & C_{13} & 0 & 0 & 0 & 0 & 0 & e_{31} & 0 & 0 & h_{31} \\ C_{12} & C_{22} & C_{23} & 0 & 0 & 0 & 0 & 0 & e_{31} & 0 & 0 & h_{31} \\ C_{13} & C_{23} & C_{33} & 0 & 0 & 0 & 0 & 0 & e_{33} & 0 & 0 & h_{33} \\ 0 & 0 & 0 & C_{44} & 0 & 0 & 0 & e_{15} & 0 & 0 & h_{15} & 0 \\ 0 & 0 & 0 & 0 & C_{44} & 0 & e_{15} & 0 & 0 & h_{15} & 0 & 0 \\ 0 & 0 & 0 & 0 & 0 & C_{66} & 0 & 0 & 0 & 0 & 0 & 0 \\ \hdashline 0 & 0 & 0 & 0 & e_{15} & 0 & -\epsilon_{11} & 0 & 0 & -\beta_{11} & 0 & 0 \\ 0 & 0 & 0 & e_{15} & 0 & 0 & 0 & -\epsilon_{11} & 0 & 0 & -\beta_{11} & 0 \\ e_{31} & e_{31} & e_{33} & 0 & 0 & 0 & 0 & 0 & -\epsilon_{33} & 0 & 0 & -\beta_{33} \\ \hdashline 0 & 0 & 0 & 0 & h_{15} & 0 & -\beta_{11} & 0 & 0 & -\gamma_{11} & 0 & 0 \\ 0 & 0 & 0 & h_{15} & 0 & 0 & 0 & -\beta_{11} & 0 & 0 & -\gamma_{11} & 0 \\ h_{31} & h_{31} & h_{33} & 0 & 0 & 0 & 0 & 0 & -\beta_{33} & 0 & 0 & -\gamma_{33} \end{array}\right) \begin{pmatrix} \varepsilon_1 \\ \varepsilon_2 \\ \varepsilon_3 \\ 2\varepsilon_{23} \\ 2\varepsilon_{13} \\ 2\varepsilon_{12} \\ \hdashline -E_1 \\ -E_2 \\ -E_3 \\ \hdashline -H_1 \\ -H_2 \\ -H_3 \end{pmatrix} \tag{D.1}$$

where $\sigma_{ij}$ represents the stress tensor, $D_i$ is the the electric displacement and $B_i$ is the magnetic induction; $C_{ij}$ represents the elastic stiffness tensor, $e_{ij}$, $h_{ij}$ and $\beta_{ij}$ represent the piezoelectric, the piezomagnetic and the electromagnetic coupling coefficients, respectively; $\epsilon_{ij}$ and $\gamma_{ij}$ are the dielectric permittivities and the magnetic permeabilities tensors, respectively; $\varepsilon_{ij}$ is the elastic strain tensor, $E_i$ is the electric field and $H_i$ is the magnetic field. In Eq. (D.1), $C_{66} = 0.5(C_{11} - C_{12})$.

The Navier's equation of a MEE material under harmonic loads can be defined as

$$C_{iJKl}u_{K,il} + \rho\omega^2\delta_{JK}u_K + b_J = 0 \tag{D.2}$$

where $C_{iJKl}$ is the 4-rank tensor of the constitutive matrix in Eq. (D.1), $\rho$ is the mass density of the material, $\omega$ is the angular frequency, $\delta_{JK}$ is the generalized Kronecker delta, $b_J$ is the generalized body forces vector and $u_K$ is defined as

$$u_K = \begin{cases} u_k, & \text{K=1,2,3} \\ \varphi, & \text{K=4} \\ \phi, & \text{K=5,} \end{cases} \tag{D.3}$$

where $u_k$ represent the elastic displacements, $\varphi$ is the electric potential and $\phi$ is the magnetic potential. The lowercase subscripts vary from 1 to 3, whilst the uppercase subscripts vary from 1 to 5.

After some mathematical manipulation, Eq. (D.2) can be redefined as

$$-\omega^2 \Lambda = a_4 \nabla^2 \Lambda + a_5 \frac{\partial^2 \Lambda}{\partial x_3^2} + \frac{\partial b_2}{\partial x_1} - \frac{\partial b_1}{\partial x_2} \tag{D.4}$$

$$-\omega^2 \Gamma = a_5 \nabla^2 \Gamma + a_2 \frac{\partial^2 \Gamma}{\partial x_3^2} + a_3 \frac{\partial^2 \Delta}{\partial x_3^2} + d_2 \nabla^2 \Psi + d_3 \frac{\partial^2 \Psi}{\partial x_3^2} + m_2 \nabla^2 \Phi + m_3 \frac{\partial^2 \Phi}{\partial x_3^2} + \frac{\partial b_3}{\partial x_3} \tag{D.5}$$

$$-\omega^2 \Delta = a_3 \nabla^2 \Gamma + a_1 \nabla^2 \Delta + a_5 \frac{\partial^2 \Delta}{\partial x_3^2} + d_1 \nabla^2 \Psi + m_1 \nabla^2 \Phi + \frac{\partial b_1}{\partial x_1} + \frac{\partial b_2}{\partial x_2} \tag{D.6}$$

$$0 = d_2 \nabla^2 \Gamma + d_3 \frac{\partial^2 \Gamma}{\partial x_3^2} + d_1 \frac{\partial^2 \Delta}{\partial x_3^2} + d_4 \nabla^2 \Psi + d_5 \frac{\partial^2 \Psi}{\partial x_3^2} + z_4 \nabla^2 \Phi + z_5 \frac{\partial^2 \Phi}{\partial x_3^2} + \frac{\partial b_4}{\partial x_3} \tag{D.7}$$

$$0 = m_2 \nabla^2 \Gamma + m_3 \frac{\partial^2 \Gamma}{\partial x_3^2} + m_1 \frac{\partial^2 \Delta}{\partial x_3^2} + z_4 \nabla^2 \Psi + z_5 \frac{\partial^2 \Psi}{\partial x_3^2} + m_4 \nabla^2 \Phi + m_5 \frac{\partial^2 \Phi}{\partial x_3^2} + \frac{\partial b_5}{\partial x_3} \tag{D.8}$$

where $\nabla^2 = \frac{\partial^2}{\partial x_1^2} + \frac{\partial^2}{\partial x_2^2}$ and the auxiliary variables are given by

$$\Lambda = \frac{\partial u_2}{\partial x_1} - \frac{\partial u_1}{\partial x_2}, \quad \Delta = \frac{\partial u_1}{\partial x_1} + \frac{\partial u_2}{\partial x_2}, \quad \Gamma = \frac{\partial u_3}{\partial x_3}, \quad \Psi = \frac{\partial \varphi}{\partial x_3}, \quad \Phi = \frac{\partial \phi}{\partial x_3} \tag{D.9}$$

and the material constants are defined as

$$a_1 = \frac{C_{11}}{\rho}, \quad a_2 = \frac{C_{33}}{\rho}, \quad a_3 = \frac{C_{13} + C_{44}}{\rho}, \quad a_4 = \frac{C_{11} - C_{12}}{2\rho}, \quad a_5 = \frac{C_{44}}{\rho}$$

$$d_1 = \frac{e_{15} + e_{31}}{\rho}, \quad d_2 = \frac{e_{15}}{\rho}, \quad d_3 = \frac{e_{33}}{\rho}, \quad d_4 = \frac{-\epsilon_{11}}{\rho}, \quad d_5 = \frac{-\epsilon_{33}}{\rho}$$

$$m_1 = \frac{h_{15} + h_{31}}{\rho}, \quad m_2 = \frac{h_{15}}{\rho}, \quad m_3 = \frac{h_{33}}{\rho}, \quad m_4 = \frac{-\gamma_{11}}{\rho}, \quad m_5 = \frac{-\gamma_{33}}{\rho}$$

$$z_4 = \frac{-\beta_{11}}{\rho}, \quad z_5 = \frac{-\beta_{33}}{\rho}$$

The solution of Eqs. (D.4) to (D.8) can be easily obtained through application of the Fourier transform. Hence, taking for example the auxiliary variable $\Lambda$ we obtain

$$\Lambda = \int \int \int_{-\infty}^{\infty} \overline{\Lambda}\, exp(i\boldsymbol{\alpha}.\mathbf{x})\, d\boldsymbol{\alpha} \tag{D.10}$$

where the overbar indicates the Fourier transformed variables and $\boldsymbol{\alpha} = (\alpha_1, \alpha_2, \alpha_3)$ is the wave number vector. Similar expressions can be obtained for the remaining auxiliary variables $\overline{\Delta}$, $\overline{\Gamma}$, $\overline{\Psi}$ and $\overline{\Phi}$. Thus, the Cartesian displacements transforms $\overline{u}_1$, $\overline{u}_2$, $\overline{u}_3$, $\overline{\varphi}$ and $\overline{\phi}$ can be defined as

$$\overline{u}_1 = \frac{\alpha_1\overline{\Delta} - \alpha_2\overline{\Lambda}}{i(\alpha_1^2+\alpha_2^2)}, \quad \overline{u}_2 = \frac{\alpha_1\overline{\Delta} + \alpha_2\overline{\Lambda}}{i(\alpha_1^2+\alpha_2^2)}, \quad \overline{u}_3 = \frac{\overline{\Gamma}}{i\alpha_3}, \quad \overline{\varphi} = \frac{\overline{\Psi}}{i\alpha_3}, \quad \overline{\phi} = \frac{\overline{\Phi}}{i\alpha_3}, \tag{D.11}$$

Lighthill [7] has used the Fourier transform with a mixed approach of the residue theorem and the stationary phase method, further extended to elastodynamics by Buchwald [1] and used by Sáez and Domínguez [10] for the calculation of far field Green's functions. An asymptotic aproximation for $u_K$ can be defined for large values of $\mathbf{x}$ and is expressed by

$$u_K \approx \frac{4\pi^2}{|\mathbf{x}|}\left(\sum_{r=1}^{N_H}\frac{C_{H_r} f_{K_H}(\boldsymbol{\alpha}^{(r)})}{\sqrt{|K_{H_r}||\nabla H^{(r)}|}} exp(i\boldsymbol{\alpha}^{(r)}.\mathbf{x}) + \sum_{p=1}^{N_G}\frac{C_{G_r} f_{K_G}(\boldsymbol{\alpha}^{(p)})}{\sqrt{|K_{G_p}||\nabla G^{(p)}|}} exp(i\boldsymbol{\alpha}^{(p)}.\mathbf{x})\right) \tag{D.12}$$

where $f_{H_r}$ represents the body forces; $N_H$ is the number of points on the surface $H=0$ where the normal is parallel to $\mathbf{x}$ and $\boldsymbol{\alpha}^{(r)}\mathbf{x} > 0$; $\nabla H^{(r)}$ is the gradient of $H=0$ at the $\boldsymbol{\alpha}^{(r)}$ positions; $K_{H_r}$ is the Gaussian curvature of $H=0$, defined as $K_{H_r} = \kappa_{H_1}\kappa_{H_2}$, being $\kappa_{H_1}$ and $\kappa_{H_2}$ the principal curvatures of the surface $H=0$; and $C_{H_r} = exp(\frac{1}{4}\pi i(sgn\ \kappa_{H_1} + sgn\ \kappa_{H_2}))$. The variables $f_{G_r}$, $N_G$, $\nabla G^{(r)}$, $K_{G_r}$ and $C_{G_r}$ are defined analogously for the surface $G=0$.

Applying the Fourier transform in Eq. (D.4), the surface $G=0$ can be stated as

$$G(\alpha_1,\alpha_2,\alpha_3) = a_4(\alpha_1^2+\alpha_2^2) + a_5\alpha_3^2 - \omega^2 = 0 \tag{D.13}$$

which is the slowness surface equation for purely transversal motions. In this class of material the sheet of the slowness surface associated to the purely transversal motion is uncoupled.

The surface $H=0$ is a quartic which represents the quasi-longitudinal and the quasi-transversal motions. The equation describing both slowness surfaces can be obtained through application of the Fourier transform in Eqs. (D.5) to (D.8), obtaining the following linear system

$$\begin{bmatrix} a_5(\alpha_1^2+\alpha_2^2)+a_2\alpha_3^2-\omega^2 & a_3\alpha_3^2 & d_2(\alpha_1^2+\alpha_2^2)+d_3\alpha_3^2 & m_2(\alpha_1^2+\alpha_2^2)+m_3\alpha_3^2 \\ a_3(\alpha_1^2+\alpha_2^2) & a_1(\alpha_1^2+\alpha_2^2)+a_5\alpha_3^2-\omega^2 & d_1(\alpha_1^2+\alpha_2^2) & m_1(\alpha_1^2+\alpha_2^2) \\ d_2(\alpha_1^2+\alpha_2^2)+d_3\alpha_3^2 & d_1\alpha_3^2 & d_4(\alpha_1^2+\alpha_2^2)+d_5\alpha_3^2 & z_4(\alpha_1^2+\alpha_2^2)+z_5\alpha_3^2 \\ m_2(\alpha_1^2+\alpha_2^2)+m_3\alpha_3^2 & m_1\alpha_3^2 & z_4(\alpha_1^2+\alpha_2^2)+z_5\alpha_3^2 & m_4(\alpha_1^2+\alpha_2^2)+m_5\alpha_3^2 \end{bmatrix} \cdots$$

$$\cdots \begin{pmatrix} \overline{\Gamma} \\ \overline{\Delta} \\ \overline{\Psi} \\ \overline{\Phi} \end{pmatrix} = \begin{pmatrix} \overline{\frac{\partial b_3}{\partial x_3}} \\ \overline{\frac{\partial b_1}{\partial x_1} + \frac{\partial b_2}{\partial x_2}} \\ \overline{\frac{\partial b_4}{\partial x_3}} \\ \overline{\frac{\partial b_5}{\partial x_3}} \end{pmatrix} \equiv \mathbf{Ax} = \mathbf{b} \tag{D.14}$$

where

$$H(\alpha_1, \alpha_2, \alpha_3) = det(\mathbf{A}) = 0 \tag{D.15}$$

To simplify the formulation, an auxiliary system of coordinates has been used, and it is illustrated in Fig. D.1, where $x_3 \equiv x_3'$ and $x_1'$ has the direction of the projection of $\mathbf{x}$ over the plane $x_1 - x_2$. In the new coordinate system, $\alpha_2^{(r)} = 0$, enforcing the fundamental solution expressions (and its derivatives) represented in the $x_2'$ direction to be zero.

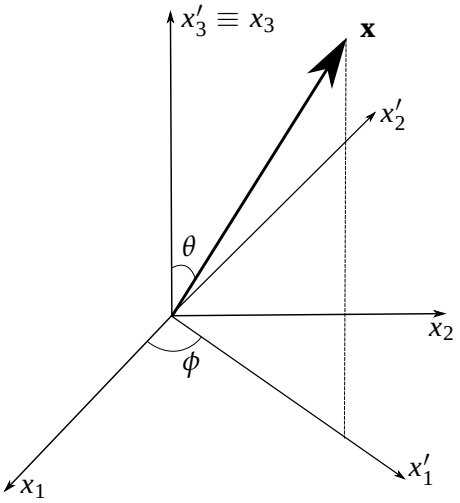


Figure D.1: Auxiliary coordinate system.

As studied by Payton [8] and Sáez and Domínguez [10], the surface $G = 0$ is an ellipsoid, therefore there is only one $\boldsymbol{\alpha}^{(p)}$ point. The quartic $H$ can be decomposed in two sheets corresponding to the quasi-longidutinal and quasi-transversal motions, $H_-$ and $H_+$ respectively. Duff [3] has shown that the quasi-longitudinal slowness surface is always convex, thus containing only one $\boldsymbol{\alpha}^{(p)}$ point. The $H_+$ surface may be convex or not, depending on the class type of the analyzed material, having at least one and at most three $\boldsymbol{\alpha}^{(r)}$ points. An extensive study on the classification of materials can be found in [8].

The determination of the $\boldsymbol{\alpha}^{(r)}$ can be simplified by the use of cylindrical coordinates. The quartic $H = 0$ can be redefined in terms of polar coordinates as

$$\alpha_1 = R(\theta)sin(\theta), \quad \alpha_3 = R(\theta)cos(\theta) \tag{D.16}$$

$$H = A(\theta)R(\theta)^4 - \omega^2 B(\theta)R(\theta)^2 + C(\theta)\omega^4 = 0$$

$$\Rightarrow R_\pm(\theta) = \omega \left( \frac{B(\theta) \pm \sqrt{B(\theta)^2 - 4A(\theta)C(\theta)}}{2A(\theta)} \right)^{1/2} \tag{D.17}$$

where $R_\pm(\theta)$ defines the $H_\pm$ sheet. The variables $A(\theta)$, $B(\theta)$ and $C(\theta)$ are determined

substituting Eq. (D.16) in (D.15). The values of $\theta$ corresponding to the desired $\boldsymbol{\alpha}$ are obtained from the solution of the non-linear equation

$$R(\theta)(cos\theta e'_{x1} - sin\theta e'_{x3}) + \frac{dR(\theta)}{d\theta}(sin\theta e'_{x1} + cos\theta e'_{x3}) = 0 \tag{D.18}$$

where $e'_{x1}$ and $e'_{x3}$ are the cosine directors of $\mathbf{x}$ in the new coordinate system.

## D.3 Numerical results

To validate the proposed far field approach, a degenerate isotropic material has been considered. The material constants are: $C_{11} = C_{33} = 283$ GPa, $C_{12} = C_{13} = 121$ GPa, $C_{44} = 80.8$ GPa and the rest are neglected. In this case, the slowness surfaces are convex, therefore there is only one $\boldsymbol{\alpha}^{(r)}$ point. The results for the displacement due to a point load, both in the $x_3$ direction, are illustrated in Figs. D.2 and D.3, where $C_L = \sqrt{C_{33}/\rho}$ and $r$ is the distance taken between the point where to load is applied and the position where the displacements are measured, forming an angle $\theta$ in respect to the $x_3$ direction in this work. One can verify that the solution obtained with the far field formulation has a perfect agreement with the analytical solution (see [10]).

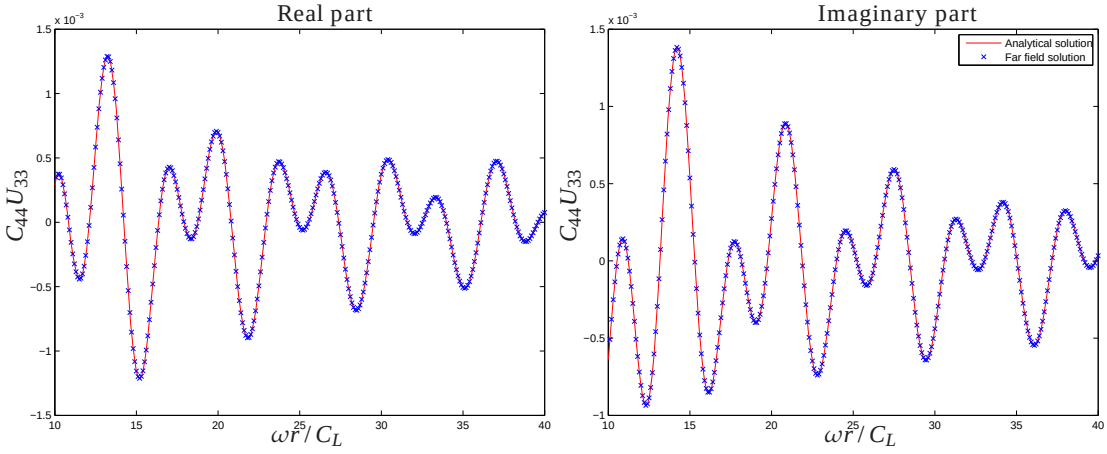


(a) (b)

Figure D.2: $U_{33}$ displacement for $\theta = 30$.

## D.4 Summary

This work proposes a new set of far field Green's functions for MEE materials under time-harmonic loadings. The method is similar to the one developed by Sáez and

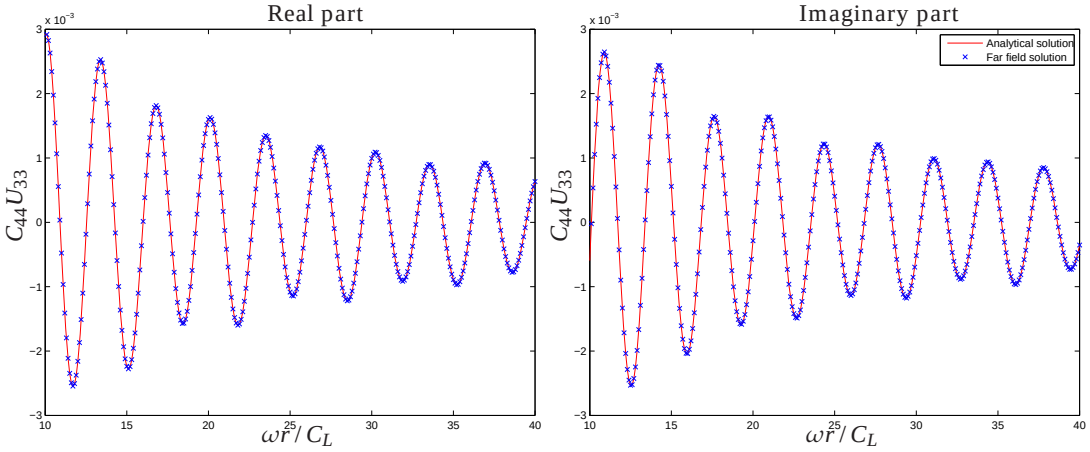


(a) (b)

Figure D.3: $U_{33}$ displacement for $\theta = 60$.

Domínguez [10] for general transversely isotropic materials. A large computational gain is achieved due to the absence of implicit integration in the formulation, which is particularly important in 3D problems.

## Acknowledgments

This work was funded by the research project DPI2010-21590-C02-02 from the Spanish *Ministerio de Economía y Competitividad* and the Excelence research project P09-TEP-5054 from the *Junta de Andalucía*.

## Bibliography

[1] V. T. Buchwald. Elastic waves in anisotropic media. *Philosophical Transactions of the Royal Society of London. Series A, Mathematical and Physical Sciences*, 253(1275):563–580, 1959.

[2] M. Denda, Y. Araki, and Y. K. Yong. Time-harmonic BEM for 2-D piezoelectricity applied to eigenvalue problems. *International Journal of Solids and Structures*, 26:7241–7265, 2004.

[3] G. F. D. Duff. The Cauchy problem for elastic waves in an anisotropic medium. *Philosophical Transactions of the Royal Society of London. Series A, Mathematical and Physical Sciences*, 252(1010):pp. 249–273, 1960.

[4] F. García-Sánchez, R. Rojas-Díaz, A. Sáez, and C. Zhang. Fracture of magnetoelectroelastic composite materials using boundary element method (BEM). *Theoretical and Applied Fracture Mechanics*, 47(3):192–204, 2007.

[5] F. García-Sánchez, A. Sáez, and J. Domínguez. Anisotropic and piezoelectric materials fracture analysis by BEM. *Computer and Structures*, 83:804–820, 2005.

[6] S. Helgason. *The Radon transform*. Birkhuser, 1980.

[7] M. J. Lighthill. Studies on magneto-hydrodynamic waves and other anisotropic wave motions. *Philosophical Transactions of the Royal Society of London. Series A, Mathematical and Physical Sciences*, 252(1014):397–430, 1960.

[8] R. G. Payton. *Elastic wave propagation in transversely isotropic media*. M. Nijhoff Publishers, 1983.

[9] R. Rojas-Díaz, A. Sáez, F. García-Sánchez, and C. Zhang. Time-harmonic Green's functions for anisotropic magnetoelectroelasticity. *International Journal of Solids and Structures*, 45:144–158, 2008.

[10] A. Sáez and J. Domínguez. Far field dynamic Green's functions for BEM in transversely isotropic solids. *Wave motion*, 32 (2):113–123, 2000.

[11] W. Voigt. *Lehrbuch der Kristallphysik*. B.G. Teubner, 1928.

## Paper E: An experimental approach for crack identification/assessment in piezoelectric materials


- Conference name: 10th World Congress on Computational Mechanics (WCCM)
- Location and date: São Paulo, 2012
- Paper ID: 18052
- ISBN: 978-85-86686-70-2

# An experimental approach for crack identification/assessment in piezoelectric materials

Authors: Gabriel Hattori, Samir Mustapha, Lin Ye and Andrés Sáez

ABSTRACT

In this work, an experimental approach for the identification of through thickness cracks in piezoelectric materials is presented, where the electric potential on the surface of the PZT elements was measured at different locations before and after the crack was introduced. A damage index (DI) was defined, based on the amount of change in electrical potential between the intact and damaged states, which was later used to develop an algorithm for identifying and assessing cracks in a PZT element under a time harmonic load. Cracks of different lengths, depths and orientation were successfully identified.

**Keywords**: PZT; Electric potential; Cracks; Damage identification.

## E.1 Introduction

Piezoelectricity is the phenomenon described as an electric field is generated upon applying a mechanical load and vice versa. This effect is utilized for the development of piezoelectric sensors and actuators. Piezoelectric wafer active sensors (PWAS) are relatively cheap and make use of the piezoelectric principles. For many years, PWAS was used in structural health monitoring (SHM) for generation of guided waves which have high sensitivity to surface and embedded structural damage. They have been widely used to develop various damage identification algorithms for assessing delamination, de-bonding, holes, cracks / notches and corrosion in both composite and metallic materials [2, 3, 7, 11, 12, 14].

The behavior of the piezoelectric materials (e.g. PZT) has been studied extensively in the past decades. Researchers have focused on the study of the effect of damage on the measured dynamic response of structures where PZT elements were used as actuators or sensors. However, limited attention has been directed towards monitoring the state of the PZT elements themselves, which is considered very critical in order to ensure that the acquired data host structure are trustful.

PZT sensors are usually brittle and could easily crack, several reports indicated that a positive electrical field applied to the PZT ceramic could slow down the crack propagation, however a negative electrical field would have an contrary effect [9,13,16]. Putting

a structural component in service with the piezoelectric ceramics installed on it, entails the need for evaluation methods to access the integrity of the structural health monitoring system itself during the life service. A minimum amount of work have focused on inspection of the sensors, while some researchers have focused on numerically simulation the change in electric potential due to the existence of crack or damage [4,8,10], on the other hand no experimental results has been recalled.

In this work, PZT ceramics with different types of damage including through thickness cracks and holes were assessed experimentally. Measures of the electric potential are taken at different locations on the PZT surface and compared to the original state. A damage index is defined and a hybrid scheme is proposed, using probabilistic analysis, sensing paths and mapping of the damage indexes.

## E.2 Experiment

### E.2.1 Sample preparation and experimental set-up

Two PZT plate measuring 50 x 50 mm (PQYY+0598) with a thickness of 1mm were bonded to an aluminum plate (60 x 60 mm acting like a substrate) using LOCTITE© super glue. The properties of the PZT ceramic are shown in Table E.1 [1]. Another circular PZT element measuring 10 mm in diameter and 1 mm in thickness was placed on the opposite side of the aluminum plate and located in the middle of the plate as shown in Fig. E.1 functioning as actuator.

Table E.1: Piezoelectric plate properties.

| **Physical and dielectric properties** | | PIC 151 | Unit | Value |
|---|---|---|---|---|
| Density | | $\rho$ | $Kg/m^3$ | 7800 |
| Curie temperature | | $T_c$ | $^\circ C$ | 250 |
| Relative permittivity | In the polarization direction | $\epsilon_{33}^T/\epsilon_0$ | - | 2400 |
| | Direction $\perp$ to the polarity | $\epsilon_{11}^T/\epsilon_0$ | - | 1980 |
| **Electro-mechanical properties** | | | | |
| Coupling factor | | $K_p$ | - | 0.62 |
| | | $K_t$ | - | 0.53 |
| | | $K_{31}$ | - | 0.38 |
| | | $K_{33}$ | - | 0.69 |
| Piezoelectric voltage coefficient | | $d_{31}$ | $10^{-12}C/N$ | $-210$ |
| | | $d_{33}$ | | 500 |
| Piezoelectric voltage coefficient | | $g_{31}$ | $10^{-3}Vm/N$ | $-11.5$ |
| | | $g_{33}$ | - | 22 |

A sinusoidal tone burst enclosed in a Hanning window with peak-to-peak voltage of 15 Volts was used as the input signal for the actuator. Activation and acquisition

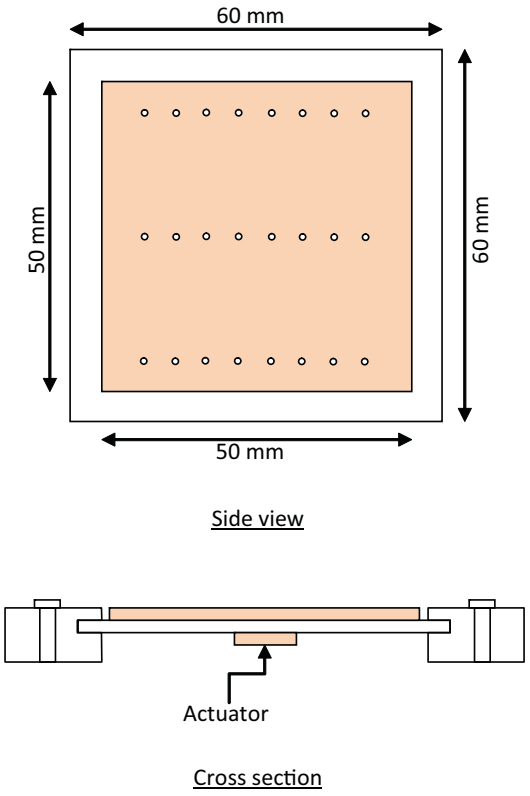


Figure E.1: Schematic view of the experiment set-up.

of wave signals were fulfilled using an active signal generation and data acquisition system developed on the VXI platform, consisting mainly of a signal generation unit (Agilent© E1441), signal amplifier (PiezoSys EPA-104), signal conditioner (Agilent© E3242A) and signal digitizer (Agilent© E1437A). The wave signals were captured at a sampling rate of 20.48 MHz. The acquisition duration was set to insure that the activated wave modes were captured. Three damage cases were introduced into the ceramic plate and they are summarized in Fig. E.2. The panels were clamped at the four edges during the experiment. Twenty four measurements of the electrical potential were taken on top of the plate as show in Fig. E.2.

The objective of this set-up is to determine the influence of different types of damage on the measure of the electric potential. It may be seen that is straight forward to detect damage in a PZT plate, however is slightly difficult to quantify it accordingly.

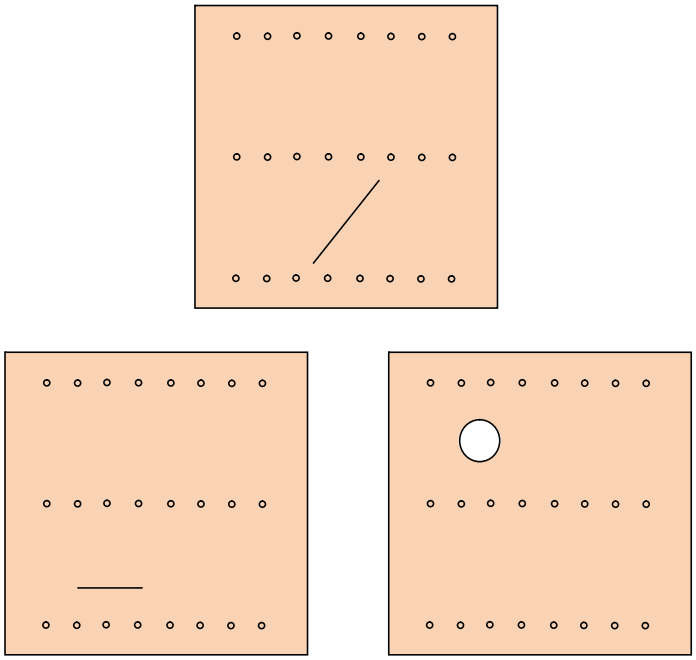

Figure E.2: Damage cases tested.

## E.3 Signal processing and data fusion

The applied methodology for damage identification in piezoelectric materials was to define a damage index (DI) as the quantification of the damage influence on the acquired signal. The DI was calculated using the correlation between two different states, i.e. the damaged and the undamaged, and it is stated as

$$\rho_{x,y} = \frac{n\sum x_i y_i - \sum x_i \sum y_i}{\sqrt{\left(n\sum x_i^2 - (\sum x_i)^2\right)\left(n\sum y_i^2 - (\sum y_i)^2\right)}} \tag{E.1}$$

where **x** and **y** are two signals with $n$ entries. Low values of the correlation indicates that the damage is very close to the point of inspection, in contrast, high values means that the damage is far away.

Data fusion is applied to obtain an approximation of the area affected by the damage. This scheme has the advantage of providing a graphical solution in the considered domain. A number of sensing paths $D_{sk}$ is considered, taken from the known measuring points $S_m$ ($m = 1 \cdots 24$) to a specific position $(x, y)$ on the plate. The probability of the presence of damage (POD) can be defined as [15]

$$P(x,y) = \sum_{k=1}^{M} DI_k W_k \tag{E.2}$$

where $M$ is the number of measurements, $DI_k = 1 - |\rho_{x,y}|$ is the damage index and $W_k$ is a weight parameters which depends on the distance between position $(x, y)$ and the $k$th measuring point. In this work, a Gaussian distribution was used in order to smooth the distribution of the damage index. The parameter $W_k$ can be written as

$$W_k = \frac{1}{\sigma\sqrt{2\pi}} exp\left(-\frac{D_{sk}^2}{2\sigma^2}\right) \tag{E.3}$$

with the standard deviation parameter $\sigma = 12$ mm.

## E.4 Results

A 5-cycles toneburst wave at the centered frequency of 200 kHz was used as exciting signal, except if specified differently. The current response corresponds to the actual damage state of the PZT plate, and it is compared to a reference state, composed by the measures of the previous state. Damages were introduced into the PZT plate and their assessment will be presented in the following sections.

### E.4.1 Slanted crack identification

A slanted crack centered at the position (25.95;14.5) mm with length 21.58 mm and orientation $\theta = 56.5^\circ$ is analysed. Due to the particularity of the material properties, the results are very similar at all measuring positions. The measured signals in Fig. E.3 represent the comparison of the present and reference state at the position (27.65;25.0) mm.

The difference in the amplitude of signals is clearly identified, and in addition the crack resulted in some time delay between both states. It may be challenging to extract the damage features from the signals in order to located and assess the damage.

As stated before, the damage index depends on the correlation of the signals from different states. High values indicate a significant difference of both signals, whilst small values implicate that the signals are very identical to each other. Fig. E.4 includes the data fusion of the probability image of the damage, calculated using Eq. (E.2), where the DI is obtained from the present and reference states. The data fusion of the results in this damage cases did not give precise prediction of the crack location, which may be attributed to two factors: (a) the signal obtained from the damage state is very identical to the reference one, and (b) the actuator is fixed at the center of the plate, therefore it may restrict the damage sensitivity provided by the input signal.

An alternative was to map the current DI into a new configuration, where the information concerning the state of the plate is the same, and still allowing the data fusion to present relevant information of the probability of damage in the plate. This approach

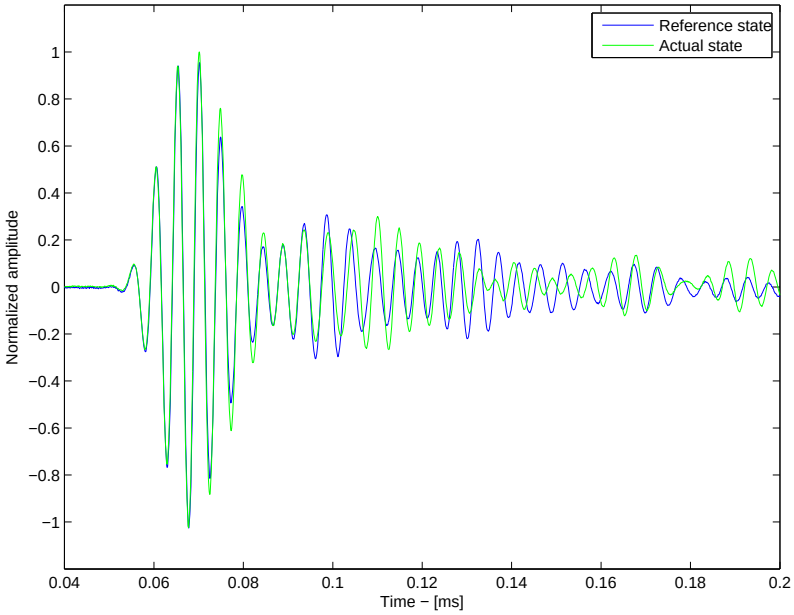


Figure E.3: Comparation between present (damaged) and reference (undamaged) states.

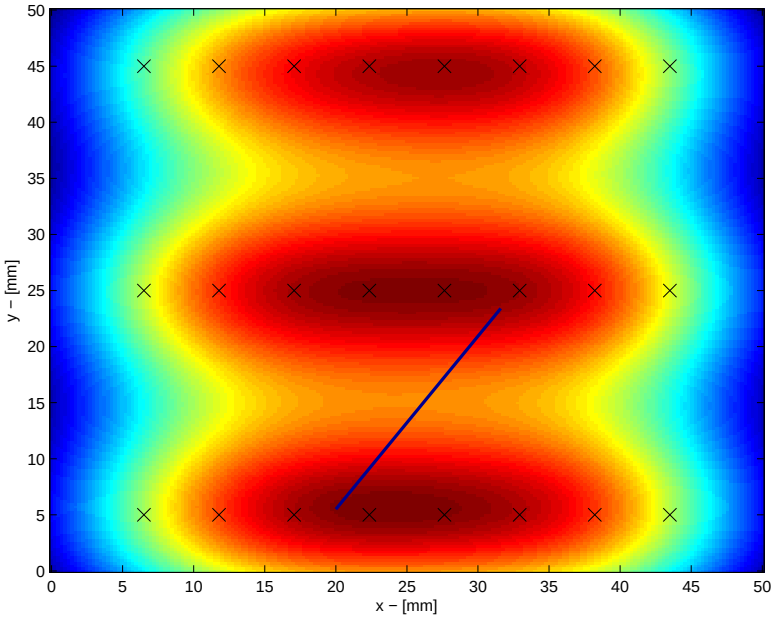


Figure E.4: Data fusion of present (damaged) and reference (undamaged) states for the slanted crack identification.

is very common in damage identification problems using neural networks [5]. In this situation, a large amount of data representing the analysed problem is normalized in function of a mapping technique, leading to a faster training of the neural network and improved identification results. For more details refer to [4, 6, 12].

A Gaussian type mapping was applied and it is defined as

$$\mathbf{z} = (\mathbf{x} - \overline{x}) \left( \frac{z_\sigma}{x_\sigma} \right) + \overline{z} \tag{E.4}$$

where $\overline{x}$ and $x_\sigma$ are the mean and standard deviation of $\mathbf{x}$, respectively. $\overline{z}$ and $z_\sigma$ are the desired values of mean and standard deviation of the resulting mapping. In this study, $\overline{z} = 0.5$ and $z_\sigma = 1$. The application of this mapping technique is consistent with the calculation of previous parameters for obtaining the POD of the plate, since the weights have a Gaussian distribution as well. Fig. E.5 shows the new reconstructed image after the mapping of the DI.

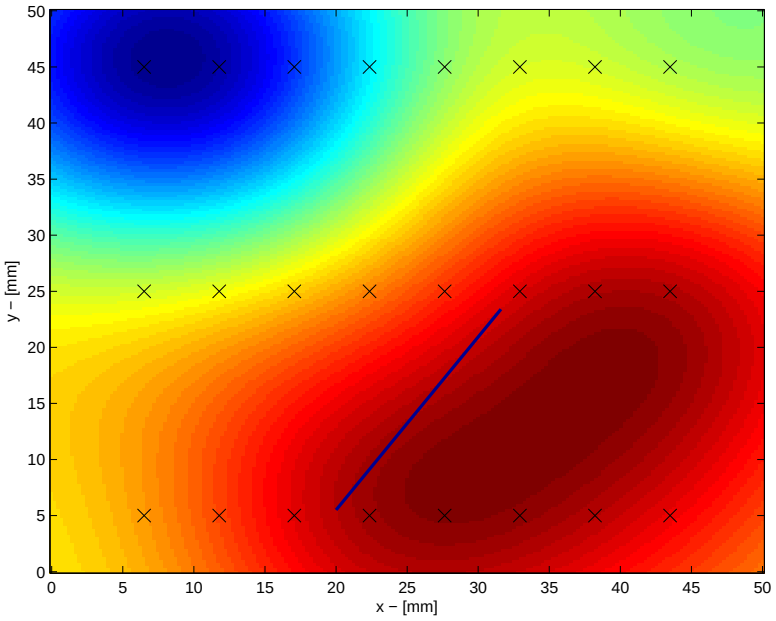


Figure E.5: Data fusion and mapping techniques applied in the slanted crack identification.

The crosses indicate the signal acquisition positions and the line depicts the real crack. A dramatic improvement in the results was noticed upon introducing the mapping into the algorithm.

### E.4.2 Horizontal crack identification

Another crack with zero slope was introduced into a second plate and was evaluated. The crack is centered at the position (15.5;10.1) mm with length 8 mm and parallel to the x-axis. Fig. E.6 shows the signals of present and reference states. In this case, the excitation signal is centered at the frequency 250 kHz. As in the previous case, only the signals at one position are shown for demonstration.

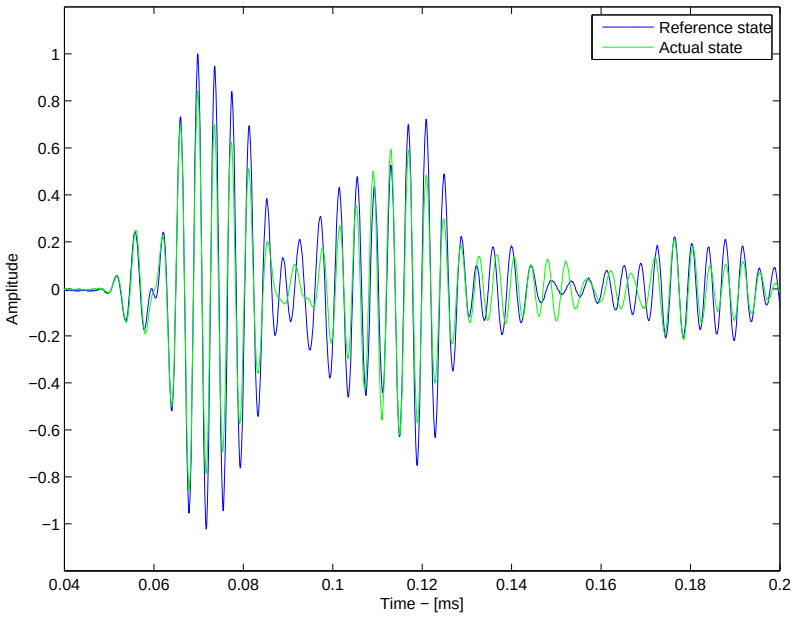


Figure E.6: Comparation between present (damaged) and reference (undamaged) states for the horizontal crack identification.

A small vertical shift and the decrease of the signal amplitude in some peaks are the perceived changes caused by the introduction of the crack. Fig. E.7 illustrates the data fusion of the DI mapping for the crack identification. A reasonable identification is provided for this crack.

### E.4.3 Experimental hole identification

A hole was introduced into the PZT plate, centered at the position (14.43;37.5) mm and radius equal to 4.5 mm. Fig. E.8 illustrates the signals for present and reference states. We consider the reference state as the damaged state of the previous section. Thus, the differences between the signals remarked at the present state are caused by the introduction of an additional defect in the PZT plate.

Fig. E.9 depicts the data fusion of the mapped DI. An excellent estimation of the hole

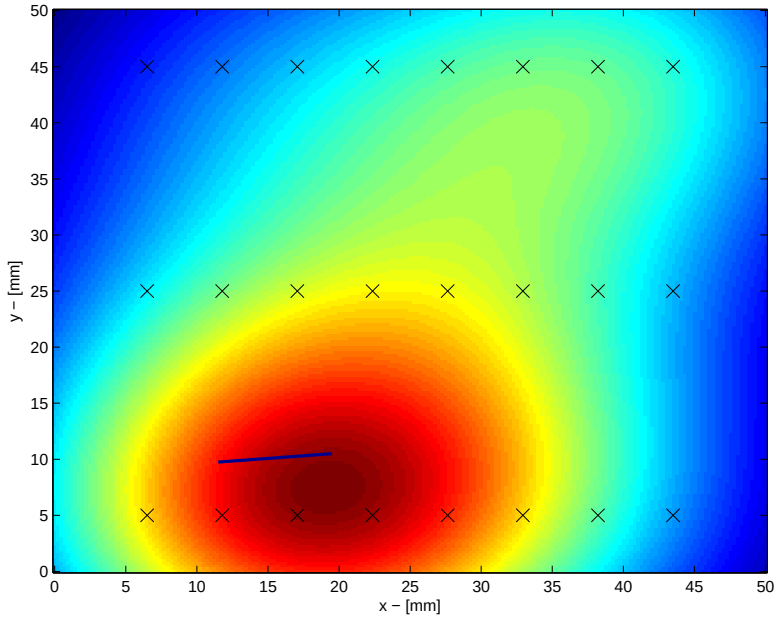


Figure E.7: Data fusion and mapping techniques applied in the horizontal crack identification.

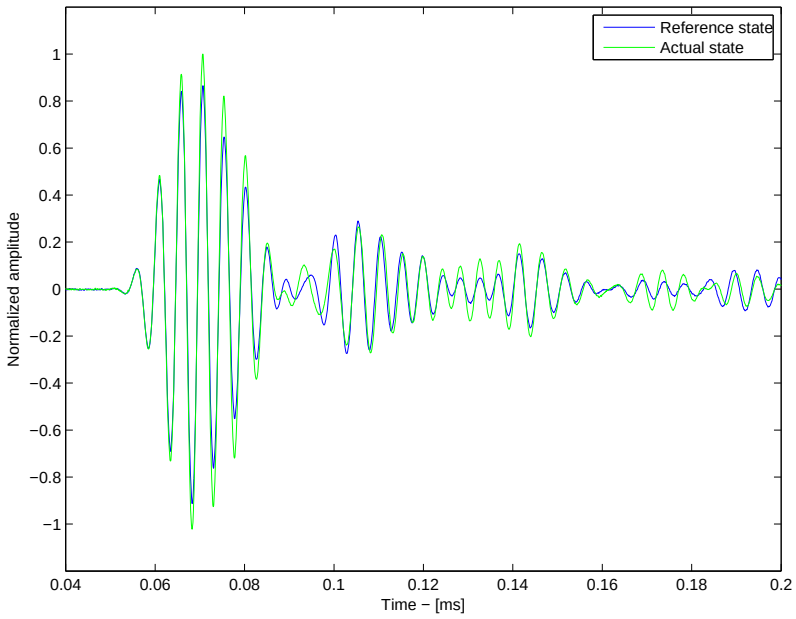


Figure E.8: Comparation between present (introduction of hole) and reference (horizontal crack) states for the hole identification.

position was predicted.

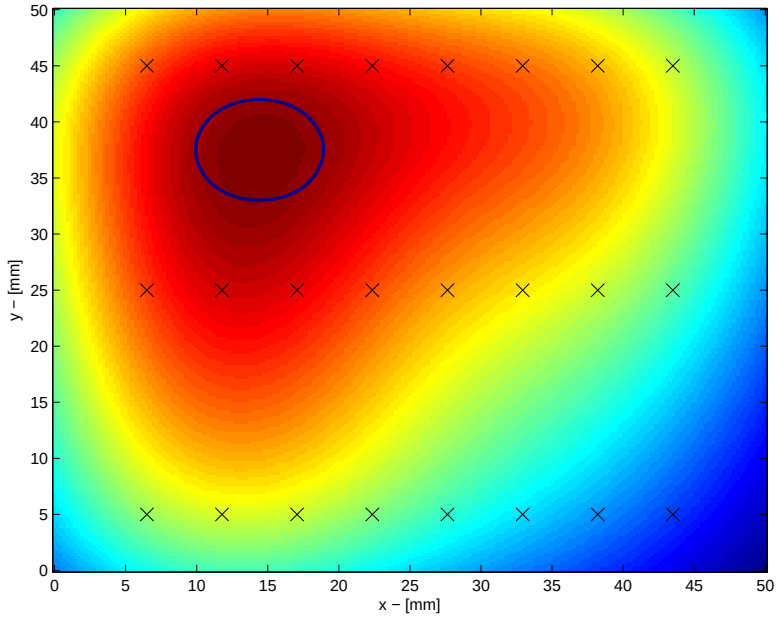


Figure E.9: Data fusion and mapping techniques applied in the hole identification.

## E.5 Conclusions

In this work, an experimental approach for damage assessment in piezoelectric plates has been proposed, based on the correlation at several positions on the plate surface. A data fusion scheme to calculate the probability of damage over the surface, improved by the adoption of a Gaussian mapping. Changes in the electric potential were found to be very small, even for large imposed damages, which could be due to the fact that the electric potential on the surface is almost constant, since the poling direction is in the z-axis. If the poling were in the x or y-axis, a more proeminent change would be noticed. Using the proposed methodology, other types of defects such as de-bonding and impact damage can be detected and quantified.

## Acknowledgements

G. Hattori and A. Sáez are supported by a Spanish National Research Project, reference DPI2010-21590-C02-02. L. Ye is grateful for the research support of a Discovery Project (DP). S. Mustapha is supported by an Australian Postgraduate Award (APA) and a top-up scholarship from the School of Aerospace, Mechanical and Mechatronic Engineering

at the University of Sydney.

## Bibliography


[1] Piezotechnology, 2011.

[2] S. R. Anton and D. J. Inman. Reference-free damage detection using instantaneous baseline measurements. *AIAA JOURNAL*, 47(8):1952–1964, 2009.

[3] G.-V. J. S. Cuc, A. and Z. Tidwell. Structural health monitoring with piezoelectric wafer active sensors for space applications. *AIAA JOURNAL*, 45(12):2838–2850, 2007.

[4] G. Hattori and A. Sáez. Damage identification in multifield materials using neural networks. *Inverse Problems in Science and Engineering*, 2013.

[5] S. Haykin. *Neural Networks: A Comprehensive Foundation*. Prentice Hall, Upper Saddle River, NJ, USA, 2nd edition, 1999.

[6] J. Lee and S. Kim. Structural damage detection in the frequency domain using neural networks. *Journal of Intelligent Material Systems and Structures*, 18(8):785–792, 2007.

[7] S. Mustapha, L. Ye, D. Wang, and Y. Lu. Assessment of debonding in sandwich CF/EP composite beams using $a_0$ Lamb wave at low frequency. *Composite Structures*, 93(2):483–491, 2010.

[8] R. Palma, G. Rus, and R. Gallego. Probabilistic inverse problem and system uncertainties for damage detection in piezoelectrics. *Mechanics of Materials*, 41(9):1000–1016, 2009.

[9] S. B. Park and C. T. Sun. Fracture criteria for piezoelectric ceramics. *Journal of American Ceramics Society*, 78:1475–1480, 1995.

[10] G. Rus, R. Palma, and J. L. Pérez-Aparicio. Optimal measurement setup for damage detection in piezoelectric plates. *International Journal of Engineering Science*, 47:554–572, 2009.

[11] S. S. M. Seth, S. K. and S. Constantinos. Damage detection in composite materials using Lamb wave methods. *Smart Materials and Structures*, 11(2):269–278, 2002.

[12] Z. Su and L. Ye. Lamb wave-based quantitative identification of delamination in CF/EP composite structures using artificial neural algorithm. *Composite Structures*, 66(1-4):627–637, 2004.

[13] A. G. Tobin and E. Pak. Effect of electric fields on fracture behavior of PZT ceramics. In *Proceedings of the Smart Structures and Materials*, 1993.

[14] C. Valle and J. W. Littles. Flaw localization using the reassigned spectrogram on laser-generated and detected Lamb modes. *Ultrasonics*, 39(8):535–542, 2002.

[15] D. Wang, L. Ye, Z. Su, Y. Lu, F. Li, and G. Meng. Probabilistic damage identification based on correlation analysis using guided wave signals in aluminum plates. *Structural Health Monitoring*, 9(2):133–144, 2010.

[16] H. Wang and R. N. Singh. Crack propagation in piezoelectric ceramics: Effects of applied electric fields. *Journal of Applied Physics*, 81(11):7471–7479, 1997.